Achim Fischereder

Synthesis and Characterization of Metal Sulfides for Photovoltaic Applications

zur Erlangung des akademischen Grades eines Doktors der technischen Wissenschaften

erreicht an der

Technischen Universität Graz

Betreuer:

Assoc. Prof. DI Dr. Gregor Trimmel

Institut für Chemische Technologie von Materialien

Technische Universität Graz

Christian Doppler Labor für Nanokomposit-Solarzellen

2011

To my family

EIDESSTATTLICHE ERKLÄRUNG

Ich erkläre an Eides statt, dass ich die vorliegende Arbeit selbstständig verfasst, andere als die angegebenen Quellen/Hilfsmittel nicht benutzt, und die den benutzten Quellen wörtlich und inhaltlich entnommene Stellen als solche kenntlich gemacht habe.

Graz, am …… ……..

(Unterschrift)

STATUTORY DECLARATION

I declare that I have authored this thesis independently, that I have not used other than the declared sources / resources, and that I have explicitly marked all material which has been quoted either literally or by content from the used sources.

…… ……..

date (signature)

Abstract

This work deals with the synthesis and characterization of metal sulfide thin films and the investigation of their performance in solar cell devices. The focus is set on three inorganic semiconductors: $CuInS_2$, Cu_2ZnSnS_4 and ZnS.

The first part of the thesis focuses on a solution based method using commercially available metal salts and a molecular sulfur source (thiourea, thioacetamide). The influence of the sulfur source and of different preparation parameters is evaluated in detail. A special emphasis is placed on the understanding of morphological and chemical changes occurring within the precursor layer during the thermal treatment and on the identification of remaining impurities within the final metal sulfide thin film.

Within the second part, precursors for the preparation of metal sulfides, which are based on metal xanthates, are developed. Through chemical modifications of the alkyl moiety they become soluble in apolar solvents. This allows the preparation of highly concentrated precursor solutions containing the corresponding metal xanthates and the photoactive polymer at the same time. Therefore, a straightforward in situ fabrication of metal sulfide/polymer nanocomposite solar cells is enabled. The optimization of $CuInS_2$/polymer solar cells is presented in detail, showing the high potential of the metal xanthates for their use in nanocomposite solar cells. In addition, for the first time in the literature CZTS thin films using only metal xanthates as precursors are prepared and characterized.

The last part presents the successful preparation of novel mesoporous ZnS thin films using a nanocasting approach. In this case, a mesoporous silica matrix is prepared and consequently infiltrated with ZnS. Afterwards the silica scaffold is selectively etched away to obtain a highly structured metal sulfide thin film.

Zusammenfassung

Das Ziel dieser Arbeit ist die Synthese und Charakterisierung von Metallsulfid-Schichten und ihre Anwendung in Solarzellen. Der Schwerpunkt liegt hierbei auf drei sulfidischen Halbleiter: $CuInS_2$, Cu_2ZnSnS_4 und ZnS.

Der erste Teil der Arbeit beschäftigt sich mit einem lösungsbasierten System, das aus kommerziell erhältliche Metallsalzen und einer molekularen Schwefelquelle (Thioharnstoff, Thioacetamid) besteht. Der Einfluss der Schwefelquelle sowie unterschiedlicher Herstellungsparameter werden im Detail untersucht. Zusätzlich werden morphologische und chemische Vorgänge während der thermischen Bildung analysiert und verbleibende Verunreinigungen innerhalb der fertigen Metallsulfid-Schicht identifiziert.

Im zweiten Teil werden Metall-Xanthate, die als Precursor für Metallsulfide verwendet werden können, untersucht und für die Anwendung in Nanokomposit-Solarzellen optimiert. Durch zielgerichtete chemische Modifikationen werden diese Komplexe in apolaren Lösungsmitteln löslich, wodurch die Herstellung von hoch konzentrierten Precursor-Lösungen, die gleichzeitig Metall-Xanthate und ein photoaktives Polymer enthalten, ermöglicht wird. Hiermit wird eine einfache in situ Herstellung von Metallsulfid/Polymer Nanokomposit-Solarzellen zugänglich. Die präsentierte Optimierung von $CuInS_2$/Polymer-Solarzellen zeigt das hohe Potential der entwickelten Metall-Xanthate für Nanokomposit-Solarzellen auf. Zusätzlich wird das erste Mal in dieser Arbeit auch die Herstellung von Cu_2ZnSnS_4 Schichten ausschließlich unter Verwendung von Metall-Xanthaten beschrieben.

Der letzte Teil beschäftigt sich mit der erfolgreichen Herstellung von neuartigen mesoporösen ZnS Schichten mit Hilfe einer Nanocasting-Methode. In diesen Fall wird eine mesoporöse Siliziumdioxid-Matrix hergestellt und mit ZnS infiltriert. Anschließend wird das Siliziumdioxid-Gerüst selektiv weggeätzt um die hochstrukturierte Metallsulfide-Schicht freizulegen.

Acknowledgment

A great number of people contributed directly to the success of this work. They provided me with the necessary environment, possibilities and support to carry out efficient research. As I had the pleasure to work together with remarkable colleagues I want to say thank you within the next few lines to:

- Assoc. Prof. Gregor Trimmel for providing me with such an interesting and thrilling research opportunity, allowing me the freedom to pursue my own ideas and supporting me during my research projects and stays abroad.
- All members of the Institute of Chemistry and Technology of Materials for the enjoyable atmosphere and special thanks goes to DI Michael Edler for being the most helpful colleague ever and Dr. Thomas Rath for his inspiring discussions and his advice.
- Dr. Heinz Amentisch (GISWAXS), Ing. Josefine Hobisch (TGA), Christoph Kronawetter (logistic support), Dr. Petra Kaschitz (NMR), Prof. Robert Saf (MS measurements)
- Prof. Dr. Galo Soler-Illia and his research group for the fruitful and highly enjoyable 7-months research stay in Buenos Aires
- the Christian Doppler Laboratory for Nanocomposite Solar Cells, the ISOVOLTAIC AG, the Federal Ministry of Economy, Family and Youth for financial support

However, this thesis does not only reflect straight scientific work over three years for me. It feels more like an unforgettable 3-years journey with some low points and even more highlights in a scientific as well as a personal sense. I had the pleasure to get in touch with people from all around the world, which helped me with their advice and support and, fortunately, some even became close friends.
Therefore, I want to express my deepest gratitude to my friends, which are strongly connected to this thesis and which made these 3 years a wonderful time. Especially I wish to thank:

- Michi and Anita for the most enjoyable time (especially lunches) at work
- Silvia and Caro for introducing me to the South American culture and making my time in Buenos Aires a time of constant pleasure and excitement

And last but not least I want to express my deepest gratitude to my family and in this context especially to Gabi, for supporting me every single second and for bringing so much joy into my life.

Table of Contents

1 General Introduction

The production of electricity, using alternative energy sources, is one of the main global challenges that have to be faced in the 21st century. Today the lion's share of the world energy supply is provided by fossil fuel based technologies, leading to an increased emission of carbon dioxide and environmental issues connected with green house gases. Forecasts predict that by 2050, the world energy demand will exceed 30 TW,[1] therefore, alternative technologies have to be found and have to be developed to lower the strong dependence on energy sources like oil, gas and coal. In this context, energy generated by solar energy conversion techniques can play a major role, as these technologies convert the energy provided by the abundant irradiation of the sun and do not produce carbon dioxide during operation. In fact this inexhaustible energy source exceeds the need of energy by humans of about 4 orders of magnitude. Solar energy conversion techniques can provide heating, cooling, natural lighting as well as electricity.[2] Concerning the electricity production the conversion of solar energy can take place indirectly via the production of heat or directly to electricity using photovoltaic (PV) devices. The most important PV technologies, which are available today on an industrial scale, are wafer-based crystalline silicon cells (80 % market share) and thin film solar cells (20 % market share). However, the overall electricity produced with PV devices takes up only a minor part of the worldwide electricity production. This situation is mainly caused by too high production costs. As a result, the average price of a kWh generated by silicon-based PV modules is more than two times larger than for other alternative technologies like wind or natural gas.[1] Fortunately, research in non-silica based PV technologies, has developed alternatives using semiconducting materials, which show a much higher potential for a large scale production than crystalline silicon. These materials exhibit a higher absorption coefficient, therefore, the same amount of light can be harvested using a much thinner active layer (thin film solar cells). As a result, the necessary amount of material needed for the fabrication of such solar cells is reduced of about 2 orders of magnitude. In addition, solar cells using these alternative semiconductors (e.g. $Cu(In,Ga)(S,Se)_2$, CdTe) already showed efficiencies close to 20 %,[3,4] which is comparable with wafer-based crystalline silicon cells.[5] Among these alternative compounds especially transition metal sulfide semiconductors, like Cu_2S, FeS_2, CdS, PbS, $CuInS_2$ and Cu_2ZnSnS_4, are very promising in terms of large scale production.[1]

1.1 Metal sulfides for photovoltaic applications

In contrast to main group elements sulfides, which exhibit ionic bonding characteristics, transition metal sulfides exhibits a highly covalent-metallic bonding between the metal and sulfur atoms. This results in unique electronic and magnetic properties of transition metal sulfides[6,7] and leads to numerous technological applications of these materials. Especially their semiconducting properties triggered an intense investigation of these materials in light emitting diodes and photovoltaic devices. Depending on the type and/or combination of metals in these sulfides a broad spectrum of energy band gaps (E_g) can be achieved. For example the band gap of PbS is around 0.3 eV,[8] whereas, the band gap of ZnS lies around 3.7 eV.[9] So far mainly binary (e.g. CdS, ZnS, CuS, Cu_2S, FeS_2…), ternary (e.g. $CuInS_2$) and quaternary metal sulfides (e.g. Cu_2ZnSnS_4) have been synthesized either as thin films, nanocrystals (NC) or nanotubes. In general, highly crystalline thin films of metal sulfides exhibit properties of the corresponding bulk material, whereas the material properties of metal sulfide NC and nanocrystalline thin films can change significantly, depending on the size and shape of the crystals. This alteration of the properties is caused by a quantum confinement effect,[10] which leads for example to an increase of the band gap with deceasing particle size. Depending on the metal sulfide these effects can be observed for particles sizes of approximately 10 nm and smaller.[11] Among metal sulfides, CdS is one of the most important materials for electronic and optoelectronic applications such as flat panel displays, light emitting diodes, transistors and lasers.[12] However, concerning photovoltaic applications, one of the most successful examples are probably $CuInS_2$ based thin film solar cells reaching already efficiencies on laboratory scale above 12 %[13] and 7.6 % on a commercial scale for a 65 cm x 125 cm module.[14]

1.1.1 Preparation methods of metal sulfide thin films

As this thesis focuses on the preparation and investigation of metal sulfides, this chapter will give a short overview of existing preparation methods of thin metal sulfide films with a special emphasis on photovoltaic applications.

In general, the preparation of metal sulfide thin films can be divided into two main approaches. On the one hand, metal sulfide nanoparticles (NP) can be synthesized

beforehand and then be used as building blocks for the formation of thin films. On the other hand, thin films can be prepared directly from precursors on suitable substrates.

Direct preparation methods of thin films for PV applications can be classified into two main areas: vacuum and non-vacuum based methods. In both cases the metal sulfide thin film can be formed by direct deposition of the sulfides or by sulfurization of pre-deposited elemental metals. Vacuum based methods include, for example, chemical and physical vapor deposition techniques,[15] various sputtering methods[16-18] and single and double source evaporation.[19,20]

Non vacuum based approaches involve spray pyrolysis,[21-23] sol-gel deposition,[23,24] electro deposition,[25,26] photo chemical deposition,[27] chemical bath deposition,[28] solution-based precursor methods[29] and successive ionic layer adsorption and reaction (SILAR).[30]

For the preparation of NP a large pool of different preparation methods was developed, aiming to control the size, shape and stoichiometry of the particles to be able to tailor precisely the material properties. Examples of preparation methods include solid-state reactions[31] and various solution based chemical syntheses like solvothermal routes,[32,33] single source precursor approaches,[34,35] hot injection methods[36] and colloidal routes.[37,38] To avoid aggregation of the synthesized NP and to obtain processible solutions the particles have to be stabilized with capping agents. However, for the preparation of thin films for photovoltaic applications it is crucial to remove these stabilizers after the preparation of the film to improve charge transport properties between the NP. Solar cells using absorber thin films prepared from NP inks showed record efficiencies of around 5 %.[39,40]

1.1.2 Conductivity types of metal sulfides

Depending on the type of metal sulfide and/or its chemical composition, they can show p- or n-type conductivity. For example, Cu_2ZnSnS_4 (CZTS) shows intrinsic p-type conductivity, whereas CdS shows intrinsic n-type conductivity. Therefore, by combination of these materials an efficient p-n junctions can be created, which provides an electric field for the separation of electron hole pairs within the solar cell (see also 1.2.1). This concept is widely employed in thin film solar cells consisting of a p-type absorber layer and a n-type buffer layer.[41] By contrast, the conductivity type of $CuInS_2$ (CIS) can be changed by different preparation methods[42,43] and/or by varying the stoichiometry[44] following the equations:

$\{([Cu]+3[In])/2[S]\}-1<0$ → **p-type** $\{([Cu]+3[In])/2[S]\}-1>0$ → **n-type**

The squared brackets refer to the elemental concentrations in this case. When the result of the equation is smaller than 0 the material shows p-type conductivity (hole conductivity), is it larger than 0 n-type conductivity (electron conductivity). Due to this flexibility of CIS it is even possible to fabricate a "one material p-n junction".[43]

Besides thin film solar cells, metal sulfides with n-type conductivity play a very important role as electron acceptors in various types of hybrid solar cells.

As one focus of this thesis lies in the application of metal sulfides in nanocomposite solar cells, the following chapter will now introduce general aspects of nanocomposite solar cells (work principle and performance parameters) with a special emphasis on the use of metal sulfides as electron acceptor materials for the fabrication of these cell types.

1.2 Hybrid solar cells

In general, the photoactive layer of nanocomposite solar cells consist of a nanostructured n-type and a nanostructured p-type semiconductors in close contact with each other. In the literature various material combinations can be found, reaching from all-inorganic compound solar cells (combination of n-type TiO_2 and p-type CIS),[45] via organic-inorganic solar cells (solid state dye sensitized solar cells,[46] solar cell based on a bulk heterojunction concept[47]) to all-organic solar cells (polymer solar cells[48]).

The highest conversion efficiencies using nanocomposite solar cell assemblies were reached with dye sensitized solar cells (DSSC),[49] however, in these cases a liquid electrolyte, acting as hole transporting phase, is used. This characteristic makes the cells susceptible to leakage and unsuitable for large scale production. In the case of solid state dye sensitized solar cell (ssDSSC)[50] the electrolyte is replaced by a solid and transparent hole conductor (e.g. CuSCN), however, these cells do not reach the efficiencies of DSSC.

Besides these solar cells, which use dyes for the absorption of light, devices based on a blend of a p-type organic polymer and a second n-type material, a so called bulk heterojunction architecture, showed record conversion efficiencies of up to 8.3 %.[4] The most successful and most intensively studied assembly is the combination of a p-type conductive photoactive polymer (e.g. MDMO-PPV, P3HT) and n-type buckminsterfullerenes (e.g. [6,6]-phenyl-C_{61}-butyric acid methyl ester (PCBM)).[51] In this case, the bulk heterojunction architecture can be achieved easily as highly concentrated solutions containing the polymer

and PCBM can be prepared due to the good solubility of buckminsterfullerene derivatives in organic solvents. After absorption of light and generation of electron hole pairs (excitons) within the polymer phase, a photoinduced electron transfer from the polymer to the buckminsterfullerene[52] takes place. As a result, efficient charge separation as well as a good charge transport, based on the good electron mobility in buckminsterfullerenes, is ensured.

However, this concept is not limited to the organic/organic assembly (e.g. polymer/PCBM) and can be extended easily to an inorganic/organic system (e.g. polymer/n-type inorganic semiconductor). In this case, the inorganic semiconductor takes over the function of the PCBM. Exciton separation takes place at the inorganic semiconductor/polymer interface[53] and electron transport occurs within the inorganic semiconductor phase. This kind of solar cell, where an organic and inorganic semiconductors are in close contact with each other, are referred to as hybrid solar cells. Such solar cells show supreme design flexibility as they combine the excellent film forming properties of conjugated polymers with the adjustable electronic properties of inorganic semiconductors (see 1.2.3).[54]

The following chapter will now focus on the working principle and performance parameters of such cells before going into detail about the role of metal sulfides as electron acceptors in hybrid solar cells using a bulk heterojunction architecture.

1.2.1 Work principle of a hybrid solar cell

In general, a hybrid solar cell, as every solar cell, converts the energy of light into electricity. The first step involves the absorption of light and generation of excitons. This process can take place when the energy of the incoming light ($h\upsilon$) exceeds E_g (difference between the HOMO and LUMO level) of the semiconducting material. In the case of the well studied polymer/PCBM solar cells, the absorption of light occurs mainly within the polymer phase, as the buckminsterfullerene derivatives show extremely low absorption coefficients above 400 nm.[55] Therefore, the general scheme depicted in Figure 1 became officially accepted.[56]

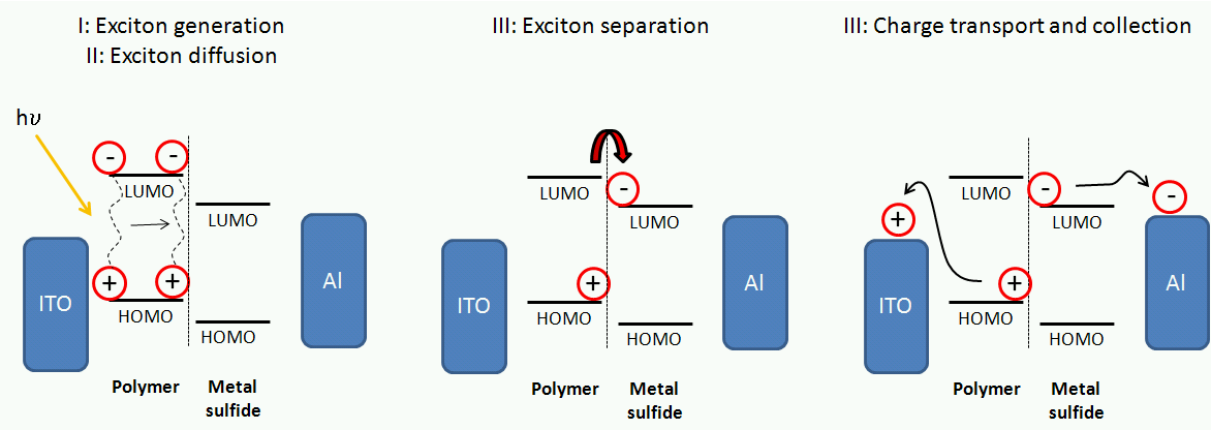

Figure 1: Principle steps involved in the charge formation within a hybrid solar cell upon adsorption of light by the conjugated polymer.

In the case of hybrid solar cells, especially when metal sulfides with large absorption coefficients at high wavelengths and low E_g (e.g. CIS) are used, the initial absorption of light can also take place within the inorganic phase (see Figure 2). This is a big advantage of hybrid solar cells, as the whole volume of the active layer contributes to the generation of charges.

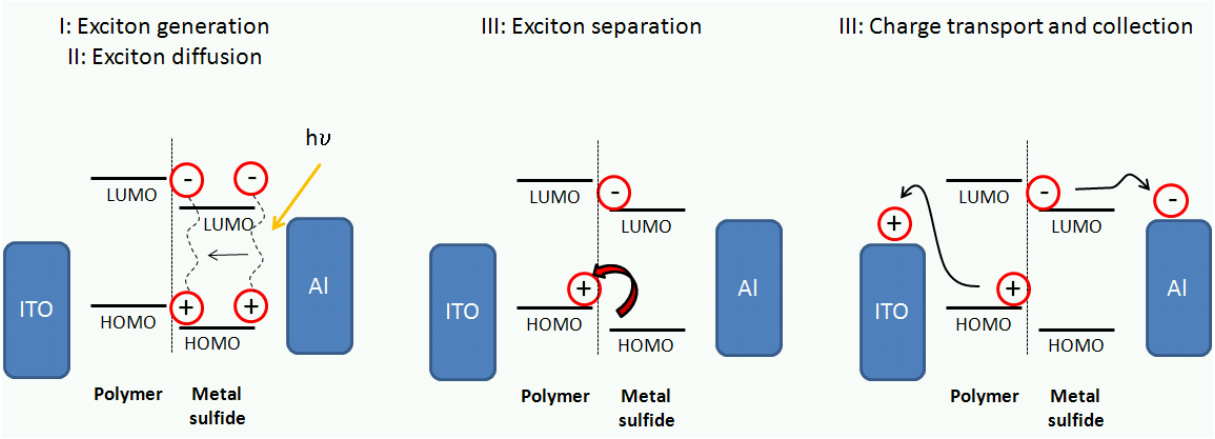

Figure 2: Principle steps involved in the charge formation within a hybrid solar cell upon adsorption of light by the n-type semiconductor.

Independent from the phase where light is absorbed within the active layer of a hybrid solar cell, the generated exciton has to diffuse to an organic/inorganic interface to be able to dissociate into free charges. Before the separation, the positive and negative charge (electron hole pair) are electrostatically bound to each other and cannot move independently from each other to the corresponding electrodes. In addition, an exciton has

only a limited lifetime, in other words, it can only travel a certain distance before it recombines. Within conjugated polymers (e.g. P3HT) this diffusion length (L_o) is approximately 10 nm.[57] Excitons, which are not generated within this 10 nm range to the next organic/inorganic interface recombine and do not contribute to the photocurrent (see Figure 3 "bilayer architecture").

Assuming a suitable band alignment (the HOMO and LUMO level of the n-type semiconductor has to be approx. 0.3 eV below the HOMO and LUMO levels of the polymer)[58] the exciton dissociates at the organic/inorganic interface forming free charges, which can be transported to the corresponding electrodes in the last step.

Two main parameters, which are independent from the material properties, play an important role for the conversion efficiency of such solar cells. Firstly, the film thickness has a strong influence on the efficiency of the charge transport and on the percentage of light that can be absorbed by the active layer. Thicker layers absorb more light, however, at the same time the generated charges have to travel a longer way to the electrodes, which leads to a more pronounced recombination losses. This situation is caused by limited charge carrier mobilities of the components. In general, the hole transport mobility of the organic polymer present here the limiting factor. Secondly, the morphology of the active layer has a significant influence on the performance of a hybrid solar cell. The mentioned limitation in exciton diffusion length is one of the main driving forces for the development of different solar cell architectures Figure 3.

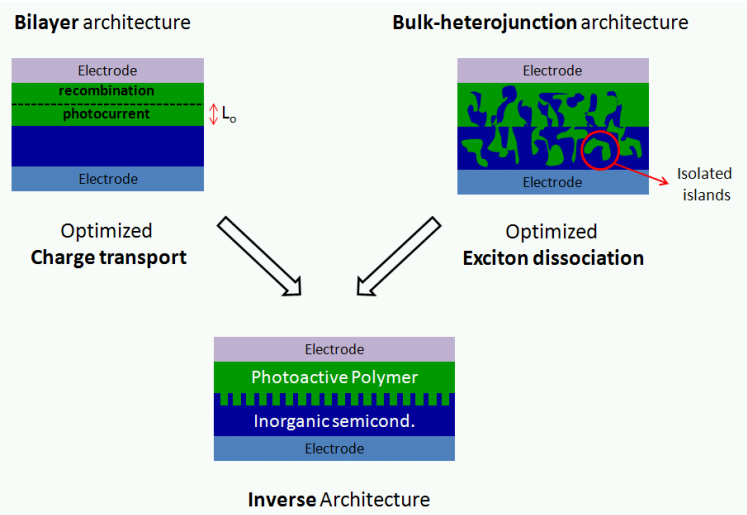

Figure 3: Different solar cells architectures using an active layer consisting of an organic polymer and inorganic semiconductor.

The simplest architecture of a two-phase active layer presents a simple bilayer device. However, this architecture suffers from significant losses due to recombination of excitons, as a large number of excitons are generated too far away of the organic/inorganic interface to be able to reach it before they recombine. In this case, only excitons, which are generated within 10 nm to the interface, can dissociate and contribute to the generation of a current. This problem gave rise to the bulk heterojunction assembly, where the two phases form an interpenetrating network, providing a large organic/inorganic interface throughout the active layer. In this case, fewer losses due to exciton recombination are suffered, however, very often a large number of isolated islands (organic as well as inorganic ones) form This leads to a recombination of charges, hence, an inefficient charge transport to the electrodes. In this case the control of the nanomorphology becomes the major problem. As one part of this thesis embraces this issue by focusing on the preparation of mesoporous n-type semiconducting thin films, a third approach is presented at this stage. This type can be seen as a combination of a good charge transport from the bilayer device and a large interface from the bulk heterojunction architecture and is called “Inverse architecture” within this thesis. This ideal case can be achieved by providing a mesoporous metal sulfide thin film, which is consequently infiltrated with an organic polymer. At this way a large organic/inorganic interface without the formation of isolated island is provided, allowing the separation of the majority of the formed excitons and efficient transport of the free charges to the electrodes at the same time.

1.2.2 Performance Parameters

Figure 4 shows a current voltage I-V characteristic of a solar cell. In the dark (black line) the cell shows a typical diode behavior as hardly any current is generated until the contacts start to inject charges at forward bias at voltages larger than the open circuit voltage.[59]

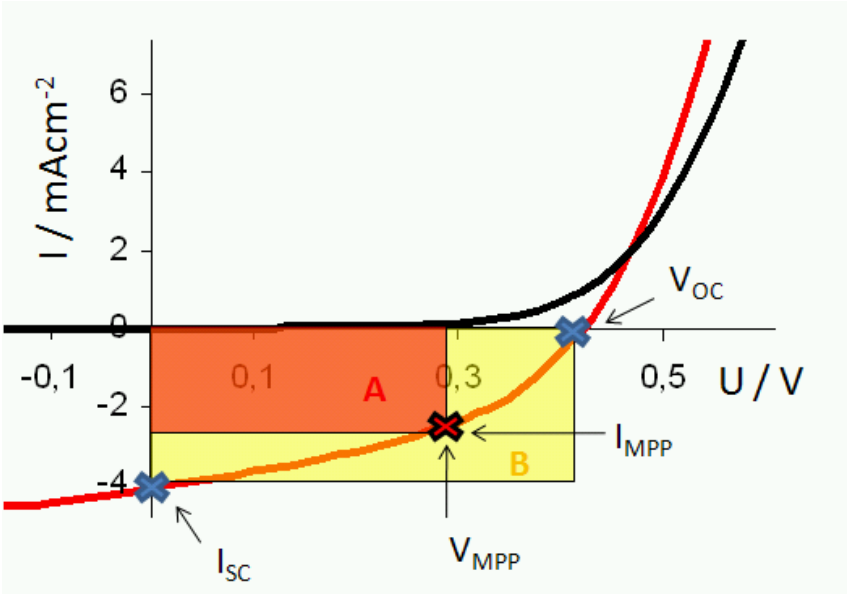

Figure 4: I-V characteristic of a solar cell including the main data points for the characterization of the cell and the calculation of the power conversion efficiency.

Under illumination of light the I-V curve is shifted vertically, due to the generation of photoinduced charge carriers. When the device is illuminated and forward biased (a voltage between 0 and V_{OC} (open circuit voltage) is applied, power is produced. By using only three characteristic points from the I-V curve under illumination all main performance parameters of the solar cell can be calculated.

The first point is the V_{OC}, which represents the electrical difference between the electrodes, when no current is flowing. Within a simple metal-insulator-metal (MIM) device this would be the difference between the work functions of the electrodes.[60] However, in the case of heterojunction devices, as hybrid solar cells, the V_{OC} is determined by the band offset between the HOMO level of the polymer and the LUMO level of the inorganic semiconductor (see Figure 5).[61] On the one hand, this difference should be as large as possible, as the power conversion efficiency depends on V_{OC} (see below). On the other hand, the optical band gaps of the components ($E_{g,P}$ and $E_{g,IS}$) should not be too big to enable the absorption of a high percentage of the incoming light. In addition, the difference between the two LUMO levels (E_D) should be at least 0.3 eV to ensure efficient exciton dissociation.[58,62]

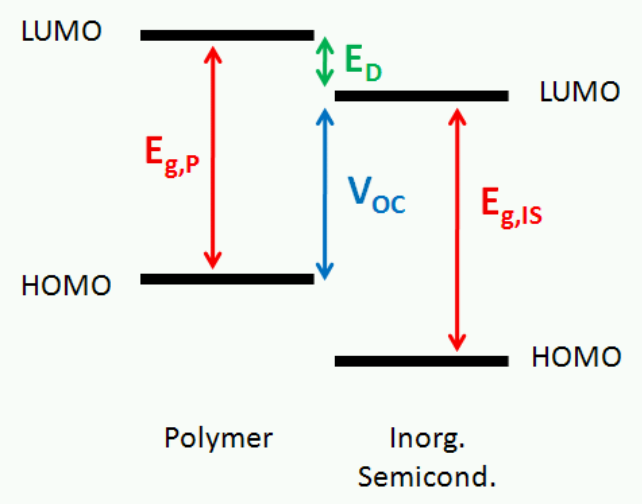

Figure 5: Energy alignment of a hybrid solar cells and corresponding parameters ($E_{g,P}$ and $E_{g,IS}$ are the optical band gaps of the polymer and the inorganic semiconductor, respectively; E_D is the energy difference needed for the separation of excitons; V_{OC} is the maximum open circuit voltage that can be obtained from the cell)

Although the V_{OC} is mainly determined by the energy offset between the HOMO level of the polymer and LUMO level of the inorganic semiconductor, also other parameters like the nanomorphology of the active layer,[63] charge carrier losses at the electrodes[64] or interfaces [65] can have a significant influence.

The second data point is the I_{SC}, which corresponds to the maximum number of charge carriers that can be extracted from the photovoltaic device under illumination. The I_{SC} is measured at zero bias and is a function of the elementary charge *e*, the charge carrier density *n* under illumination, the carrier mobility μ and the electric field *E*.[66]

$$I_{SC} = e \cdot n \cdot \mu \cdot E \qquad (1)$$

Especially *n*, which correspond to the number of free charges, and μ are affected by the architecture of the cell as well as the energy alignment of the two phases within the active layer.[59] A parameter which is closely related to I_{SC} is the external quantum efficiency or incident photon to current efficiency (IPCE).

$$IPCE(\lambda) = \frac{1240}{\lambda}\frac{I_{SC}}{P_{IN}} \quad (2)$$

Simplified, the IPCE shows the ratio between electrons collected under short circuit current and the number of incident photons at a given wavelength. For example, this factor would be 100 %, if every incident photon generates one electron that can be extracted from the device.

The third parameter is the point of maximum power (intersection of I_{MPP} and V_{MPP}), which defines the current and voltage at with the solar cell produces maximum power (P_{MAX}) under illumination. At this point the product between current and voltage is maximal.

$$P_{MAX} = I_{MPP} \cdot V_{MPP} \quad (3)$$

The quality of the I-V curve can be described by the fill factor (FF), which is expressed by the ratio of P_{MAX} and the product of V_{OC} and I_{SC}.

$$FF = \frac{P_{MAX}}{V_{OC} \cdot I_{SC}} \quad (4)$$

The FF describes the ability of the charge carriers to reach the electrodes when the build-in field is lowered towards V_{OC}.[59] When the electric field is reduced, the distance, which can be covered by the charge carriers, is lowered as well. This leads to increased losses due to charge recombination, hence, a reduction of the current. In addition, resistances within the different components of the solar cell (e.g. organic polymer, inorganic semiconductor, electrodes) as well as at their interfaces drastically lower the fill factor.[67]

The most important cell parameter, which can be calculated using these three points, is the power conversion efficiency (η) of the device. In other words, the ratio between the power output from the device and power input into the device.

$$\eta = \frac{P_{OUT}}{P_{IN}} = \frac{V_{OC} \cdot I_{SC} \cdot FF}{P_{IN}} = \frac{P_{MAX}}{P_{IN}} = \frac{I_{MPP} \cdot V_{MPP}}{P_{IN}} \quad (5)$$

To be able to draw a comparison between different solar cells, standardized conditions for the light source for the illumination of the device are set. The source has to have a power

density of 1000 W/m^2 with a spectral intensity distribution being equal to the sun on the earth's surface with an incident angle of 48.2 ° (AM 1.5 spectrum).[68]

1.2.3 Metal sulfides as electron acceptors

As mentioned above, n-type semiconducting metal sulfides can act as electron acceptors in hybrid solar cells, using a bulk heterojunction architecture. In the literature several example can be found using metal sulfides (e.g. $CuInS_2$,[69] CdS,[47] or PbS[70]) as electron acceptors together with p-type organic polymers.

There are several reasons why inorganic semiconductors, such as metal sulfides, have found scientific interest in hybrid solar cells:[54]

- they can have very high optical absorption coefficients and good photoconductivities
- various inorganic semiconductors show band gaps which are ideal for photovoltaic applications (e.g. CIS: E_g = 1.5 eV)
- the n- and p-type doping level can be adjusted, hence the charge transport properties in organic/inorganic composites can be tailored.
- the electronic properties of inorganic nanoparticles can be varied depending on the size of the nanoparticles. Particles, which are smaller than approximately 10 nm are subjected to a quantum confinement effect, allowing the variation of E_g of the semiconducting material.
- their surface to volume ratio is very high, which provides a large interface for exciton separation

Due to the possibility to tailor the electronic properties of metal sulfides (variation of E_g, alteration of the HOMO as well as LUMO level) by varying their size, shape and chemical composition, they are highly flexible regarding their possible applications. In the case of conjugated polymers especially the film forming and physiochemical properties can be varied easily. As a result the combination of metal sulfides with conjugated polymers in hybrid films brings together their specific advantages (although each compound still possesses its chemical identity) and allows a good adaptability of the whole system.[71]

In general, a bulk heterojunction architecture using an inorganic semiconductor and a photoactive polymer can be achieved in two ways (see Figure 6).

Firstly the active layer can be prepared by applying a solution of pre-synthesized NP and an organic polymer. Herein, this method is named “Nanoparticle Approach” and is depicted in Figure 6, left. Unfortunately, NP show low solubility in apolar solvents and tend to form large aggregates. To solubilize them and to inhibit agglomeration of the particles they have to be stabilized by organic surfactants. Solar cells using this approach have already achieved record power conversion efficiencies of 3.13 %.[72] However, these surfactants present a certain limitation as they hinder the charge transport properties between the organic/inorganic interfaces as well as within the inorganic phase itself.[54] In addition, removal of the surfactants turns out to be very difficult, which leads to a significant reduction in power conversion efficiencies of these cells.

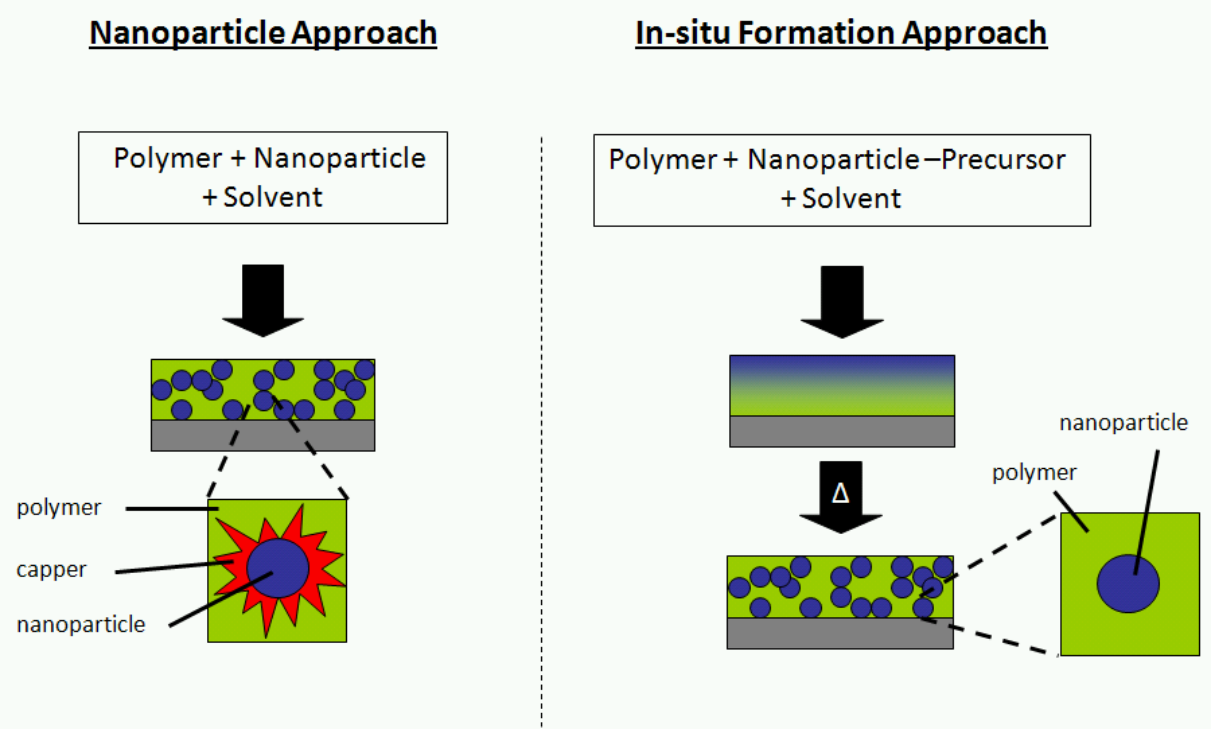

Figure 6: Formation of a bulk heterojunction architecture between an organic polymer and inorganic NPs using the “Nanoparticle Approach” (left) and the “In-situ Formation Approach” (right).

The second approach, named “In-situ Formation Approach” (Figure 6, right) within this work, uses a solution, containing precursors for the inorganic semiconductor and the photoactive polymer. In this case, the inorganic semiconductor is formed directly within the polymer matrix by some kind of treatment (e.g. heat, vapor, light) of the precursor layer.

When this method is employed, it is important to choose precursor materials, which are soluble and do not form decomposition by-products, which cannot be removed from the active layer. In this case, the polymer matrix replaces the organic surfactant, inhibiting the agglomeration of NPs. Therefore, no insolating shell of capping agent is present, hence, good charge transport properties between the organic and inorganic phase are ensured.

For the first time the "In-situ Formation Approach" was used for the fabrication of metal oxide/polymer composites (e.g. ZnO/P3HT),[73] where metal complexes were hydrolyzed within the polymer matrix to form an interpenetrating metal oxide semiconductor phase. Regarding metal sulfides, only very few reports can be found in the literature. This concept was already realized for CdS[47,74] and will be discussed for other metal sulfides as CIS and CZTS in detail in chapter 3.4.

1.3 Scope and aim of the thesis

This thesis focuses on the synthesis and characterization of metal sulfide semiconductors for photovoltaic applications. On the one hand, these materials will be prepared as metal sulfide thin films for the use as absorber layers in pure inorganic thin film solar cells. On the other hand, metal sulfide/polymer nanocomposites, which can be applied as active layers in hybrid solar cells, will be fabricated. In general, the thesis divides into two main parts.

The first part, which includes chapter 2 and 3, deals with the synthesis of CIS and CZTS using a solution based precursor approach. In this case, a solution, containing the metals sulfide precursors, will be applied on substrates to form a precursor layer, which is thermally treated to obtain the final metal sulfide thin film. In both chapters a broad range of analytical methods will be used to assess the optical, electrical, chemical and structural properties of the obtained CIS and CZTS materials. In addition, a special focus will be placed on the investigation of chemical and morphological changes, which occur during the conversion of the precursors. For this purpose, precursor layers will be analyzed during the thermal conversion step to the metal sulfide, using synchrotron radiation based characterization techniques.

In detail, chapter 2 will use commercially available metal salts in combination with an external molecular sulfur source (thiourea or thioacetamide) as precursor materials. The influence of the molecular sulfur source as well as of different preparation parameters (e.g.

synthesizing temperature) on the formation process of the metal sulfide thin films and its final properties will be studied.

Within chapter 3, the synthesis of novel metal xanthates, which are soluble in apolar solvents, will be targeted and their application for the preparation of CIS and CZTS metal sulfide thin films and metal sulfide/polymer nanocomposite layers will be evaluated. Additionally, CIS/polymer nanocomposite solar cells will be fabricated and optimized to assess the potential of these novel precursors for photovoltaic applications.

The second part of the thesis, chapter 4, will deal with the preparation of nanostructured metal sulfide thin films. In detail, a synthetic approach for mesoporous ZnS thin films using a nanocasting method will be targeted. In the first step a mesoporous silica matrix will prepared and consequently infiltrated with ZnS. In the last step the silica exotemplate should be removed to obtain a stable and silica free mesoporous ZnS thin film. Among standard characterization methods, synchrotron based characterization methods will be employed to gain a deeper understanding in the preparation process.

2 Metal sulfide thin films prepared by solution based precursor methods

2.1 Introduction

Inorganic semiconducting thin films can be synthesized by numerous preparation techniques ranging from vacuum to non vacuum based approaches.

This chapter focuses on the preparation and characterization of metal sulfide thin films using a solution based method, which can be classified as a non vacuum based method. In this case, metal salts together with a molecular sulfur source act as precursors for the metal sulfide. In addition, a special emphasis is placed on the application of these films in photovoltaic applications. The general preparation scheme is shown in Figure 7. The precursors are dissolved in an appropriate solvent and the obtained solution is consequently applied on suitable substrates to form a precursor layer. The decomposition of the precursors, hence, the formation of the metal sulfide thin films is induced by a thermal treatment.

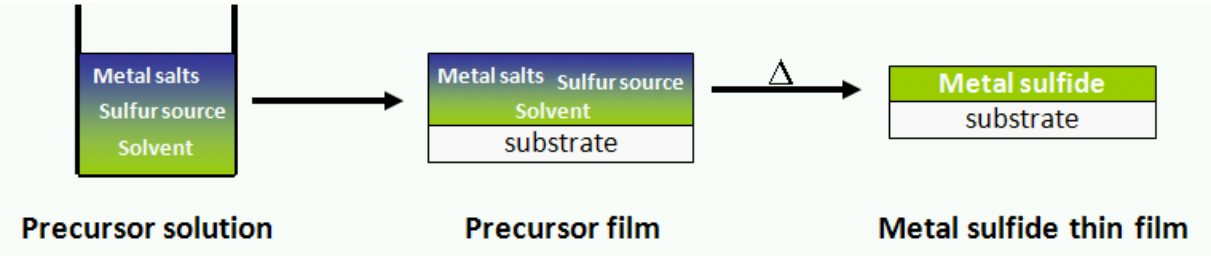

Figure 7: General preparation scheme of metal sulfide thin films using the solution based precursor method.

In contrast to vacuum based methods no sophisticated equipment is needed to gain precise control of the preparation parameters (temperature and pressure). In addition, solution based precursor methods show a very high versatility as the chemical composition of the final metal sulfide can be adjusted by varying the metal salt concentrations within the precursor solution. Moreover, large area films can be prepared easily as the solution can be applied by highly developed deposition methods as spin coating, doctor blading or spraying.

Due to their relevance and importance for photovoltaic applications, a specific focus is placed on the synthesis and characterization of CIS, a ternary semiconductor, and CZTS, a quaternary semiconductor.

2.2 $CuInS_2$ thin films

2.2.1 Introduction

$CuInS_2$ (CIS) belongs to the family of I-III-IV_2 semiconductors. In this work the abbreviation CIS refers only to $CuInS_2$ and does not involve the extensively researched sister material $CuInSe_2$ or any other semiconductor of the $Cu(In,Ga)(S,Se)_2$ family. There has been a very strong scientific interest in the investigation and development of CIS based solar cells since the first reports of photovoltaic devices. In 1977 the first CIS homojunction solar cells[75] as well as heterojunction cells with CdS as buffer layer[76] were published. This interest is caused by the superior material properties of CIS for photovoltaic applications. It possesses a direct band gap of 1.5 eV,[77] which is very close to the optimum value for terrestrial solar cells.[78] Assuming an ideal single junction solar cell the maximum theoretical power conversion efficiency, which can be achieved with CIS, is 28.5 %.[78] This value is among the highest figures for photovoltaic devices (e.g. silicon: 24 %; GaAs: 28 %).[75] Doping of CIS with Ga allows a variation of the band gap and has evolved into one of the most efficient approaches to improve the efficiency of CIS based solar cells.[79] Other dopants as Ag, Mg, or Zn can also have a significant influence on the performance of the cells.[80] In addition, CIS shows a large absorption coefficient[81] and a high photoconductivity.[69]

An other possibility, which is offered by CIS, is the convertibility of the conductivity type (p- or n-type conductivity). Depending on the stoichiometry, n-type or p-type CIS can be synthesized (for details see 1.1.2). In short, sulfur rich CIS shows p-type majority carriers, whereas sulfur poor and copper poor materials show n-type majority carriers.

Based on the versatility of CIS, it can be found in various solar cell types ranging from all-inorganic thin film devices (e.g. homo and heterojunction devices)[75] to nanocomposite solar cells (TiO_2/CIS device,[82] ETA - extremely thin absorber - devices,[83] Polymer/CIS hybrid devices).[69]

State of the art CIS based thin film solar cells, prepared by vacuum based evaporation techniques, already reached efficiencies on the laboratory scale above 12 %[13] and are

already available on a commercial scale with efficiencies of 7.6 % for a 65 cm x 125 cm module.[14] However, thinking of large scale production non vacuum based techniques would be preferable. Several of these techniques (e.g. spray deposition, sol gel deposition) use precursor solutions containing metal salts and molecular sulfur sources. One essential part of the investigation of the performance of prepared CIS materials the fabrication of solar cell devices. However, at the same time it is crucial to gain a deeper knowledge about the chemical and morphological changes within the precursor layer, which occur during the CIS formation. Therefore, the next chapter addresses the investigation of a solution based precursor method using pyridine as solvent. Additionally, a special focus is placed on chemical and morphological changes occurring during the CIS film formation in dependence on the synthesizing parameters and the concentration of the molecular sulfur source within the precursor solution.

2.2.2 Experimental

Chemicals

Copper (I) acetate (CuAc, 97%), indium (III) chloride ($InCl_3$, 98%), thiourea (TU, 99%) and pyridine (reagent plus ≥99%) were purchased from Sigma Aldrich and used without further purification.

Indium tin oxide- (ITO)-coated glass substrates with a surface resistivity of 15-25 Ω/cm^2 were purchased from Delta Technologies Ltd.

Sample preparation

ITO-coated glass substrates were cleaned in an ultrasonic water bath followed by an ultrasonic isopropanol bath, each for 20 min. The CIS precursor solution consisted of CuAc (0.22 mol/L), $InCl_3$ (0.15 mol/L) and TU (0.6 mol/L, 1.05 mol/L or 1.5 mol/L) dissolved in pyridine. The solution was then spin coated on the substrates at a speed of 1000 rpm, which were then baked for 30 min at different temperatures in the range of 160 – 450 °C under vacuum. After the heat treatment the samples were cooled down to room temperature under vacuum within 10 min.

For XRD analysis, TEM-EDX measurements and mass spectroscopy studies the CIS-precursor solution was sprayed onto glass substrates at ambient conditions, followed by the

same heat treatment of the substrates as described above. Finally the µm thick CIS layer was scraped off the glass substrate to obtain a CIS powder.

For TG/MS measurements 25 µL of the CIS-precursor solution was transferred into an Al2O3 crucible, which was consequently stored under vacuum at 60 °C for 8 hours prior the measurement.

Characterization

The X-ray powder diffraction profiles were measured with a Siemens D-5005 powder diffractometer (θ/θ geometry, Cu Kα radiation, graphite monochromator, scintillation counter, step width 0.02 °, constant counting times of 10 s/step, measured range of 10 - 70 ° in 2θ). Transmittance and reflectance spectra of the thin films were measured with a Lambda 900 spectrometer (Perkin Elmer) including an external integrating sphere diffuse reflectance accessory (PELA-1000). The surface morphology was studied with a Veeco Dektak 150 surface profiler and a JEOL JSM-5410 scanning electron microscope equipped with a secondary electron detector. Energy dispersive X-ray (EDX) spectra were recorded in scanning transmission electron microscopy (STEM) mode using a Philips CM20/STEM operated at 200 kV with a LaB_6 cathode equipped with a Noran HPGe-detector. Simultaneous 2D grazing incident small angle X-ray scattering (GISAXS) and 1D gracing incident wide angle X-ray scattering (GIWAXS) measurements were performed at the Austrian SAXS Beamline 5.2L of the electron storage ring ELETTRA (Italy).[84] The beamline has been adjusted to a q-resolution ($q=4\pi/\lambda*\sin(2\theta/2)$) between 0.1 and 3.1 nm^{-1} (GISAXS) to resolve the angular range (2θ) between 21.1 ° and 41.8 ° (GIWAXS) using a X-ray energy of 8 keV. The glass/ITO/precursor-substrates were placed in a custom made sample cell with a grazing angle of about 0.18 ° and were heated from 40 °C up to 190 °C at a heating rate of approx. 8 °C min^{-1} under vacuum. During the temperature scan, data were recorded with 5 s and 10 s resolution for GISAXS, using an image intensified CCD detector (Model CV 12, Photonic Science Ltd., Millham / UK), and GIWAXS, using a 1-D gas detector based on the delay line principle, respectively. The simultaneous TG/MS measurements were carried out with a Netzsch STA 449C thermal analyzer under helium atmosphere and the helium flow was fixed at 50.0 mL min^{-1}. The samples were held at 20 °C for 10 min, then heated up with a rate of 8 °C min^{-1} followed by an isothermal step at 550 °C for 10 min. The volatile products of the thermal decomposition were analyzed online with a Netzsch QMS 403C quadrupole

mass spectrometer. Mass spectrometry studies on CIS powders were carried out with direct insertion mass spectrometry (DI-MS) with electron impact (EI, 70 eV) on a Waters GCT Premier.

2.2.3 Results and discussion

Sample preparation

Precursor solutions were prepared from metal salts (copper(I) acetate, indium(III) chloride) and thiourea (TU) in pyridine. To investigate the influence of the synthesizing temperature and the sulfur source on the formation of CIS, samples with three different amounts of TU within the precursor solution were prepared, each annealed at three different temperatures. It was shown that a certain excess of TU is necessary to compensate the loss of sulfur during pyrolysis,[85] therefore, three series of solutions with a S/(Cu+In) ratio within the precursor solution of 1.6, 2.8 and 4 (1.6, 2.8 and 4 equiv. TU) were prepared. The Cu/In ratio was fixed at 1.5 to avoid secondary phases like In_2S_3[86-88] and to favor the formation of CIS with chalcopyrite structure.[85] The precursor solutions were spin coated (in situ GISWAXS studies, SEM analysis, UV/vis measurements) to obtain thin films and also sprayed onto glass substrates (XRD analysis, TEM-EDX analysis, DI-MS analysis) to prepare CIS powders. In both cases the precursor layers were baked at different synthesizing temperatures (200, 300 and 450 °C) to obtain CIS thin films. Samples for TG/MS studies were prepared by adding 25 µL of the CIS precursor solution into an Al_2O_3 crucible, which was then stored under vacuum at 60 °C for 8 hours.

X-ray diffraction

For all samples we observed the major characteristic X-ray diffraction peaks (112), (220), (312) for the chalcopyrite type structure of CIS (Figure 8). Additionally, the XRD patterns obtained at 300 and 450 °C also show the minor superstructure reflections (200), (224) and (440) of the chalcopyrite crystal structure, due to the higher crystallinity of these powders. The positions of the reflections are in good agreement with literature values of crystalline CIS (chalcopyrite), according to the Powder Diffraction File (PDF) 27-159 of the International Centre for Diffraction Data.

The crystallinity of the obtained CIS powders (see Table 1) depends strongly on the synthesizing temperature, as all reflections get sharper with increasing temperature. In

contrast to this, the concentration of TU has only a minor influence. It has to be noted that the uncertainty of the estimation of the crystallographic domain sizes using Scherrer formula is rather high, thus it can only be seen as a rough estimation.

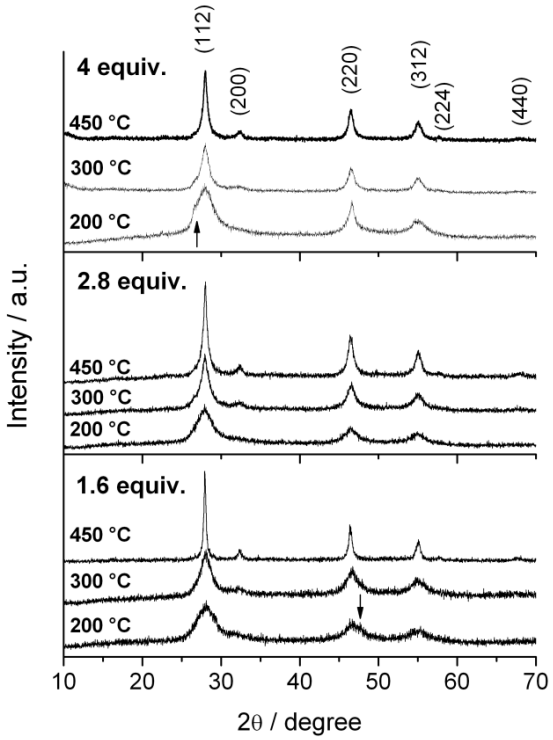

Figure 8: X-ray diffraction patterns of CIS samples prepared with 1.6, 2.8 and 4 equiv. of TU at different temperatures. Diffraction patterns are shifted vertically for better visibility. Arrows mark reflections, which do not belong to the chalcopyrite crystal structure.

Table 1: Crystallographic domain sizes of CIS powders synthesized at different temperatures and with different amounts of TU

equiv. of TU	Crystallographic domain sizes / nm		
	200 °C	300 °C	450 °C
1.6	5.0	6.4	23.4
2.8	6.7	8.7	13.8
4.0	5.8	9.9	12.9

It has to be noted that all CIS powders synthesized at 450 °C do not show any indication for impurities and can be regarded as single phase with chalcopyrite crystal structure based on the XRD analysis.

Samples prepared with 2.8 equiv. of TU show no extra reflections, indicating any secondary phases, independent from the synthesizing temperature. However, at low temperatures (200 and 300 °C) the co-existence of traces of amorphous secondary phases or minor impurities cannot be fully ruled out, due to the broadness of the reflections, caused by the low crystallinity of these powders.

XRD patterns of samples synthesized with 1.6 equiv. of TU and baked at 200 and 300 °C, show an unidentified secondary phase, indicated by a not completely symmetrical (220) reflection – marked with (↓). We assume, that the amount of thiourea within these samples is not sufficiently high enough to result in a complete coordination of the copper and indium metal ions, therefore, different metal-complex species might be present. This leads to a non-uniform reaction across the film and to the formation of secondary phases.

Samples prepared at 200 and 300 °C with 4 equiv. of TU show a shoulder at the (112) reflection – marked with (↑) – which was already mentioned before several times in the literature.[86-89] It was observed, that these additional reflections were more pronounced when sulfur rich precursor solutions were used, which is consistent with our experiments. It was suggested, that they may, at least partially, derive from organic impurities like melamine, melamine acid or cyanuric acid[87] or from indium rich secondary phases ($CuIn_5S_8$, $CuIn_{11}S_{17}$, In_6S_7 or In_2S_3). In our case, it is very unlikely, that this shoulder is caused by indium rich phases as the used Cu/In-ratio should be sufficiently high. The possibility that copper rich phases (CuS, CuS_2 or Cu_7S_4) are responsible is improbably as the extra reflections occur only for the 4 equiv. sample at a synthesizing temperature of 200 and 300 °C. In contrast to inorganic phases, organic impurities like melamine, formed by the trimerisation of TU, seem very plausible. On the one hand the high concentration of thiourea in this series (4 equiv. of TU) could lead to a pronounced formation of this by-product and due to its decomposition temperature (> 280 °C) the impurity does not show up in samples prepared at 450 °C.

MS measurements

The formation of melamine from urea is a well known industrial process[90] and so the formation in CIS thin films with TU as sulfur source can be expected. During the preparation of CIS/polymer nanocomposite layers the formation of melamine, using a very similar precursor system for CIS, was already observed before.[91]

To prove the formation of melamine within the studies CIS material, direct insertion mass spectrometry (DI-MS) studies with electron impact (EI) were conducted. These measurements reveal the presence of a volatile compound with a molecular mass of 126.0653 Da in the sample with 4 equiv. TU. This mass corresponds well with the molecular formula of $C_3H_6N_6$ which has a calculated accurate mass of 126.0654 Da. To verify the result, a typical fragment ion of the compound with a mass of 85.0517 Da (calculated accurate mass: 85.0514 Da) was analyzed.

Additionally, it was observed that with decreasing amount of thiourea and increasing annealing temperature of the different samples, the formation of melamine diminishes.

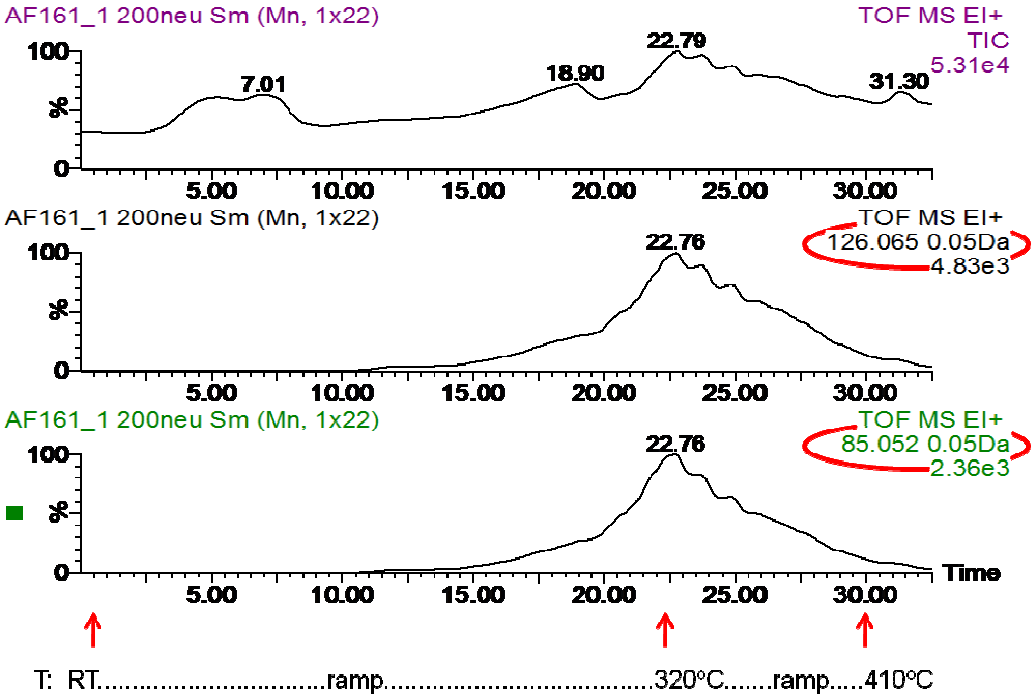

Figure 9: DI-MS Total ion chromatogram and selected ion traces of melamine in CIS thin films prepared at 200°C (4 equiv. TU) (top: total ion current, middle: ion trace molecular ion, bottom: ion trace fragment ion)

In situ GIWAXS and GISAXS analysis

Complimentary to the XRD analysis, the annealing process was studied by an in situ time resolved GIWAXS and GISAXS study using synchrotron radiation. For this, the phase formation was studied on a heating stage, which allowed simulating the annealing conditions described in the experimental part.

Results of the XRD analysis discussed above show that samples prepared at 200 °C have already a chalcopyrite type crystal structure. To obtain information about the temperature, at which the reaction – the decomposition of TU and the formation of CIS – starts, we performed a combined time-resolved GIWAXS and GISAXS study on spin coated precursor films in the temperature range from room temperature up to 190 °C.

GIWAXS patterns collected during the conversion of a precursor film with of 4 equiv. and 1.6 equiv. TU are shown in Figure 10.

At room temperature two sharp reflections at approximately 28° and 36° (marked with ↑) are visible, which might originate from TU- and TU/metal-complexes. This assumption is supported by the fact, that these reflections are more intense in the case of the sample with higher TU concentration within the precursor solution. During the heating run these reflections vanish in both cases and a peak at approx. 28 ° evolves, which can be assigned to the (112) reflection of the CIS chalcopyrite structure, based on results obtained by XRD analysis. In the case of the sample prepared with 4 equiv. TU, the evolving (112) reflection is much sharper, indicating a higher crystallinity than for the sample with the lower concentration of TU.

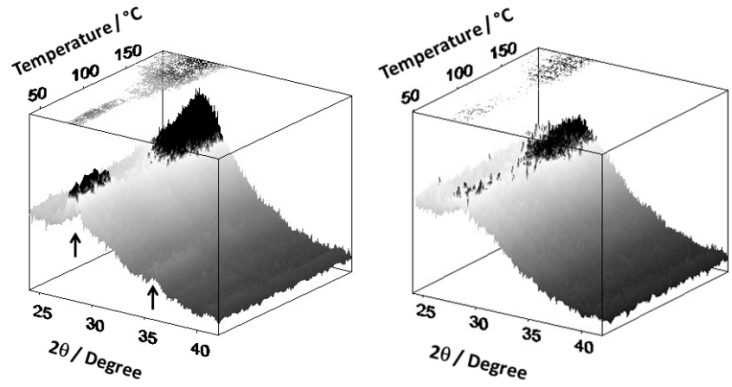

Figure 10: GIWAXS patterns with the corresponding contour plot on top of samples with 4 (left) and 1.6 equiv. of TU (right) showing the (112) reflection of the chalcopyrite structure obtained during the heating run with a heating rate of approx. 8 °C min^{-1}.

By plotting the Lorentz corrected integrated intensity ($\int dq \cdot q^2 \cdot I(q)$) from 26 ° -29 ° 2 θ versus the temperature (Figure 11), the thermal onset for the evolution of the (112) reflection can be estimated.

The slight variation in intensity between 80 and 130 °C can be assigned to the decomposition of TU- or TU/metal-complexes, whereas, the rapid increase in intensity above 130 °C derives from the appearance of the (112) diffraction peak.

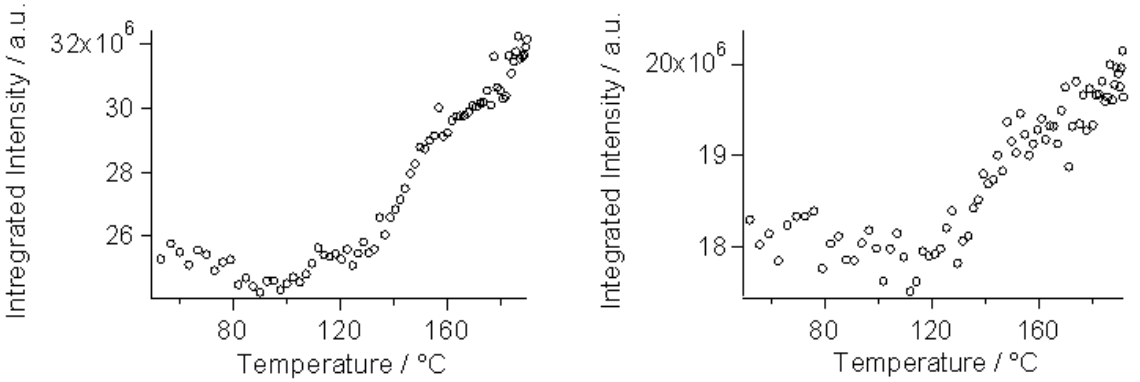

Figure 11: Lorentz corrected integrated intensity (4 equiv. of TU left, 1.6 equiv. of TU right) calculated from GIWAXS patterns of Figure 10 in the WAXS range between 26-29 ° 2θ, where the (112) reflection of chalcopyrite appears.

Interestingly this temperature, 130 °C, is much lower than the decomposition temperature of pure TU (approx. 190 °C) or metal salt/TU complexes[92,93] (200 °C), indicating a catalytic effect of pyridine within the metal salt/TU/pyridine complexes. This facilitates the decomposition of TU and the release of sulfur species to form the metal sulfide. Similar observations were made by Fan et al. for the formation of CuS, starting from a precursor solution using pyridine as a solvent.[94]

In order to investigate internal changes of the nanostructure of the films during the heating run, in situ GISAXS patterns have been recorded simultaneously with the GIWAXS measurements. Typical results, obtained from a sample with 4 equiv. of TU are shown in Figure 12a and 12b taken at room temperature and at 190 °C, respectively. Qualitatively the evolution of the GISAXS pattern over the temperatures is visualized in Figure 12c and 12d, in which the in-plane as well as the out-of-plane scattering is presented. Both have been obtained by integration over the boxes as indicated in Figure 12b. In both directions a strong increase of the scattering intensity with temperature is visible, which can be attributed to chemical and/or morphological changes as well as to the CIS formation. To quantify this observation, the out-of-plane data have been analyzed in detail. First the correlation

length,[95] which is proportional to a characteristic dimension of the nanoparticles/crystallites and defined by

$$l_m = 2\pi \int (q^2 \cdot I(q)dq) / \int (q^2 \cdot I(q)dq) \qquad (6)$$

has been determined. Secondly, for a profound analysis the data have been fitted with a generalized unified Guinier-exponential/power-law function[96] with polymeric constrain, in which a Porod term accounting for the surface roughness and large inhomogeneities was included. In addition for samples prepared with 4 equiv. TU a structure factor had to be included at a later stage, for which a hard-sphere interaction model[97,98] ($(S_{HSP}(q, R_{HSP}, p_{HSP}))$ was used. This was necessary to describe properly the scattering patterns. The whole equation writes as:

$$I_{GISAXS}(q_y, q_z) = G \cdot \left(\exp\left(-\left(\frac{q^2 \cdot R_g^2}{3} \right) \right) + \frac{2}{R_g^2} \cdot \left(\frac{\left(erf\left(\frac{q \cdot R_g}{\sqrt{6}} \right) \right)^3}{q} \right)^P \right) \cdot S_{Hsp}\left(q, R_{Hsp}, p_{Hsp}\right) + \frac{C_{por}}{q^{P_{por}}} \qquad (7)$$

in which q stands for the scattering vector calculated with $q = \sqrt{{q_y}^2 + {q_z}^2}$. The scattering vectors in-plane and out-of-plane are denoted with q_y and q_z, respectively. G corresponds to the Guinier prefactor and Rg to the radius of gyration. The parameter R_{Hsp} and p_{Hsp} are the hardsphere radius and the volume fraction of the hardsphere respectively and determines the structure factor. Both parameters have been fixed in the beginning (R_{HSp} = 3 nm and p_{Hsp} = 0) and were fitted only when the structure factor was visible in the scattering pattern. The parameters C_{por} and P_{por}, determine the power-law contribution of the surface roughness and large inhomogeneities. In this simplified approach the influence of refraction and correction terms of the DWBA-theory[99] have been neglected as only the structural progression was the main focus of the study.

The quality of the fit can be observed in Figure 13 in which the vertical GISAXS cuts are shown together with the fit.

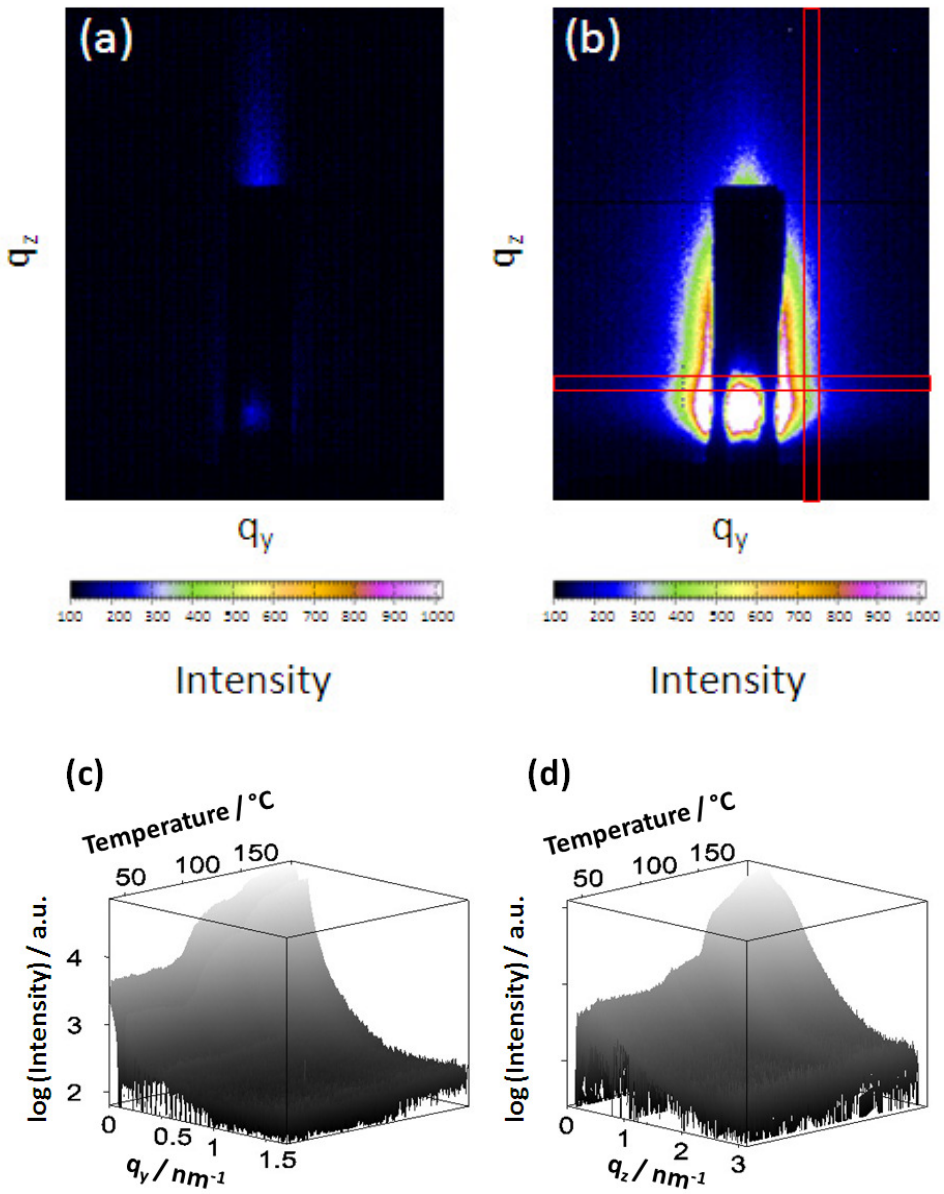

Figure 12: GISAXS patterns of samples prepared with 4 equiv. TU at room temperature (a) and at 190 °C (b). The red squares indicate the vertical and horizontal areas for integration (in-plane and out-of-plane scattering). Evolution of the in-plane scattering (c) and the out-of-plane scattering (d) as a function of temperature.

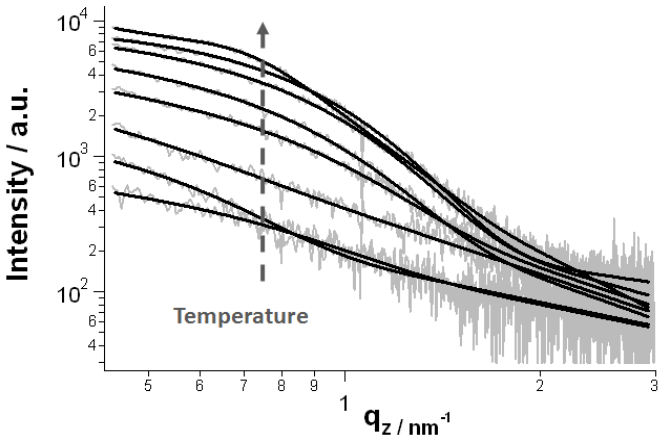

Figure 13: Vertical GISAXS cuts at different temperatures (73, 123, 138, 143, 168, 175, 181, 192 °C) for a sample with 4 equiv. TU and the corresponding fits. The position of interference shoulder caused by the structure factor is indicated with an arrow.

The qualitative behavior can be clearly identified in the correlation length l_m (Figure 14a and Figure 14d). Here the small increase of l_m indicates chemical or/and morphological changes within the precursor film prior the formation of CIS nanoparticles. At 130 °C a second sharp increase of l_m can be observed, which can be attributed to the growth of CIS crystallites. These results underline the findings from the XRD-measurements.

The determined normalized Guinier prefactor G/G_{max} over temperatures (Figure 14c and Figure 14f) quantifies the qualitative behavior as expected from GIWAXS and in- and out-of-plane GISAXS and manifests the increase of the electron density contrast and particle numbers caused by the CIS formation.

Assuming that the scattering structures are mainly caused by the crystalline phase, and in particular the smallest values of scattering objects are therefore the primary crystallites, the radius of gyration Rg of 3.4 (4 equiv. of TU) and 2.6 nm (1.8 equiv. of TU), should be related to the crystal dimensions. Assuming spherical CIS crystallites, the diameter can be calculated using the equation $d = 2 \cdot \sqrt{5/3} \cdot R_g$.[95] The obtained diameter of 8.8 and 6.7 nm, respectively, is in fairly good agreement to the diameter calculated from XRD measurements (6 and 5 nm), taking into account, that the Scherrer equation can only be seen as an estimation.

In addition, for samples prepared with 4 equiv. of TU, it can be clearly seen that the fit parameters p_{Hsp} and R_{Hsp}, i.e. the structure factor, show a sharp increase at approximately

180 °C, indicating changes in the morphology of the film: order of the CIS nanoparticles increases suddenly at this temperature.

Summing up the GIWAXS and GISAXS results, we conclude that CIS nanoparticles are already formed at temperatures above 130 °C, however some morphological or/and chemical changes take place already at 90 °C. The morphological changes occurring at 180 °C might be caused by the excess amount of TU in the samples with 4 equiv. as these observations were not observed in samples prepared with 1.6 equiv. TU. To provide evidence for this assumption, made on the basis of the GISAXS analysis, films synthesized at 160 and 220 °C were further studied with SEM.

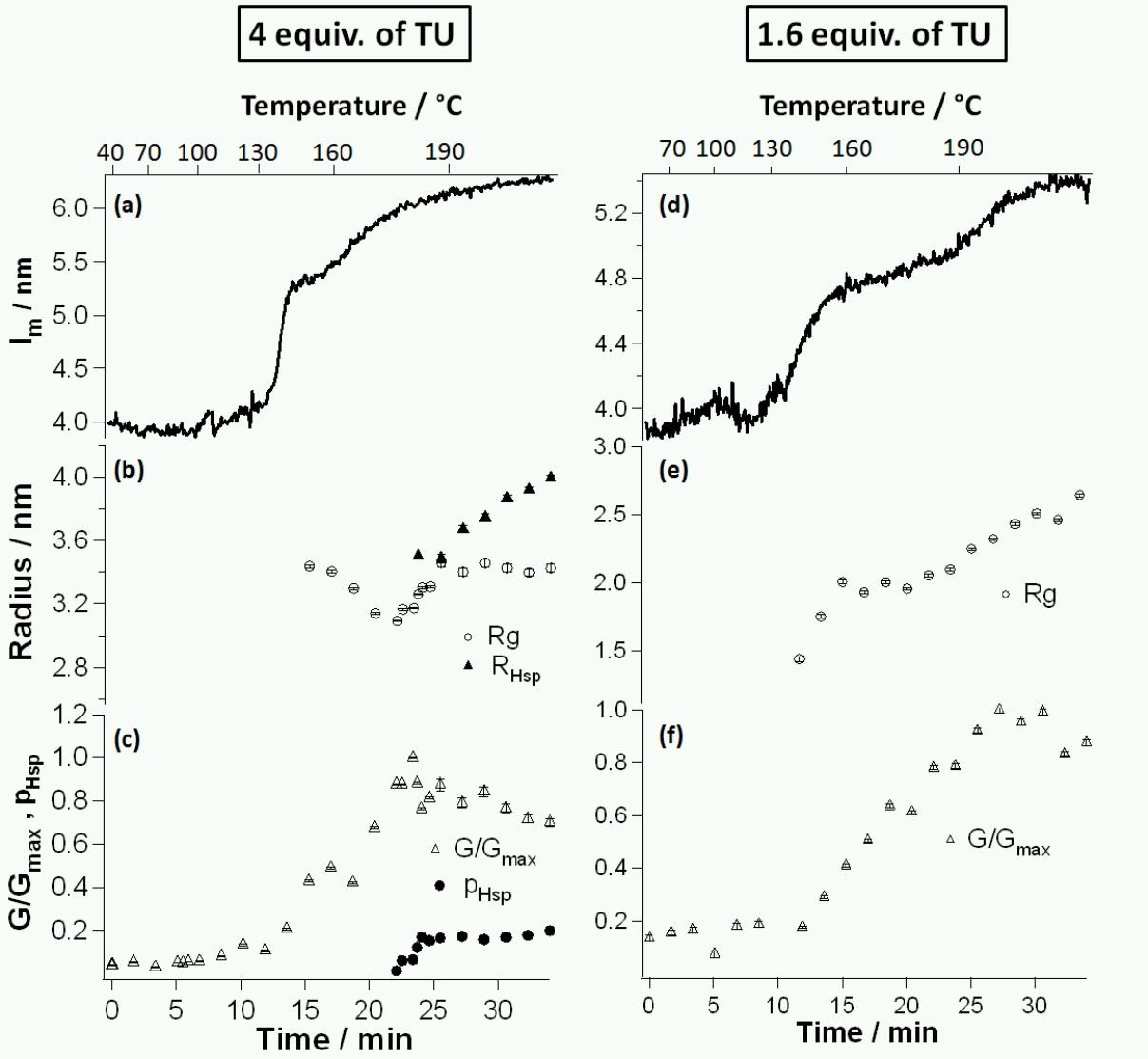

Figure 14: Evolution of l_m and fit parameters p_{Hsp}, G, R_g and R_{Hsp} for a sample prepared with 4 equiv. of TU ((a), (b) and (c)) and evolution of l_m and fit parameters G and R_g for a sample prepared with 1.6 equiv. of TU ((d), (e) and (f)) during the heating run.

Microstructure cross section

SEM cross sections of CIS thin films baked at 160 and 220 °C, respectively, are shown in Figure 15. These measurements demonstrate that the morphology of the films changes significantly between these two temperatures.

The non-uniform and cluster-like film at 160 °C turns into a compact film with an even surface at 220 °C. This observation confirms the result obtained by GISAXS measurements.

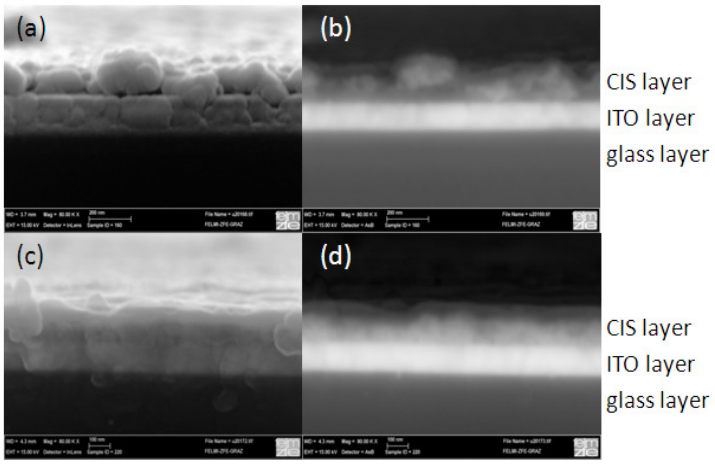

Figure 15: SEM micrographs of a cross-sectional view of a CIS layer synthesized at 160 °C (a, b) and 220 °C (c, d) recorded with a SE-inlens (SE) detector (left) and an angle selective backscattered electron (ASB®)-detector (right).

In order to reveal these changes at certain stages of the heating process simultaneous TG/MS analysis was performed.

Simultaneous TG/MS analysis

Samples were prepared by adding 25 µL of the CIS precursor solution into an Al_2O_3 crucible, which was then stored under vacuum at 60 °C for 8 hours. On the one hand, this temperature is low enough to avoid decomposition of the precursors and on the other hand, non-coordinated pyridine can be removed.

Figure 16 gives a comparison of the absolute mass loss of samples, prepared with different amounts of TU and Figure 17 shows an overlay of the simultaneous recorded TG trace and TIC trace of a sample prepared with 4 equiv. of TU. The first mass loss starts at approximately 80 °C and is mainly caused by evaporation of pyridine (bp. 115 °C) and acetic acid (bp. 118 °C), referring to MS data shown in Figure 18. Pyridine can be detected above

80 °C with its maximum evaporation rate at 120 °C, corresponding to its boiling point. It has to be noted, that all non-coordinated pyridine was removed during the sample preparation, therefore, it is very likely, that the evaporating pyridine derives from decomposing metal salt/TU/pyridine complexes. Acetic acid starts to evaporate at 105 °C with its maximum at 145 °C. This evolution of acetic acid is retarded in relation to its boiling point. Based on this result, the onset of the decomposition of the precursors can be identified at a temperature region between 80 and 105 °C. These results are in accordance with literature, where CuS was formed at 100 °C using a similar precursor solution (CuAc, TU, pyridine)[94] and with the GIWAXS and GISAXS results shown before. Interestingly, no volatile decomposition products of TU, like NH_3 and HCN can be found in this temperature range, despite the fact that evidence for the formation of CIS from 130 °C upwards is provided by GIWAXS analysis. This temperature is ideal from the operational point of view as it allows obtaining a stable precursor solution and a stable precursor film under ambient conditions, however, the formation of CIS requires only a mild thermal treatment.

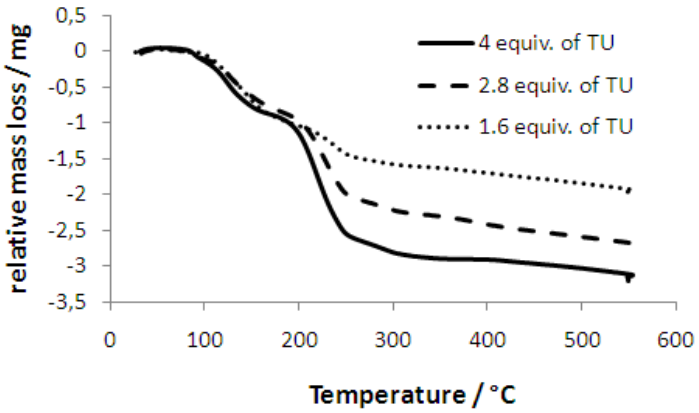

Figure 16: TG curves of samples prepared with 4, 2.8 and 1.6 equiv. of TU recorded in flowing helium at a heating rate of 8 °C min^{-1}. The sample mass is 4.5, 3.1 and 2.7 mg, respectively. The relative mass loss of the samples was referenced to the amount of metal ions within the sample.

The second mass loss between 180 and 260 °C differs remarkably between the samples. The higher the used amount of TU within the precursor solution the greater the mass loss. In addition, MS data indicate, that this weight loss could linked to the evaporation of typical decomposition products of TU[100] and TU/metal complexes.[93] Ion current traces with

molecular ion masses of 17, 27 and 26 can be observed which might be connected to NH_3, HCN and CS_2, respectively, as evolving gases (Figure 18) as well as by their characteristic ion fragments. However, for a precise identification, a more detailed MS study would be necessary.

Based on these results it can be concluded, that sulfur species, necessary for the formation of CIS, are primarily provided by coordinated TU at temperatures below 180 °C. This is also supported by the fact that the first mass loss is in the same range for all samples regardless of the used amount of TU. This is reasonable, because at this low temperature range (< 130 °C) the decomposition of TU has to be supported catalytically to be able to take place and to allow the release of sulfur species. This catalytical effect can be achieved by the formation of such complexes in combination with the coordinating solvent pyridine. Above 180 °C the temperature is sufficiently high for the decomposition of non-coordinated TU, which is consistent with values from the literature.[100] Supported by these results the morphological changes observed in cross-sectional SEM micrographs of thin films and during GISAXS measurements can be clearly linked to the decomposition of non-coordinated TU. Additionally, this explains why samples with only 1.6 equiv. of TU do not show such a pronounced change in morphology at 180 °C during GISAXS analysis, as these samples possess hardly any non-coordinated TU.

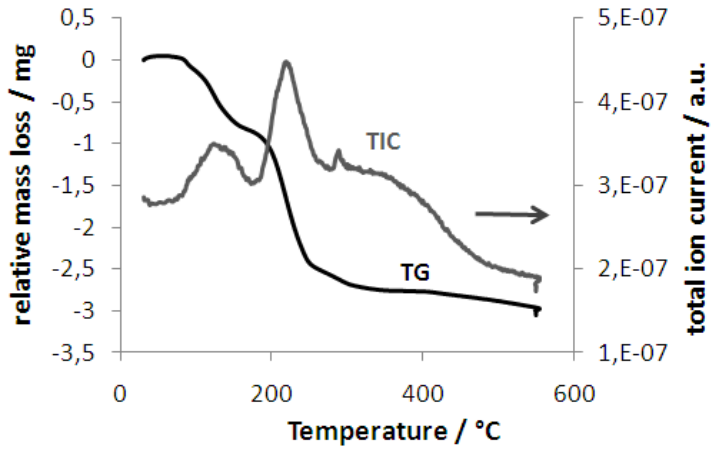

Figure 17: TG curve (black) and total ion current (TIC) trace (gray) of a sample prepared with 4 equiv. of TU. The measurement was done in helium atmosphere with a heating rate of 8 °C min^{-1} by simultaneous TG/MS. The sample mass is 4.5 mg.

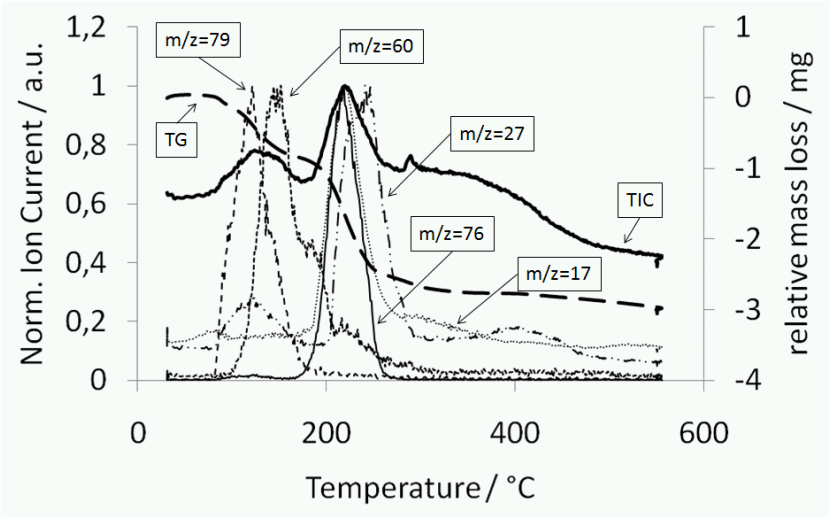

Figure 18: Ion current vs. temperature curves of molecule ions in the identified gases evolved of a sample prepared with 4 equiv. of TU as measured in helium with a heating rate of 8 °C min^{-1} by simultaneous TG/MS.

Chemical composition

The elemental composition was determined using TEM-EDX analysis. Figure 19 shows the atomic percentage of the elements for the synthesized CIS samples. The atom percentages were calculated using the Cu K, Zn K, Sn L, and S K peaks using the Cliff-Lorimer approximation.[101] The elemental ratios of Cu/In and S/(Cu+In) are summarized in Table 2. All CIS powders possess nearly stoichiometric amounts of sulfur, with a S/(Cu+In) ratio varying between 0.93 and 1.11, independent from the amount of TU within the precursor solution or the synthesizing temperature. Nearly all samples show a lower Cu/In ratio than in the precursor solution. These deviations from the starting composition might be caused by a preferred generation of volatile Cu-species during the thermal induced CIS formation. These observations have also been also made by Krunks et al.[86] when they used Cu-rich precursor solutions. Despite this effect, the powders are still of Cu-rich nature in our case, yielding CIS with p-type conductivity.[44]

Table 2: Elemental ratios of the CIS powders synthesized at different temperatures calculated from TEM-EDX measurements.

T / °C	Elemental ratio					
	1.6 equiv. TU		2.8 equiv. TU		4 equiv. TU	
	Cu/In	S/(Cu+In)	Cu/In	S/(Cu+In)	Cu/In	S/(Cu+In)
200	1.69±0.51	1.11±0.07	1.29±0.11	1.10±0.08	1.00±0.18	0.95±0.07
300	1.93±0.26	0.93±0.06	1.22±0.04	1.04±0.03	1.34±0.09	1.01±0.04
450	1.17±0.08	1.05±0.06	1.14±0.15	1.03±0.08	1.09±0.04	1.09±0.04

In contrast to CIS powders prepared with 2.8 and 4 equiv. of TU the stoichiometry of samples prepared with 1.6 equiv. of TU varies significantly, especially at low synthesizing temperatures. We assume, that this non-uniform elemental distribution across the film is caused by an incomplete coordination of the copper and indium ions by TU (see discussion of XRD analysis).

Samples prepared at 200 °C exhibit chlorine as an impurity, which may derive from not yet removed decomposition products of the precursor at this stage. However, at higher synthesizing temperatures (> 300 °C) the chlorine content is significantly reduced and samples prepared at 450 °C can be regarded as chlorine-free.

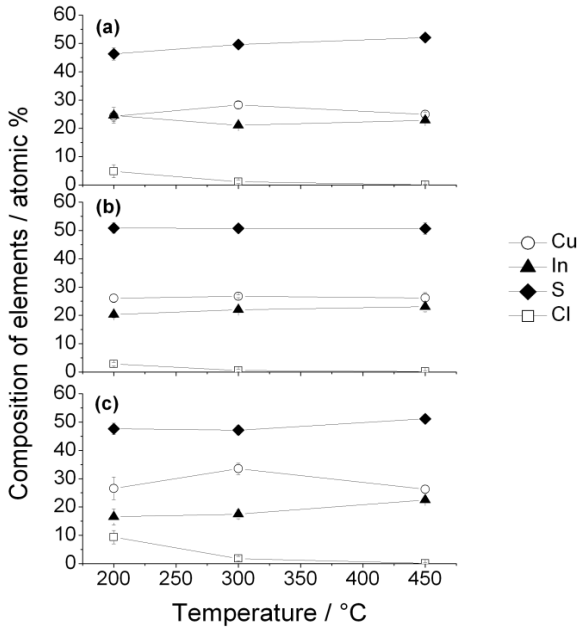

Figure 19: Chemical composition of CIS powders prepared with 4 (a), 2.8 (b) and 1.6 (c) equiv. of TU in the precursor solution.

Optical properties

The optical properties of the synthesized CIS films were studied by transmittance and reflectance measurements. The absorption coefficient (α) was calculated according to following equation:[102,103]

$$\alpha = \frac{1}{d}\ln\left(\frac{1-R}{T}\right) \qquad (8)$$

where d is the thickness of the film, R the reflectance and T the transmittance of the film. The film thickness was determined using a surface profiler.

Figure 20 gives the typical absorption spectra obtained for CIS samples synthesized at different temperatures using 2.8 equiv of TU within the precursor solution. In general, it can be seen, that all films show a high optical absorption (> 10^4 cm^{-1}) between 850 and 350 nm and very similar absorption spectra independent of the syntheses parameters.

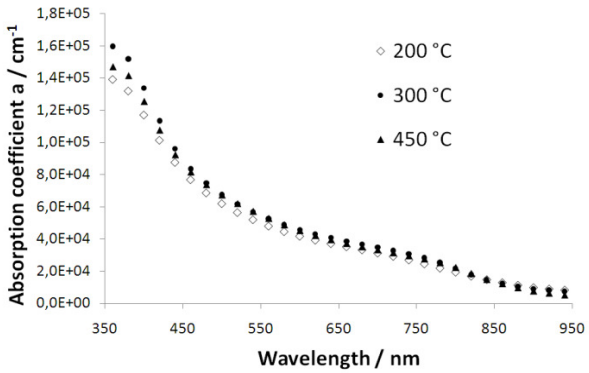

Figure 20: Optical absorption coefficient of CIS films synthesized with 2.8 equiv TU and baked at different temperatures.

The optical band gap (Eg) values were obtained from the equation:

$$\alpha = \frac{A(h\upsilon - E_g)^n}{h\upsilon} \qquad (9)$$

where A is a constant, (hν) the photon energy and n an exponent, which is equal to 2 or ½ for indirect or direct transition, respectively. In the present work n was found to be ½ indicating a direct band gap, which is consistent with the literature.[89] Therefore, the band

gap values were estimated from the $(\alpha h\nu)^2$ versus ($h\nu$) plots by extrapolating the linear part of the function as shown in Figure 21. Table 3 gives a summary of the estimated optical band gaps of the prepared CIS films.

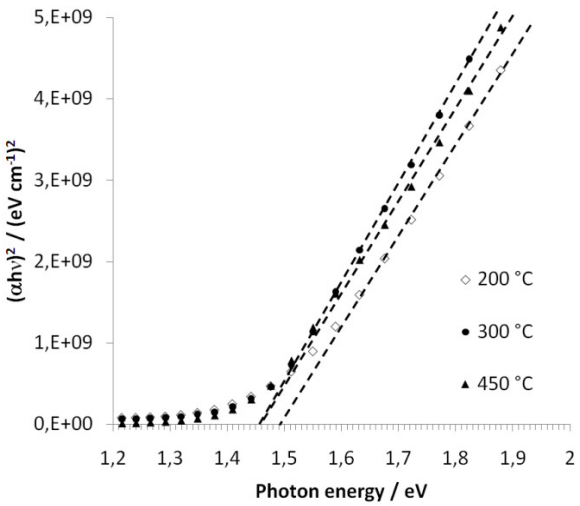

Figure 21. $(\alpha h\nu)^2$ vs. photon energy ($h\nu$) of CIS films prepared with 2.8 equiv TU and baked at different temperatures.

Table 3: Estimated optical band gaps from $(\alpha h\nu)^2$ vs. photon energy ($h\nu$) plots of prepared CIS films

equiv. TU	Band gap / eV		
	200 °C	300 °C	450 °C
1.6	1.51	1.46	1.48
2.8	1.47	1.47	1.45
4	1.49	1.46	1.46

The obtained band gaps range from 1.45 to 1.51 eV and do not show a strong dependence on the synthesizing temperature or the amount of TU used in the precursor solution. The band gap values are consistent with literature.[89,104,105]

2.2.4 Conclusion

In this chapter the preparation of CIS thin films by a solution based method using copper(I) acetate and indium(III) chloride as metal salts, TU as sulfur source and pyridine as solvent is presented. The films exhibit very beneficial properties for photovoltaic applications as they possess a chalcopyrite crystal structure, a near ideal band gap and a high absorption coefficient. Additionally, the formation process, taking place during the thermal conversion of the precursor layer, was studied intensively (Figure 22): At the beginning the precursor layer consists of metal salt/TU/pyridine complexes embedded into a matrix of TU. The dimensions of this matrix depend on the equivalent of TU used for the preparation of the precursor solution. At 90 °C these metal salt/TU/pyridine complexes start to decompose followed by the formation of CIS nanoparticles within the TU matrix at 130 °C. This temperature range is much lower than for non-coordinated TU (> 190 °C) indicating a catalytic effect of pyridine. The TU matrix decomposes at 180 °C, which causes the formation of a dense CIS thin film. Hence, it can be concluded that the formation of CIS is primarily linked to the decomposition of TU originating from metal salt/TU/pyridine complexes. In addition, mass spectrometry studies of CIS powders reveal that melamine is formed as a by-product, especially when high concentrations of TU are used in the precursor solution. However, using synthesizing temperatures above the decomposition temperature of melamine (280 °C), leads to melamine free CIS thin films.

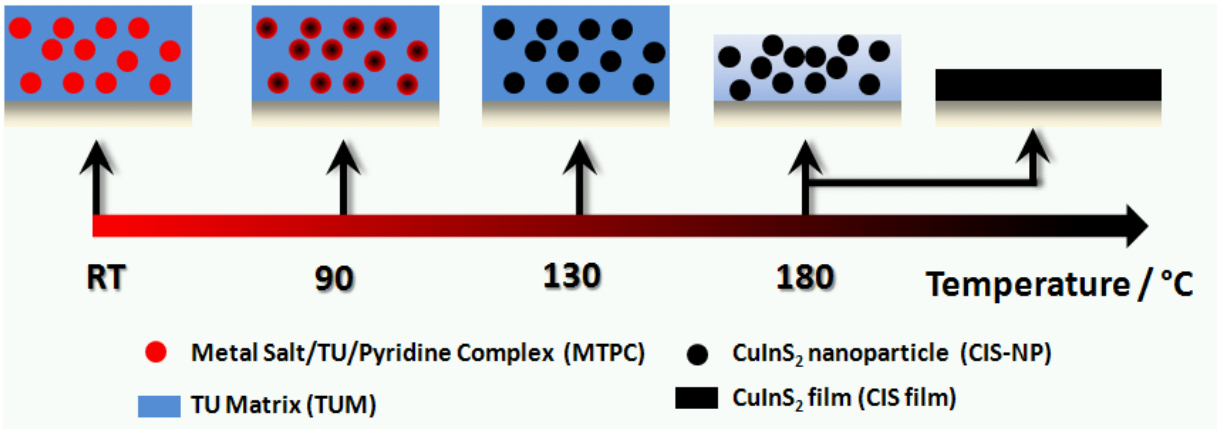

Figure 22: Events occurring during the heating process and the formation of the CIS thin films.

2.3 Cu_2ZnSnS_4 thin films

2.3.1 Introduction

The family of $Cu(In,Ga)(S,Se)_2$ semiconductors has already demonstrated its potential for photovoltaic applications, however, concerns, regarding a large scale production are raised. Especially the extremely low concentration of In and Ga (less than 0.05 ppm) within the earth crust[106] represent a serious bottleneck. Forecasts for existing chalcogenide based solar cell technologies predict a maximum energy production of less than 100 GW per year,[107] due to limitation of raw materials for the fabrication of these cells. Compared to the overall energy consumption in approximately 40 years (30 TW)[1], 100 GW are only a marginal fraction. Triggered by these limitations, the chalcopyrite-type semiconductor Cu_2ZnSnS_4 (CZTS) attracts more and more scientific interest in the last three years. In this case, In and Ga are substituted by Zn and Sn and Se is replaced by S, therefore, this material consists only of abundant, cheap and non-toxic elements.[108] The concentrations of Zn and Sn within the earth crust, 75 and 2.2 ppm, exceed the content of In by more than 1500 and 44 times respectively.[106] In addition, the combination of an ideal direct band gap of about 1.4 – 1.5 eV[109-111] and a high optical absorption coefficient ($< 10^4$ cm^{-1})[112] allows to harvest a high percentage of the incoming photons. Based on this data, the theoretical maximum energy conversion efficiency for single junction devices using CZTS should be as high as for CIS (28.5 %). Up to now record conversion efficiencies of CZTS based thin film solar cells nearly reach 10 % using a liquid based process for the preparation of the CZTS layer.[107] Bearing in mind, that CZTS is only studied intensively for the last three years, this conversion efficiency is quite remarkable. In general, the preparation methods for CZTS thin films can be roughly divided into vacuum-based and non-vacuum based approaches. In both cases CZTS can be deposited directly or formed by sulfurization of deposited precursors. Vacuum-based methods include evaporation techniques[113-118] and sputtering techniques.[119-121] Non-vacuum approaches involve chemical methods like electrochemical deposition,[108,122-124] photo-chemical deposition,[27] sol-gel deposition,[125] sol-gel spin-coated deposition[29,126,127] and spray

pyrolysis.[128-132] In addition, to these methods CZTS thin films were also prepared from CZTS nanocrystals, which were prepared by a colloidal synthesis routes.[39,133]

From the economical point of view, solution based non vacuum preparation methods are very interesting as large homogeneous films can be prepared, using simple application methods as spin coating, spraying or doctor blading.

In our case, we adapted the preparation method used for the fabrication of CIS thin films (2.2). Commercially available metal salts are used as metal precursors and the solvent pyridine remaines, due to its ability to reduce the decomposition temperature of the precursors. However, the sulfur source was changed from TU to thioacetamide (TAA) to inhibit the formation of melamine, which remains within the semiconducting layer at temperatures below its decomposition temperature (> 280 °C).

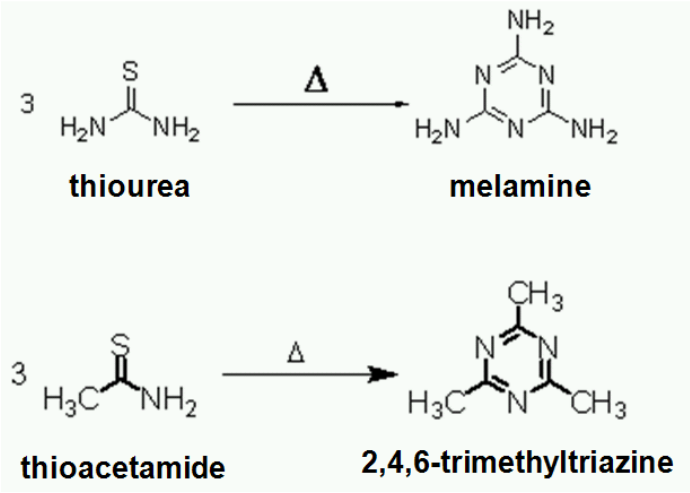

Figure 23: Trimerisation reaction of thiourea and thioacetamide leading to the occurrence of melamine and 2,4,6-trimethyltriazine during the CZTS film formation.

The trimerisation reaction,[87] which leads to the formation of melamine (Figure 23), is still expected to take place for TAA, however, the formed 2,4,6-trimethyltriazine has a very low boiling point (156 °C)[134] and can be removed easily from the semiconducting layer during the thermal treatment.

Additionally, the influence of different synthesizing temperatures and amounts of TAA was evaluated using various analytical methods: X-ray diffraction (XRD), optical absorption spectroscopy, energy dispersive X-ray spectroscopy (EDX), scanning electron microscopy (SEM) and a surface profiler. To gain a better insight into the early stages of formation of

CZTS films and to determine the temperature, at which the CZTS formation starts, an in situ time and temperature resolved synchrotron X-ray analysis is performed.

2.3.2 Experimental

Chemicals

Copper (I) iodide (CuI, 99,999%), zinc (II) acetate ($ZnAc_2$, 99,99%), tin (II) chloride anhydrous ($SnCl_2$, ≥97%), thioacetamide (TAA, 99+%) and pyridine (reagent plus ≥99%) were purchased from Sigma Aldrich and used without further purification.

Indium tin oxide- (ITO)-coated glass substrates with a surface resistivity of 15-25 Ω/cm^2 were purchased from Delta Technologies Ltd.

Sample preparation

ITO-coated glass substrates were cleaned in an ultrasonic water bath followed by an ultrasonic isopropanol bath, each for 20 min. The CZTS precursor solution consisted of CuI (0.32 mol/L), $ZnAc_2$ (0.16 mol/L), $SnCl_2$ (0.16 mol/L) and TAA (3.2 mol/L or 2.2 mol/L) dissolved in pyridine. The solution was then spin coated at a speed of 1500 rpm on the substrates, which were then baked for 15 min at different temperatures in the range of 180 – 450 °C (heating rate 21 °C/min) under vacuum to form the CZTS-layer. After the heat treatment the samples were cooled down to room temperature under vacuum within 10 min.

For XRD analysis and TEM-EDX measurements the CZTS-precursor solution was sprayed onto glass substrates at ambient conditions, followed by the same heat treatment of the substrates as described above. Finally the µm thick CZTS layer was scraped off the glass substrate to obtain the CZTS powder.

Characterization

The X-ray powder diffraction profiles were measured with a Siemens D-5005 powder diffractometer (θ/θ geometry, Cu Kα radiation, graphite monochromator, scintillation counter, step width 0.02 °, constant counting times of 10 s/step, measured range of 20 - 60 ° in 2θ). The diffraction patterns were fitted by full-profile Rietveld refinements using the program system TOPAS 3. The calculations included least-squares refinements of the profile

parameters (lattice constants, sample height, six parameters for Pseudo-Voigt approximations of the peak profiles and – in separate cycles – the crystallographic domain sizes) as well as structural data (positional and displacement parameters, occupancies). Transmittance and reflectance spectra of the thin films were measured with a Lambda900 spectrometer (Perkin Elmer) including an external integrating sphere diffuse reflectance accessory (PELA-1000). The surface morphology was studied with a Veeco Dektak 150 surface profiler and a JEOL JSM-5410 scanning electron microscope equipped with a secondary electron detector. Energy dispersive X-ray (EDX) spectra were recorded in scanning transmission electron microscopy (STEM) mode using a Philips CM20/STEM operated at 200 kV with a LaB_6 cathode equipped with a Noran HPGe-detector. Simultaneous 2D grazing incident small angle X-ray scattering (GISAXS) and 1D gracing incident wide angle X-ray scattering (GIWAXS) measurements were performed at the Austrian SAXS Beamline 5.2L of the electron storage ring ELETTRA (Italy).[84] The beamline has been adjusted to a q-resolution ($q=4\pi/\lambda*\sin(2\theta/2)$) between 0.1 and 3.1 nm^{-1} (GISAXS) and to resolve the angular range (2θ) between 21.1 ° and 41.8 ° (GIWAXS) using an X-ray energy of 8 keV. The glass/ITO/precursor-substrates were placed in a custom made sample cell with a grazing angle of about 0.18 ° and were heated from 40 °C up to 180 °C at a heating rate of approx. 8 °C/min in vacuum. During the temperature scan, data were recorded with 5 s and 10 s resolution for GISAXS and GIWAXS, respectively.

2.3.3 Results and Discussion

Sample preparation

Precursor solutions were prepared from metal salts (copper(I) iodide, zinc(II) acetate, tin(II) chloride) and TAA in pyridine. To investigate the influence of the synthesizing temperature and of the amount of sulfur source on the formation of CZTS, samples with two different amounts of TAA, each annealed at four different temperatures, were prepared. From literature reports it is known, that an excess of thiourea is necessary to compensate the loss of sulfur during pyrolysis [112,135]. Therefore, two series of solutions containing 3.5-fold and 5-fold of stoichiometric amount of TAA were prepared. The metal salts were applied using the stoichiometric ratio of Cu:Zn:Sn of 2:1:1. The solutions were spin coated or

sprayed onto glass substrates, which were then baked at different synthesizing temperatures between 180 °C and 450 °C to obtain CZTS thin films.

X-ray diffraction

For all samples we observed the major characteristic X-ray diffraction peaks (112), (200), (220), (312) for the kesterite type structure of CZTS[136] (Figure 24), which shows the close relationship of the kesterite structure with the cubic sphalerite type sub-structure. As ZnS and Cu_2SnS_3 have a very similar crystal structure[137] it is not possible to exclude the presence of those phases. However, the XRD patterns obtained at 350 °C and 450 °C also show the minor superstructure reflections of the kesterite CZTS (110), (202), (211), (114), (105) and (224), due to the high crystallinity of these powders. The positions of the reflections are in good agreement with the literature values of crystalline CZTS (kesterite), according to the Powder Diffraction File (PDF) 26-0575 of the International Centre for Diffraction Data. However, a differentiation of CZTS from Cu_2SnS_3 was only possible by the EDX analysis of the chemical composition (see below).

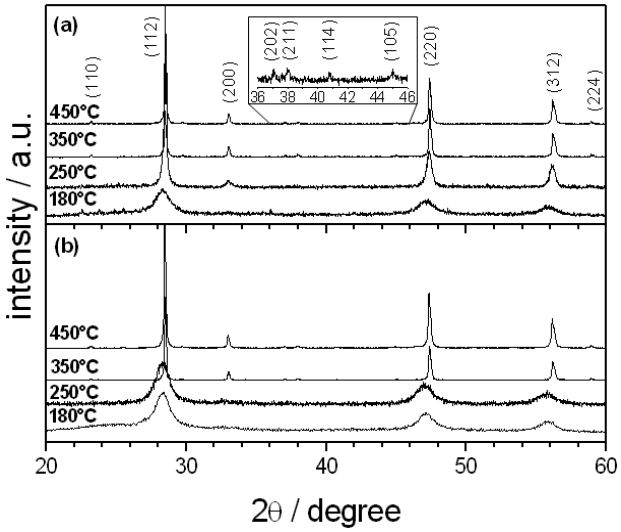

Figure 24: X-ray diffraction patterns of CZTS samples prepared with 5 equiv TAA (a) and 3.5 equiv TAA (b) at different temperatures. Diffraction patterns are shifted vertically for better visibility.

As Schorr et al.[138] showed by neutron diffraction studies, that CZTS crystallizes in the kesterite type structure, we assume that the here prepared samples are of kesterite nature. However, it is not possible to distinguish between the Cu and Zn positions in the Cu-Zn layer in the kesterite type structure with laboratory XRD data, due to the very similar scattering

factors of Cu and Zn. Therefore, the presence of stannite as possible modification, which has a very similar structure to kesterite,[139,140] cannot be fully ruled out.

In contrast, we were able to determine the exchange ratio of the Cu and Sn cations at their respective sites by Rietveld methods, since the scattering curves for these elements differ significantly. Generally, the calculated XRD patterns showed an excellent agreement with the measured data (Figure 25). Above 180 °C no additional peaks, corresponding to any secondary phase, can be seen, indicating, that the CZTS powders are single phase. Only powders obtained at 180 °C sometimes showed some very weak unidentified reflections, which may reveal not removed reaction side products at this temperature. This is in contrast to earlier reports where TU was used as sulfur source.[127,141] In these cases no CZTS single phase could be obtained at low temperatures.

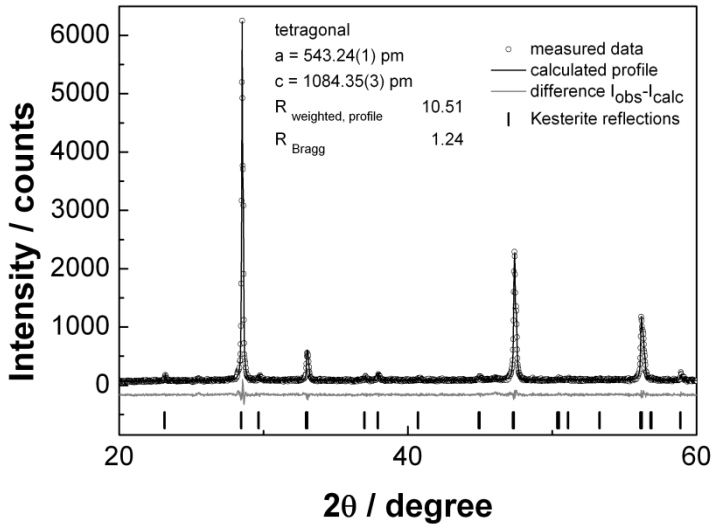

Figure 25: Results of the Rietveld refinement of the diffraction data for a sample with 5 equiv. TAA synthesized at 350 °C; The peaks are in good agreement with the structure of kesterite CZTS (PDF 26-0575 – sharp lines at the bottom).

The primary crystallite sizes of the powders rise significantly with increasing synthesizing temperature, as all reflexes get sharper, which can also be seen from the domain size calculated using Scherrer formula, implemented in the TOPAS program system (Table 1). The uncertainty of these calculation is relatively high, thus, it only can be a rough measure for the crystallite diameters. The data for the samples, prepared at higher temperatures, are in a comparable range and their differences should not be over-interpreted. However, there is

a significant difference of the domain sizes at 350 °C and 450 °C as compared with those of the low-temperature samples.

CZTS powders, synthesized with only 3.5 equiv. TAA instead of 5 equiv. TAA, show the same purity and crystal structure (kesterite). The only difference can be seen in the domain size of the samples. Powders at 180 °C can be regarded as nanocrystalline in both cases with an average size of 8 nm. However, samples containing 5 equiv. of TAA, prepared at 250 °C show significantly larger crystallites (35 nm) than the sample with 3.5 equiv. (8 nm). For higher temperatures highly crystalline powders are obtained in both cases with primary crystallite diameters between 100 and 160 nm.

The lattice parameters of the synthesized CZTS powders (Table 4) were obtained by the Rietveld refinements of the X-ray diffraction data. The data for the samples prepared at 350 °C and 450 °C, respectively, are in good agreement with the values of a = 0.5427 nm and c = 1.0848 nm, reported by Schaefer et al.[136] Samples at and below 250 °C show slightly larger lattice constants, mainly due to a cation disorder within the CZTS crystals at this temperature, leading to an expansion of the unit cell and a more or less statistically cation distribution on all possible sites.

Table 4: Lattice parameters and crystallographic domain sizes of CZTS powders synthesized at different temperatures and with different amounts of TAA.

Sample	a / nm	c / nm	V / nm^3	d / nm*
5 equiv. TAA				
180 °C	0.5436(7)	1.095(3)	0.324(1)	8
250 °C	0.5438(1)	1.0841(4)	0.3206(2)	35
350 °C	0.54322(1)	1.08434(3)	0.31998(2)	156
450 °C	0.54335(1)	1.08496(4)	0.32032(2)	134
3.5 equiv. TAA				
180 °C	0.5442(5)	1.097(2)	0.3249(8)	8
250 °C	0.5438(4)	1.102(2)	0.3259(7)	9
350 °C	0.54313(2)	1.08454(5)	0.31993(2)	135
450 °C	0.54350(1)	1.08530(4)	0.32060(2)	100

* according to Debye-Scherrer equation, refined by TOPAS [142].

This assumption is confirmed by the refinement of the positional parameters of the sulfur atoms, which showed that the anions are located at x = y = ¾ at lower temperatures, resulting in equal metal-sulfur distances for the Cu/Zn (Cu-S, Zn-S: 233 pm) as well as for the Cu/Sn layers (Cu-S, Sn-S: 240 pm) in the structure of kesterite (Table 5). At higher temperatures the positional parameters of the sulfur atoms differ significantly from ¾, leading to distances of Cu1-S: 234 pm (236 pm), Sn1-S: 247 pm (244 pm), Cu2-S: 241 pm (240 pm) and Zn-S: 220 pm (222 pm) for the 350 °C samples (the distances for the 450 °C samples are given in parenthesis; all standard deviations are equal or less than 1 pm). Figure 26 shows the elemental cell derived from XRD data from a sample with 5 equiv. TAA synthesized at 350 °C. The interatomic distances do not differ significantly regarding the 3.5 equiv. TAA and 5 equiv. TAA samples.

Table 5: Positional and site occupancy parameters of kesterite CZTS (350 °C, 5 equiv TAA). The mixed site occupancies of all samples were refined and are given in the lower part of this table.

Site	x	y	z	Occupancy *
Cu1A	0	0	0	0.861(9)
Cu1B	½	½	½	0.139
Sn1A	½	½	½	0.861
Sn1B	0	0	0	0.139
Cu2	0	½	¼	1
Zn1	½	0	¼	1
S1	0.777(2)	0.744(3) **	0.8670(7)	1

	occ (Cu1A) = occ(Sn1A)	occ (Cu1B) = occ(Sn1B)
5 equiv TAA		
180 °C	0.7(1)	0.3
250 °C	0.6(1)	0.4
350 °C	0.861(9)	0.139
450 °C	0.84(1)	0.16
3.5 equiv TAA		
180 °C	0.7(1)	0.3
250 °C	0.6(1)	0.4
350 °C	0.84(1)	0.16
450 °C	0.834(1)	0.166

** The occupancy parameters have been set to a sum of 1. During the refinement of the occupancies the thermal displacement parameters of the Cu1A, Cu1B, Sn1A and Sn1B atoms have been constrained and refined with a single value.*

*** The positional parameters of S1 are nearly identical in the samples heated to 350 °C and 450 °C, both for 3.5 equiv. TAA and 5 equiv. TAA. In the 180 °C and 250 °C samples the refinement shifted these parameters to the ideal value of ¾ for an disordered cubic ZnS (sphalerite) type sub-structure.*

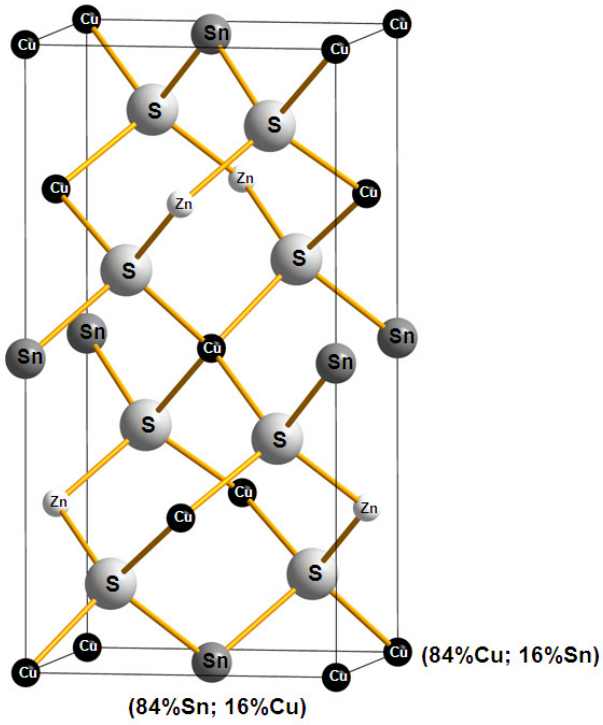

Figure 26: Elemental cell derived from XRD data from a sample with 5 equiv. TAA synthesized at 350 °C. The Cu/Sn-layers show a slight cation disorder. 16 % of the Cu-cations are displaced by Sn-cations and vice versa.

***In situ* GIWAXS and GISAXS analysis**

The XRD-results discussed above show that samples prepared at 180 °C have already a kesterite-type crystal phase. In order to obtain information at which temperature the reaction – the decomposition of TAA and the formation of CZTS – starts, we performed a combined time-resolved grazing incident small and wide angle X-ray scattering (GISAXS and GIWAXS) study on thin films in the temperature range from ambient temperature up to 180 °C.

GIWAXS patterns collected during the conversion of a precursor film containing 5 equiv TAA are shown in Figure 27. Above 105 °C a peak at approx. 28 ° evolves, which corresponds to the (112) diffraction peak of CZTS kesterite structure. The slight shift of the (112) peak to smaller angles was also observed during powder-XRD measurements at lower temperatures. As already mentioned, the co-existence of similar phases, like Cu_2SnS_3 or ZnS, cannot be fully excluded. However, experimental results from TEM-EDX and XRD analysis show a strong indication, that CZTS with kesterite structure is formed, as all samples possess approximately the expected chemical composition for CZTS and powders prepared at high synthesizing

temperatures (350 °C and 450 °C, Figure 24) exhibit also the minor superstructure reflections for the kesterite crystal structure. Therefore, we interpret the evolving peak at approx. 28 ° as the (112) reflection of the kesterite structure. By plotting the Lorentz corrected integrated intensity ($\int dq \cdot q^2 \cdot I(q)$) from 25 ° - 32 ° 2θ versus the temperature (Figure 28), the onset for the formation of CZTS can be estimated.

The decrease in intensity from 60 °C to 100 °C derives from the decomposition of TAA and TAA-complexes, whereas, the sharp increase in intensity above 105 °C is assigned to the appearance of the (112) diffraction peak. Based on these results, the formation of CZTS from the metal- and sulfur-precursors starts at around 105 °C.

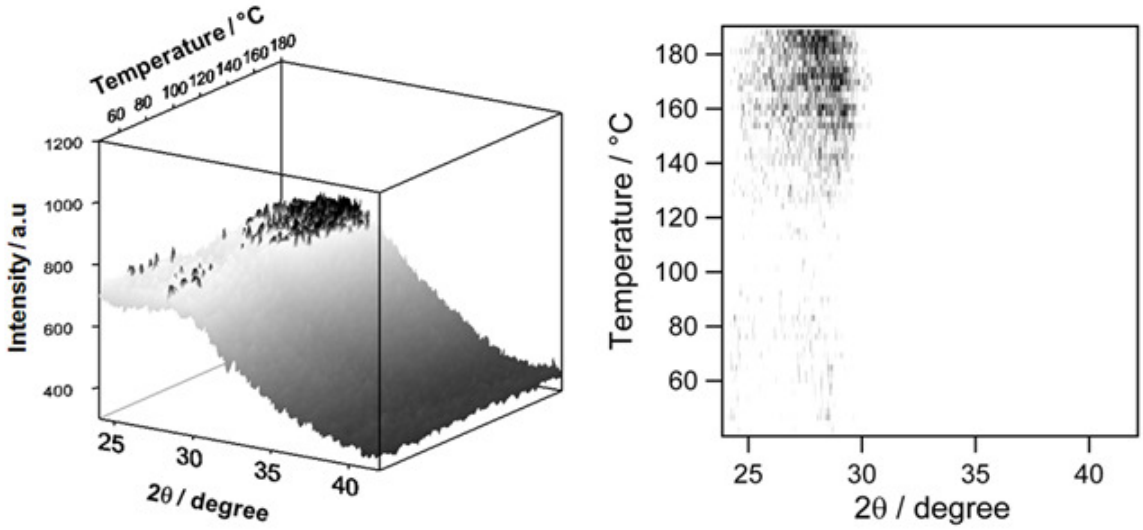

Figure 27: GIWAXS patterns of a sample containing 5 equiv. TAA showing the (112) reflection of kesterite obtained during heating from 40 to 180 °C with a heating rate of 8 °C/min (left) and corresponding contour plot (right).

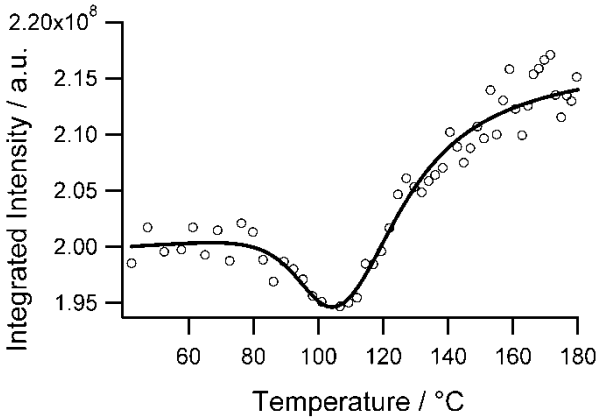

Figure 28: Lorentz corrected integrated intensity calculated from GIWAXS patterns of Figure 27 in the WAXS range between 25-32 ° 2θ, where the (112) reflection of kesterite appears. Black line is drawn as a guideline for the eye.

In order to probe the internal nanostructure of the films, in situ GISAXS patterns have been taken simultaneously with the GIWAXS measurements. Typical results, obtained from a sample with 5 equiv. TAA, are shown in Figure 29a and Figure 29b taken at ambient temperature and at 165 °C, respectively. Qualitatively the evolution of the GISAXS pattern over the temperatures is visualized in Figure 29c and Figure 29d, in which the in-plane as well as the out-of-plane scattering is presented. Both have been obtained by integration as indicated with the red boxes in Figure 29a. Here, a strong increase of the scattering intensity with temperature is visible. In particular between 80 °C and 120 °C the growth of the nanostructures as well as the increase of surface roughness, which occurs in both directions (in-plane and out-of-plane), can be paralleled with the decomposition of TAA and TAA-complexes and the following growth of the CZTS crystallites, observed in the GIWAXS data. For quantification, the out-of-plane data have been analyzed in detail and, therefore, have been fitted with a generalized unified Guinier-exponential/power-law function[96] with polymeric constrain, in which a Porod term accounting for the surface roughness and large inhomogeneities was included. The whole equation writes as

$$I_{GISAXS}(q_y, q_z) = G \cdot \exp\left(-\left(\frac{q^2 \cdot R_g^{\,2}}{3}\right)\right) + \frac{2 \cdot G}{R_g^{\,2}} \cdot \left\{\left[\operatorname{erf}\left(\frac{q \cdot R_g}{\sqrt{6}}\right)\right]^3 \Big/ q\right\}^P + \frac{C_{por}}{q^{P_{por}}} \qquad (10)$$

in which q stands for the scattering vector calculated with $q = \sqrt{q_y^{\,2} + q_z^{\,2}}$. The scattering vectors in-plane and out-of-plane are denoted with q_y and q_z, correspondingly. G denotes

the Guinier prefactor and R_g the radius of gyration. The parameters C_{por} and P_{por}, determine the power-law contribution of the surface roughness and large inhomogeneities. In this simplified approach the influence of refraction and correction terms of the DWBA-theory[99] have been neglected as only the structural progression was the main focus of the study.

The quality of the fit can be observed in Figure 30 in which the data are shown together with the fit. In the insert the evolution of the fit parameters with temperature is given. Interestingly, there is only an increase of the radius of gyration R_g from 1.7 to 2.1 nm. This behavior has been confirmed with Laboratory SAXS experiment, in which the sample has been casted on a capillary and has been measured in transmission geometry. In this experiment the radius of gyration has been determined with 2.0 nm, which is close to the value of the GISAXS experiment taking the different geometries and coating conditions into account. This demonstrates, that the structural morphology of the TAA and TAA-complexes is similar to the final CTZS powder. The determined Guinier prefactor G over temperatures quantifies the qualitative behavior, as expected from WAXS and in- and out-of-plane GISAXS, and manifests the increase of the electron density contrast and particle numbers caused by the CZTS formation.

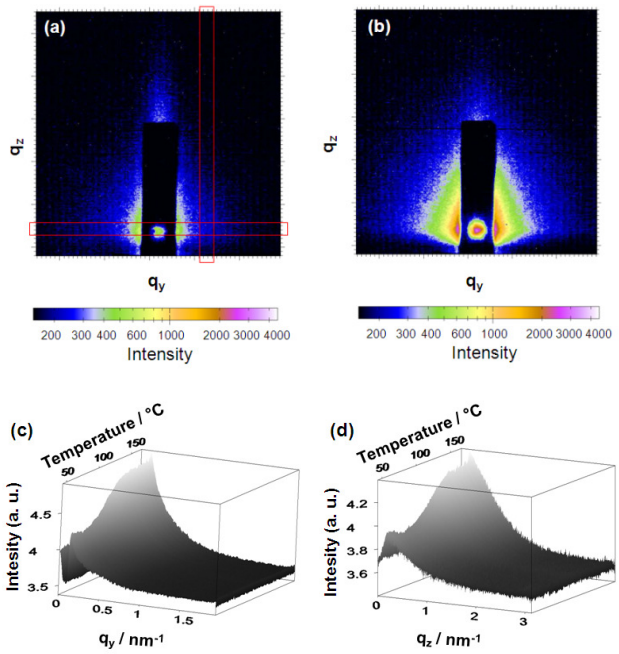

Figure 29: GISAXS patterns of the prepared samples at room temperature (a) and at 165 °C (b). The red squares indicate the vertical and horizontal areas for integration (in-plane and out-of-plane scattering). Evolution of the in-plane scattering (c) and the out-of-plane scattering (d) as a function of temperature.

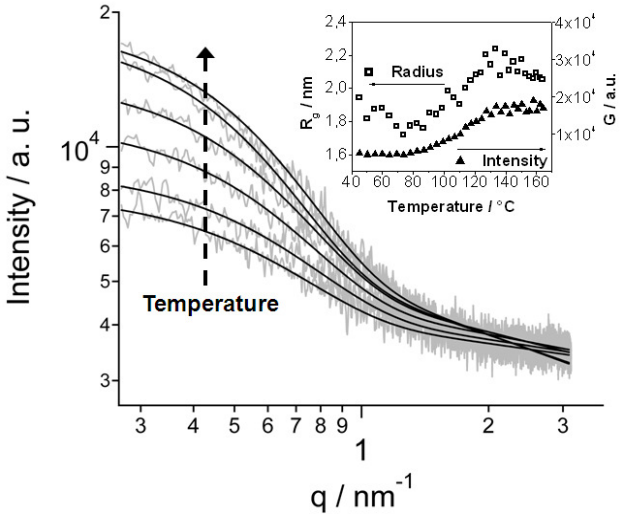

Figure 30: SAXS patterns at different temperatures (44, 83, 100, 114, 140, 164 °C) for a sample with 5 equiv. TAA (vertical integration) and the corresponding fits. Inset shows the evolution of the Guinier prefactor G and radius of gyration R_g during the heating run.

Assuming that the scattering structures are mainly caused by the crystalline phase, and in particular the smallest values of scattering objects are therefore the primary crystallites, the radius of gyration of 2.1 nm should be related to the crystal dimensions. Assuming spherical CZTS crystallites the diameter can be calculated using the equation $d = 2 \cdot \sqrt{5/3} \cdot R_g$. The obtained diameter of 5.4 nm is in fairly good agreement to the diameter calculated from XRD-measurements (8 nm) taking into account that the Scherrer equation can only be seen as an estimation. In addition, GISAXS values also display a slight uncertainty due to the high surface roughness and inhomogeneity of the CZTS films and the high polydispersity of the CZTS crystallites. Summing up the GIWAXS and GISAXS results, we conclude that TAA and TAA-complexes already decompose at approx. 80 °C and that the formation of CZTS starts at rather low temperatures of 105 °C.

Optical properties

The optical properties of the synthesized CZTS films were studied by transmittance and reflectance measurements. The absorption coefficient (α) was calculated according following equation:[102,103]

$$\alpha = \frac{1}{d}\ln\left(\frac{1-R}{T}\right) \qquad (8)$$

where d is the thickness of the film, R the reflectance and T the transmittance of the film. The film thickness was determined using a surface profiler (Table 7).

Figure 31 shows the absorption coefficient versus wavelength for the CZTS films synthesized at different temperatures with 5 equiv. TAA and 3.5 equiv. TAA.

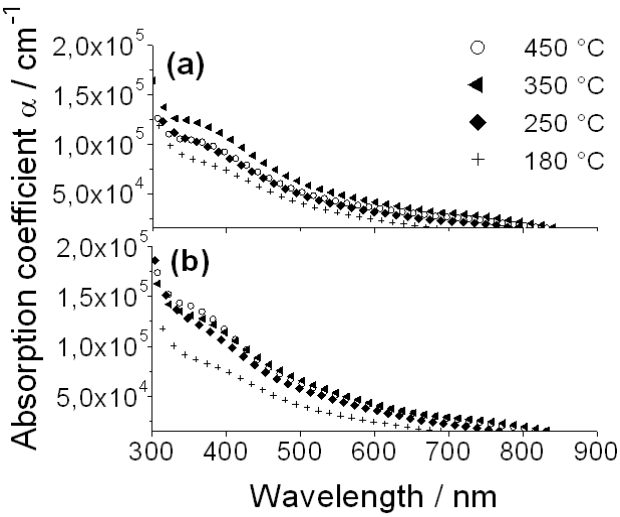

Figure 31: Optical absorption coefficient of CZTS films synthesized at different temperatures with 5 equiv. TAA (a) and 3.5 equiv. TAA (b).

All films show a high optical absorption coefficient lager than 10^4 cm^{-1}, which is in good agreement with other reports[112,127] in the literature. In addition the optical band gap (E_g) values can be obtained from the equation:

$$\alpha = \frac{A(h\upsilon - E_g)^n}{h\upsilon} \qquad (9)$$

where A is a constant, (hν) the photon energy and n an exponent, which is equal to 2 or ½ for indirect or direct transition, respectively. In the present work n was found to be ½ indicating a direct band gap, which is consistent with the literature.[112] Therefore, the band gap values were estimated from the $(\alpha h\nu)^2$ versus (hν) plots by extrapolating the linear part of the function as shown in Figure 32.

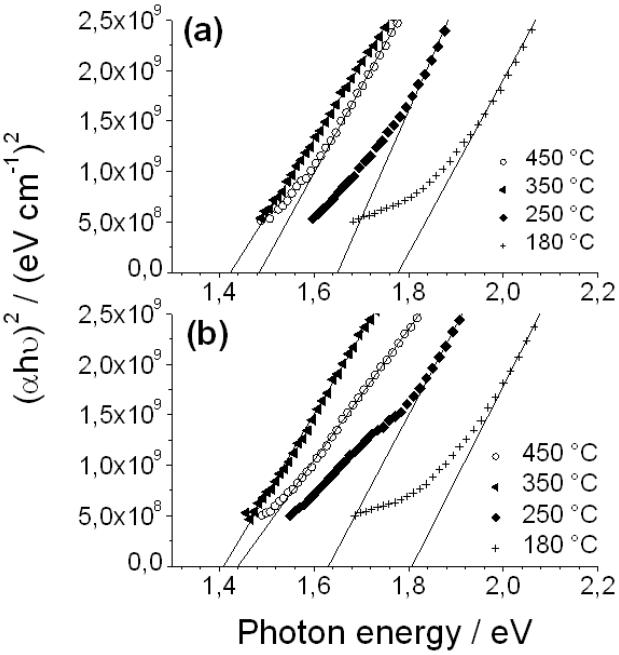

Figure 32: $(\alpha h\nu)^2$ vs. photon energy ($h\nu$) of CZTS films synthesized at different temperatures with 5 equiv. TAA (a) and 3.5 equiv. TAA (b).

The obtained band gaps range from 1.41 to 1.49 eV for CZTS films synthesized at 350 °C and 450 °C, which is consistent with reported values from literature (1.45 – 1.51 eV).[120,143] Especially samples prepared at 180 °C exhibit a significant blue shift of E_g (1.8 eV). On the one hand, this shift could be caused by quantum confinement effects as the primary crystallite size is substantially smaller at 180 °C (8 nm) than at higher temperatures (28-156 nm) and comparable critical dimensions for quantum confinement effects are reported for similar semiconductors like $CuInS_2$[144] or CdS.[11] On the other hand, it is more likely that the optical absorption is influenced by the high lattice disorder, the difference in compositional order and/or found impurities at this temperature.

Chemical composition

The elemental composition was determined using TEM-EDX analysis. Figure 33 shows the atomic percentage of the elements for CZTS samples synthesized with 5 equiv. and 3.5 equiv. TAA, respectively, at different temperatures. The atom percentages were calculated using the Cu K, Zn K, Sn L, and S K peaks using the Cliff-Lorimer approximation.[101] The elemental ratios of Cu/(Zn+Sn), Zn/Sn and S/(Cu+Zn+Sn) are summarized in Table 6.

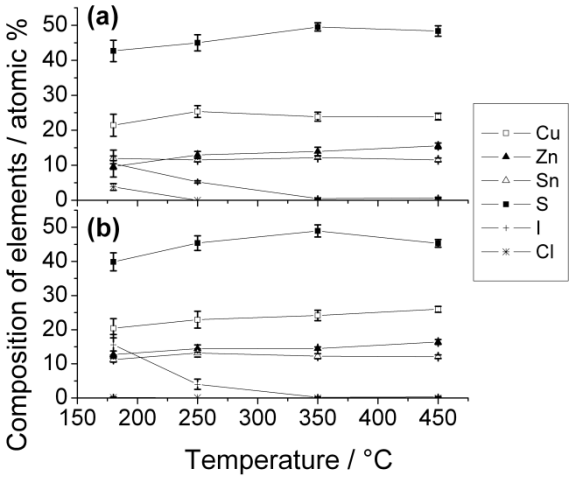

Figure 33: Chemical composition of CZTS films synthesized with 5 equiv. TAA (a) and 3.5 equiv. TAA (b).

Table 6. Elemental ratios of the CZTS powders synthesized at different temperatures calculated from TEM-EDX measurements.

T / °C	Elemental ratio					
	5 equiv. TAA			3.5 equiv. TAA		
	Cu/(Zn+Sn)	Zn/Sn	S/(Cu+Zn+Sn)	Cu/(Zn+Sn)	Zn/Sn	S/(Cu+Zn+Sn)
180	0.86 ± 0.16	1.13 ± 0.13	0.90 ± 0.07	1.00 ± 0.18	0.81 ± 0.08	0.99 ± 0.07
250	0.84 ± 0.14	1.10 ± 0.09	0.90 ± 0.06	1.04 ± 0.08	1.12 ± 0.10	0.91 ± 0.09
350	0.91 ± 0.06	1.19 ± 0.09	0.96 ± 0.07	0.92 ± 0.07	1.15 ± 0.14	0.99 ± 0.04
450	0.91 ± 0.03	1.36 ± 0.13	0.83 ± 0.04	0.89 ± 0.06	1.35 ± 0.07	0.95 ± 0.06

All CZTS powders possess nearly stoichiometric amounts of sulfur, with an S/(Cu+Zn+Sn) ratio varying between 0.99 and 0.83, independent from the amount of TAA in the precursor solution. Despite the fact that the precursor solution contains stoichiometric amounts of Cu, Zn and Sn, nearly all samples show Cu/(Zn+Sn) ratios below 1 and Zn/Sn ratios above 1.

These deviations from the stoichiometric composition might be caused by a preferred generation of volatile Cu-species, compared to Zn and Sn, during the thermal induced CZTS formation. Consequently, the powders are of Cu-poor and Zn-rich nature, which is the preferable elemental composition to obtain highly efficient CZTS-based thin film solar cells, according to investigations by Katagiri et al.[145] No significant influence of different synthesizing temperatures on the elemental ratios can be observed, except a slight increase of the Zn/Sn ratio when samples are heated up to 450 °C rather than 350 °C. In CZTS samples, synthesized at temperatures at and below 250 °C, the elements iodine and chlorine were also detected by TEM-EDX analysis, which may derive from not yet removed decomposition products of the metal-precursor at these stages.

Microstructure

Figure 34 shows SEM images of the CZTS films synthesized with 5 equiv. and 3.5 equiv. TAA, obtained at 180 °C and 450 °C.

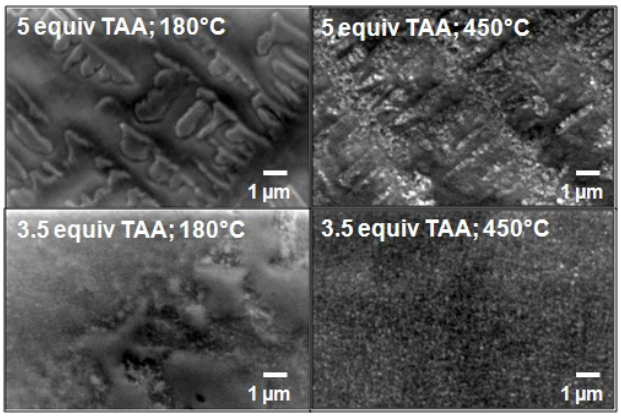

Figure 34: SEM micrographs of CZTS films synthesized with 5 equiv. and 3.5 equiv. TAA at 180 °C and 450 °C.

Films synthesized at 180 °C show a continuous and “closed” surface, contrary to films treated with 450 °C, which exhibit a porous-like surface. CZTS films synthesized with 5 equiv TAA exhibit a microstructured surface with higher roughness, in contrast to films prepared with 3.5 equiv. TAA. Table 7 gives the root-mean-square (Rq) values of roughness based on surface profiler measurements of the films, which are consistent with the observations from the SEM micrographs showing an enhanced surface roughness for the CZTS samples prepared with 5 equiv. TAA. The height of these structures are in the range of 20 to 100 nm

(estimated from surface profiler measurements), however, the film itself seems to be continuous. This surface roughness and microstructure might be caused by a pronounced crystallization of excess TAA within the precursor films compared to samples with only 3.5 equiv. TAA. This assumption is also supported by the observation, that precursor films with 5 equiv. TAA turn from transparent to white with a crystalline like surface, after coating. This is in contrast to precursor films with 3.5 equiv. TAA, which stay transparent over a long time. However, only single phase CZTS is detected by XRD-measurements in both cases at 450 °C. The film thickness decreases slightly from 164 nm and 152 nm to 129 nm and 116 nm, respectively, with increasing temperature, indicating that a more condensed CZTS layer is obtained at higher temperatures.

Table 7: Rq values of roughness and thickness of the CZTS films.

T / °C	Rq values / nm		Thickness / nm	
	5 equiv TAA	3.5 equiv TAA	5 equiv TAA	3.5 equiv TAA
180	21.4	5.7	164	152
250	28.4	2.0	143	139
350	29.9	4.4	127	136
450	28.4	5.6	129	116

2.3.4 Conclusion

Highly crystalline CZTS thin films are prepared by a solution based precursor method using copper(I) iodide, zinc(II) acetate, tin(II) chloride as metal precursors and TAA as sulfur source. The use of TAA turns out to be advantageous, as the release of sulfur species, hence, the formation of sulfides already starts at 105 °C. At low synthesizing temperatures the coexistence of other phases (ZnS, Cu_2SnS_3) beside CZTS cannot be excluded due to structural similarities, however, samples synthesized at higher temperatures (350 °C and 450 °C) show also the minor reflections, characteristic for single phase CZTS with kesterite structure. All films exhibit high optical absorption coefficients (>10^4 cm^{-1}) and optical band gaps between

1.41 and 1.81 eV depending on the synthesizing temperature. Obtained CZTS powders exhibit a Cu-poor and Zn-rich nature, which was found to be an ideal composition ratio for CZTS-based thin film solar cells. Samples prepared with only 3.5 equiv. of TAA exhibit a surface with low roughness, whereas, the use of 5 equiv. TAA leads to microstructured films with high surface roughness. However, both synthesis routes lead to single phase CZTS with suitable properties for photovoltaic applications.

2.3.5 Inorganic solar cells using Cu_2ZnSnS_4 as absorber layer

CZTS thin films synthesized from metal salts and TAA (see 2.3) show very beneficial properties for the application as absorber layers in solar cells. They exhibit a band gap of approximately 1.4 eV and a high absorption coefficient (> 10^4 cm^{-1}). In addition, single phase CZTS with an ideal chemical composition (Cu/(Zn+Sn) and Zn/Sn ratios) for the fabrication of efficient solar cell devices[145] is obtained.

To investigate the performance of these CZTS thin layers in devices, inorganic solar cells with an ITO/CZTS/CdS/Al assembly (Figure 35) were fabricated and characterized.

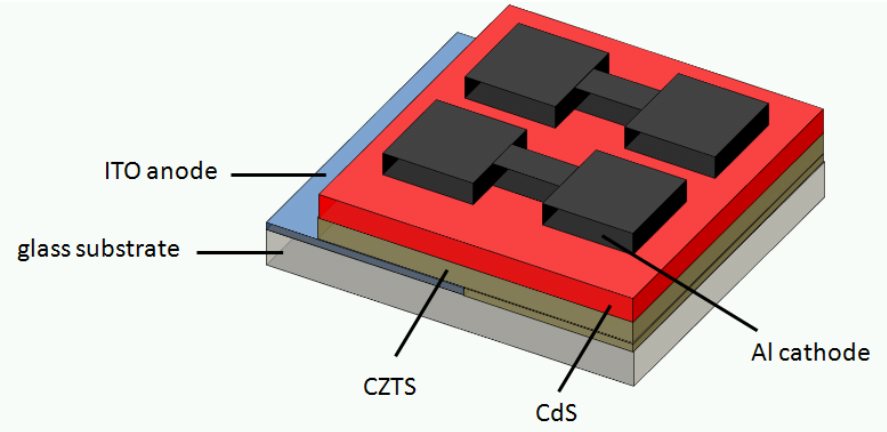

Figure 35: Schematic illustration of an ITO/CZTS/CdS/Al assembly to investigate the performance of CZTS thin layers in solar cell devices.

As CZTS shows p-type conductivity, a n-type buffer layer (CdS) is used to obtain an efficient p,n-junction for the separation of generated electron hole pairs.[125146] Caused by the internal electric field, the holes (positive charges) travel to the ITO anode and the electrons (negative charges) migrate to the aluminum cathode.

As the buffer layer influences the performance of the solar cell significantly, two different chemical bath deposition based preparation methods were investigated for CdS.

2.3.5.1 CZTS/CdS

CZTS thin films were prepared from stoichiometric precursor solutions with 7 equiv. TAA as described in 2.3.3. The CZTS precursor layers were spin coated at 1500 rpm for 18 seconds on ITO covered glass substrates and baked at 350 °C for 15 minutes (21 °Cmin^{-1} heating rate) under vacuum to form the final CZTS thin film. The composition of the two different CdS precursor solutions is given in Table 8. These solutions were directly applied on top of the CZTS layer by spin coating (1000 rpm, 18 sec) and the substrate was heat treated at 250 °C for 10 minutes under vacuum. In the next step the same CdS precursor solution was applied again on the substrates using the same preparation conditions, except the time of the heat treatment was reduced to 5 minutes. To obtain a working solar cell device, a 200 nm thick aluminum cathode was deposited on top of the CdS layer in the last step.

Table 8: Composition of the two different CdS precursor solutions used for the preparation of CdS buffer layers.

Precursor solution 1				Precursor solution 2			
	mass / mg	volume / mL	equiv.		mass / mg	volume / mL	equiv.
$CdCl_2$	36.7	-	1	$CdAc_2$	75.7	-	1
TU	45.6	-	3	TU	75.0	-	3
1-butylamine	-	2	-	pyridine	-	2	-
1-propionic acid	-	0.2	-				

Precursor solution 1 and 2 are modified recipes from literature reports.[47,147] In both cases TU is used as sulfur source to provide the necessary sulfur species for the formation of CdS.
At this stage it has to be noted, that the preparation of CdS buffer layers using $CdAc_2$ and TAA as precursor solution was investigated as well, however, the obtained solar cells were all short-circuited. Therefore, this preparation method is not described in detail further.

2.3.5.1.1 CdS buffer layer prepared from $CdCl_2$ and TU

During the preparation of the solar cells, UV/vis spectra of the different preparation steps were recorded to investigate the formation of the CdS buffer layers. Figure 36 shows the

UV/vis spectra from a substrate containing only the CZTS absorber layer (CZTS) and of the same substrate after the first and second application of the CdS buffer layer (CZTS + CdS and CZTS + CdS + CdS, respectively). It can be clearly seen, that the absorption below 500 nm increases significantly after the first and second application of the CdS buffer layer on top of the CZTS layer. This is reasonable, as CdS exhibits an optical band gap of 2.5 eV,[12,148] which corresponds to an absorption onset of approximately 506 nm.

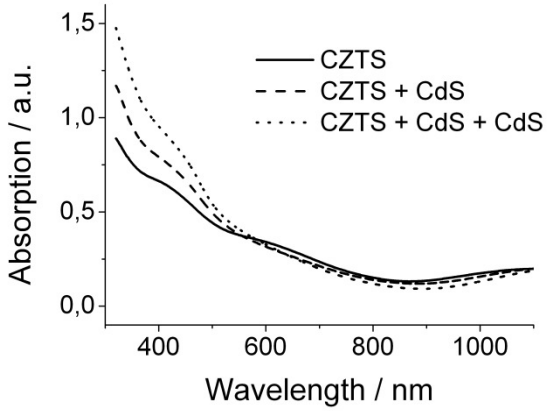

Figure 36: UV/vis spectra of an ITO/CZTS (CZTS) and of an ITO/CZTS/CdS sample after the first (CZTS + CdS) and second (CZTS + CdS + CdS) CdS buffer layer formation.

The I-V characteristic of a CZTS thin film solar cell using this type of CdS buffer layer is shown in Figure 37. Despite the fact, that highly efficient CZTS thin film solar cells nowadays reach efficiencies of up to 10 %,[107] the obtained efficiency is quite remarkable. In this case the CZTS thin layer, which produces the charge carriers, is only approx. 120 nm thick[29] compared to other high performance devices, which use CZTS layers with a thickness of several µm. In addition, it can be expected, that with more sophisticated assemblies using molybdenum anodes and various interfacial layers, like ZnO, much higher efficiencies could be achieved. Therefore, the obtained efficiency of 0.6 % shows clearly the high potential of the CZTS prepared by the synthesis strategy described in 2.3.3.

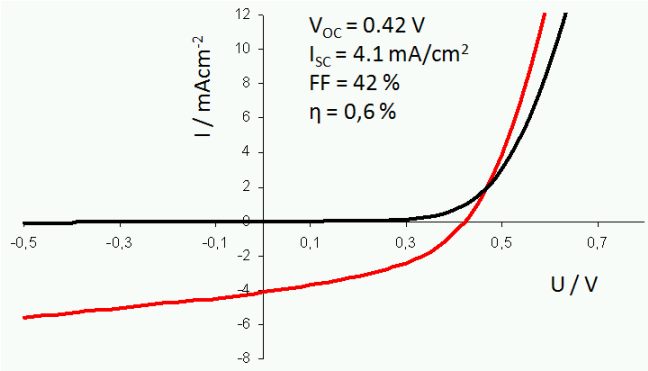

Figure 37: I-V characteristic of a CZTS thin film solar cell using a CdS buffer layer prepared with $CdCl_2$ and TU.

2.3.5.1.2 CdS buffer layer prepared from $CdAc_2$ and TU

After the application of the CdS buffer layer on top of the CZTS thin layer a strong increase in absorption below 500 nm can be observed from UV/vis spectra (Figure 38). An explanation for this phenomenon is given in 2.3.5.1.1.

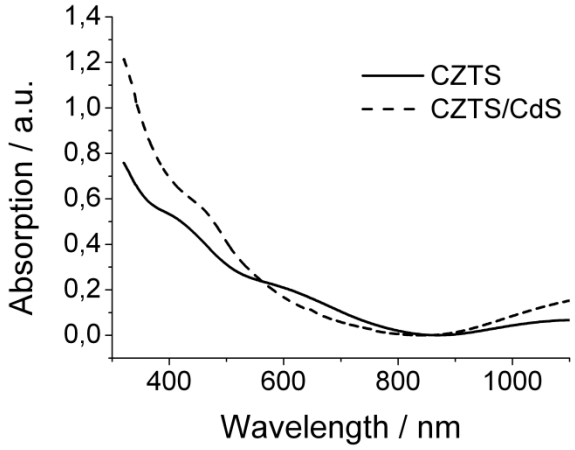

Figure 38: UV/vis spectra of an ITO/CZTS (CZTS) and of an ITO/CZTS/CdS sample after the second CdS buffer layer formation (CZTS /CdS).

To obtain structural and morphological information about the different thin films (CZTS and CdS) during the preparation of the solar cell, scanning electron microscopy studies were conducted. Top and cross-sectional images at various stages of the fabrication (CZTS layer,

CZTS/CdS layer) are shown in Figure 39. Figure 39 a and Figure 39 b show the top view of the CZTS layer and CZTS/CdS layer, respectively, after the thermal treatment. The CZTS layer consists of agglomerated nanoparticles forming a porous surface structure. Upon CdS deposition, the film displays a similar surface morphology, however, with larger agglomerates. The porosity of the layers is most likely caused by the evaporation of volatile side products, formed during the decomposition of the precursor materials, hence, the formation of the metal sulfide thin films. Figure 39 c and Figure 39 d display a cross-section of a final CZTS/CdS solar cell recorded with a SE-inlens and an angle selective backscattered electron (ASB®)-detector, respectively.

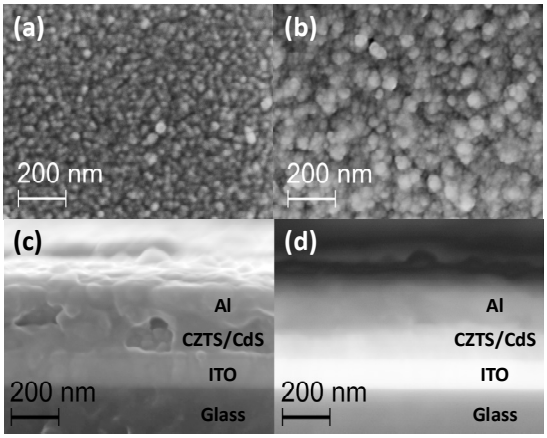

Figure 39: SEM images recorded during various stages of cell fabrication. (a) Top view of the CZTS film. (b) Top view of the CZTS/CdS layer. Cross-sectional view of the final CZTS/CdS solar cell recorded with a SE-inlens (SE) detector (c) and an angle selective backscattered electron (ASB®)-detector (d).

The ASB®-detector allows distinguishing between the ITO, CZTS/CdS and aluminum layer. Due to similar Z-values and similar morphologies for CZTS and CdS it is not possible to distinguish between these two layers neither in the ASB®- nor the SE-image. Therefore, only the thickness of the combined layers of CZTS and CdS can be estimated at approximately 120 – 130 nm.

The I-V characteristic of such a solar cell is shown in Figure 40 (right). The device exhibits characteristics as follows: V_{OC} = 420 mV, J_{SC} = 3.02 mA/cm^2 and FF = 39.0 % leading to an efficiency of 0.5% under illumination of 100 mW/cm^2. The external quantum efficiency (EQE) spectrum of the solar cell is shown in Figure 40 (left). The EQE increases towards shorter wavelengths upon approx. 500 nm, which is in agreement with the absorption spectra of the CZTS thin film. The decrease of EQE below 500 nm can be assigned to a pronounced

absorption of the CdS buffer layer. It has to be noted that no additional optimization steps (variation of the CZTS composition, increase of the CZTS layer thickness, other architectures using Mo and ZnO as electrodes and/or interfacial layers) were undertaken. As a result, it can be expected, that much higher power conversion efficiencies are obtainable using the presented solution based precursor method.

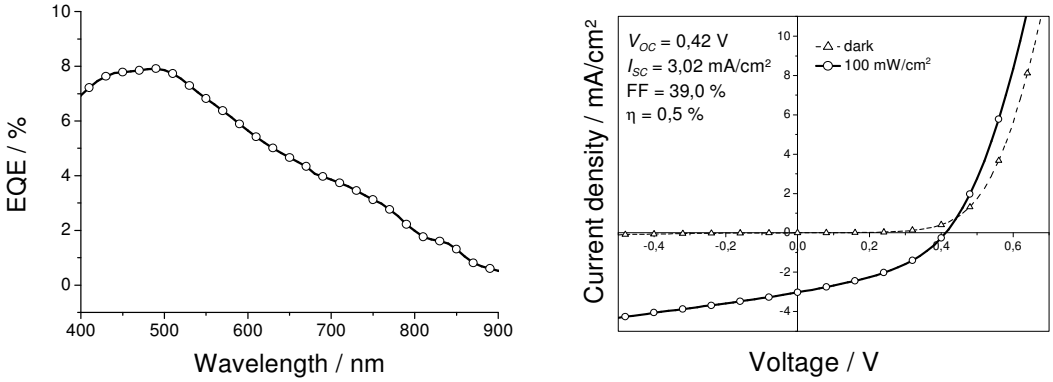

Figure 40: EQE spectra (left) and I-V characteristic (right) of an ITO/CZTS/CdS/Al solar cell.

2.4 Hybrid solar cells

2.4.1 $CuInS_2$/PCBM

In 2.2 the formation of CIS, starting from metal salts (CuAc and $InCl_3$) and TU as sulfur source and pyridine as solvent was studied in detail. The main focus of the work was placed on the investigation of structural and chemical changes within the precursor layer during the heat treatment. It was observed, that it is necessary to add TU in a certain excess to the stoichiometric required amount to ensure a complete coordination of the metal salts with TU molecules and to allow a uniform formation of metal salt/TU/pyridine complexes throughout the layer. These complexes decompose to CIS at 130 °C, which is much lower than the decomposition temperature of pure TU (190 °C). However, too high concentrations of TU lead to drastic morphological changes during the thermal treatment of the precursor layer. At 190 °C non-coordinated TU decomposes very quickly, leading to a collapse of the precursor layer, which consisted of CIS particles imbedded in a matrix of TU before this change.

To assess the impact of these chemical and morphological changes on the solar cell performance of CIS thin layers, bilayer solar cells with an ITO/CIS/PCBM/Al assembly were fabricated. As the prepared CIS thin layers exhibit a Cu/In ratio slightly higher than 1, it can be assumed, that these films show p-type conductivity.[44] As a result, the second layer has to have n-type conductivity to enable an efficient separation of excitons. To reduce the number of parameters, which can additionally affect the performance of the cell, and to be able to study the influence of different synthesizing temperatures of the CIS layer, the organic n-type semiconductors PCBM was chosen. This type of semiconductor can be applied directly on top of the CIS layer from solution and does not need a successive thermal treatment. Therefore, the CIS thin layer is not influenced by its application and mainly the different heat treatments of the CIS layer influence the performance of the cell.

The preparation of the solar cell devices was conducted as follows: The CIS precursor solution (CuAc (0.22 mol/L), $InCl_3$ (0.15 mol/L) and TU (1.5 mol/L) dissolved in pyridine) was spin coated at 1500 rpm on ITO covered glass substrates, which were then baked for 15 min at different temperatures (160, 220, 350 and 450 °C) under vacuum. The heating rate was kept at approximately 23 °C/min. After the heat treatment, the substrates were cooled down to room temperature under vacuum, before the PCBM solution (20 mg/mL in $CHCl_3$) was spin coated with 2000 rpm on top of the CIS layer. In the last step Al electrodes were evaporated through shadow masks on top of the PCBM layer to obtain the final ITO/CIS/PCBM/Al solar cell assembly.

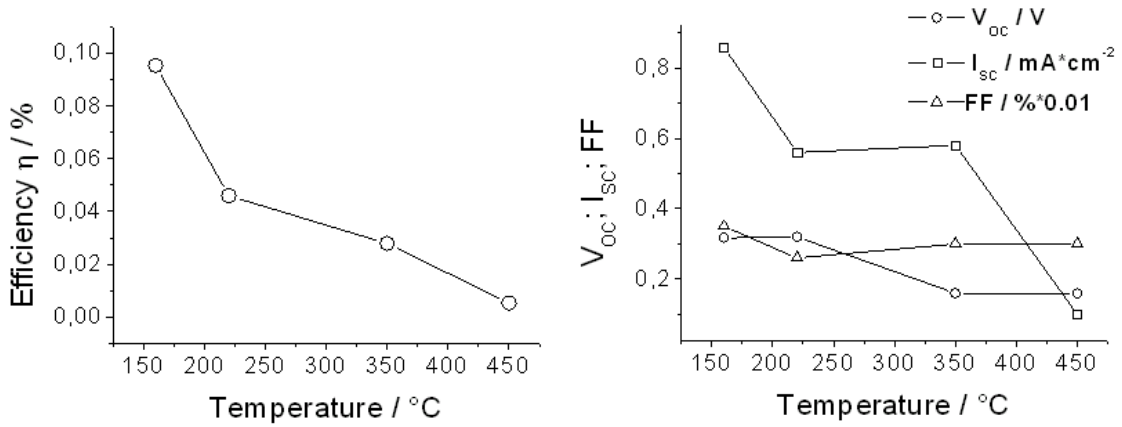

Figure 41: Solar cell parameters as a function of the synthesizing temperature of the CIS absorber thin film.

Interestingly, solar cells, where the CIS layer was baked at 160 °C, hence, still contains TU, shows the highest efficiencies. At higher synthesizing temperatures (≤ 220 °C) the V_{OC} and I_{SC} of the solar cells drops significantly, which might be caused by the morphological changes occurring at 190 °C. Before the decomposition of non-coordinated TU the CIS layer is continuous and spaces between the CIS nanoparticles are filled with TU, inhibiting direct contacts between the anode and cathode (ITO and Al, respectively). After the decomposition of the TU matrix these free spaces between the CIS nanoparticles are not filled anymore, leading to a higher amount of short circuits within the active layer of the solar cell and as a result to a reduced solar cell performance.

The I-V characteristic of the solar cell with the highest efficiency (η = 0.1 %) using an ITO/CIS/PCBM/Al assembly is shown in Figure 42. In this case the CIS layer was baked at 160 °C for 15 minutes. The curve shows a pronounced S-shape, which could derive from bad charge transport properties of the active layer, due to the remaining TU.

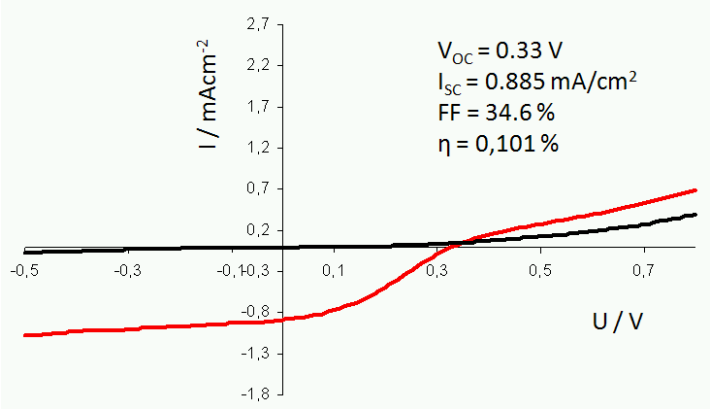

Figure 42: I-V characteristic of a solar cell using an ITO/CIS/PCBM/Al assembly. The CIS layer was baked at 160 °C.

2.4.2 Cu_2ZnSnS_4/Polymer

Motivated by the good results obtained during the characterization of CZTS (2.3.3) and the use of these CZTS thin layers in inorganic solar (2.3.5), hybrid solar cells based on an ITO/Cu_2ZnSnS_4:P3EBT/Al assembly were fabricated. In this case a precursor solution, which contained the CZTS precursors (CuAc, $ZnAc_2$, $SnCl_2$ and TAA) and poly(3-(ethyl-4-butanoate)thiophene (P3EBT), a photoactive polymer, was applied directly on an ITO covered glass substrate. During the thermal treatment the CZTS nanoparticles are formed directly within the polymer matrix. Unfortunately, these cells did not show any noteworthy

photovoltaic effect, which can be explained by a conductivity mismatch of the CZTS and used polymer, rather than the CZTS material itself. Based on literature reports[149] and on own observations (2.3.5) CZTS shows p-type conductivity, hence, it would require a n-type photoactive polymer. Due to the restriction to highly polar solvents (e. g. pyridine) to obtain a stable CZTS precursor solution, the only possible photoactive polymer for the preparation of the precursor solution was P3EBT, which is moderately soluble in pyridine. However, this polymer is a polythiophene derivative and shows p-type conductivity. Variations of the Cu/(Zn+Sn) and Zn/Sn ratio within the precursor solution, to alter the conductivity behavior of CZTS, did not improve the situation either.

To verify this assumption, bilayer solar cells using an ITO/CZTS/PCBM/Al assembly were fabricated. As PCBM shows n-type conductivity this solar cell architecture should show a photovoltaic effect, assuming that CZTS exhibits p-type conductivity. As expected, these solar cells showed an increase in the I_{SC} of three orders of magnitude compared to the CZTS/P3EBT nanocomposite solar cells, leading to an efficiency of approximately 0.04 %. At this stage it has to be noted, that no further optimizations of these cells were undertaken, therefore, even higher efficiencies could be expected.

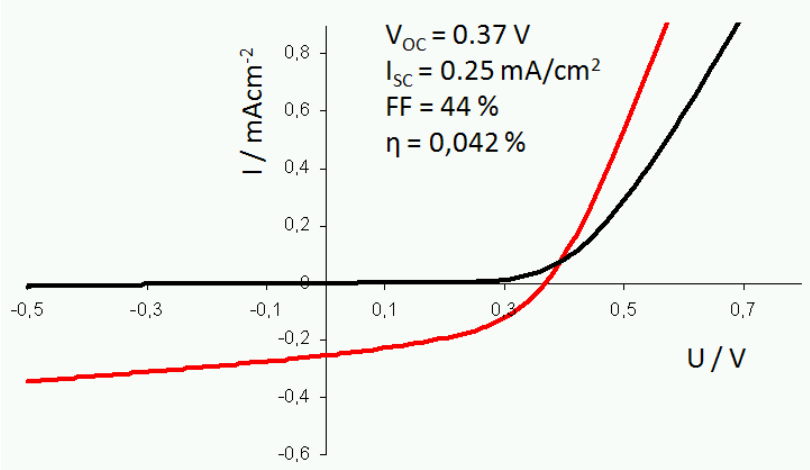

Figure 43: I-V characteristic of a solar cell using an ITO/CZTS/PCBM/Al assembly.

3 Metal sulfides prepared via metal xanthates

3.1 Introduction

Most synthetic routes for the preparation of metal sulfide nanoparticles and metal sulfide thin films rely on the use of metal salts (e.g. CuCl, CuAc, $ZnCl_2$, $CdCl_2$, $InCl_3$) in combination with an molecular sulfur source (e.g. TU, TAA).[29,86,147] Due to their chemical nature, only very polar solvents are suitable to obtain homogeneous solutions of these precursors. Concerning the straight synthesis of nanoparticles or thin films, this situation does not raise problems. However, for the direct fabrication of hybrid materials (e.g. polymer/inorganic blends) this situation is unsatisfactory. The preparation of a homogeneous solution containing the metal sulfide precursors and the organic polymer turns out to be very difficult, due to the contrary solubility of the components. In contrast to the metal sulfide precursor, organic polymers (e.g. P3HT, MEH-PPV, F8T2)[150,151] require apolar solvents, like $CHCl_3$, chlorobenzene or dichlorobenzene, to obtain concentrated solutions. Especially for the preparation of hybrid solar cells using the fabrication approach presented in 2.4.2 these circumstances reduce the choice of suitable organic polymers for the preparation of the active layer. This drastically limits the theoretical potential of the obtained solar cells.[47]

The only way to improve this situation is to change the solubility properties of the organic polymer or the metal salts precursors. Concerning photoactive organic polymers the minority of literature reports deals with the synthesis of polymers, which are soluble in highly polar solvents and suitable for photovoltaic applications at the same time. This is understandable, as the most efficient solar cells are based on the bulk heterojunction architecture, using organic electron acceptors (e.g. PCBM)[51], which are highly soluble in apolar solvents. As a result, no driving force for the development of new photoactive polymers for apolar solvents exists. In addition, the synthesis of polymers is very time consuming.

Caused by this situation, the focus was placed on the development of metal sulfide precursors, which are highly soluble in apolar solvents to be able to prepare precursor solutions using the broad range of commercially available photoactive polymers. O'Brien et al.[152-156] and Efrima et al.[157,158] were among the first, who showed that it is possible to use

metal dithiocarbonate (also called xanthate), dithiocarbamate and trithiocarbonate metal salts (Figure 44) for the synthesis of metal sulfide nanoparticles.

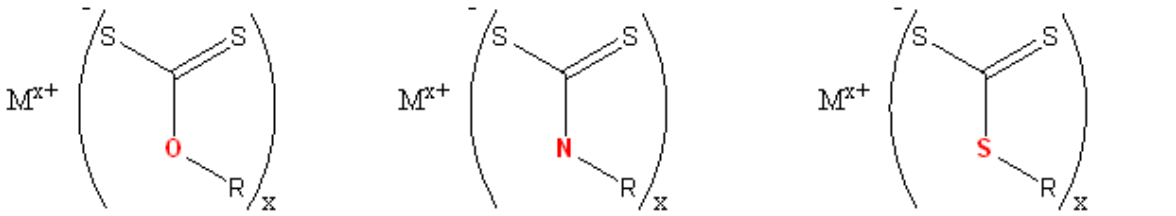

Dithiocarbonate metal salt (Xanthate metal salt) Dithiocarbamate metal salt Trithiocarbonate metal salt

Figure 44: Chemical structure of dithiocarbonate (xanthate), dithiocarbamate and trithiocarbonate metal salts.

These three organic-metal single source precursors are strongly related as their chemical structure is only altered by one position, however, their decomposition behavior differs significantly. Despite the fact that all three precursors can form metal sulfides, the decomposition temperature of dithiocarbamates (approx. 200 °C) and trithiocarbionates is significantly higher than of xanthates (approx. 140 °C). In addition, it was found, that metal sulfide nanoparticles synthesized from xanthates show a much higher quality as from the other two precursors.[157] As the chemical modification (e.g. breakage of conjugation) and/or decomposition of photoactive polymers starts in most cases at temperatures above 200 °C, it is important to keep the synthesizing temperature for the metal sulfide nanoparticles as low as possible. As a result, the main focus was placed on the application of xanthate metal salts as precursor materials.

The solubility of xanthates can be modified by changing the alkyl moiety (R-group in Figure 44). Whereas commercially available ethyl and amyl metal xanthates show hardly any solubility in organic solvents, metal xanthates with branched alkyl moieties are reasonable soluble. Transition metal xanthates with different alkyl moieties can be prepared by a simple two step synthesis (Figure 45). Firstly, the potassium xanthate with the desired alkyl moiety is synthesized starting from a potassium base (e.g. *t*-BuOK), CS_2 and the selected alcohol. In a second step the potassium xanthate is reacted with the corresponding metal salt (e.g $InCl_3$, $CdCl_2$, $CuAc_2$) to form the final transition metal xanthate.

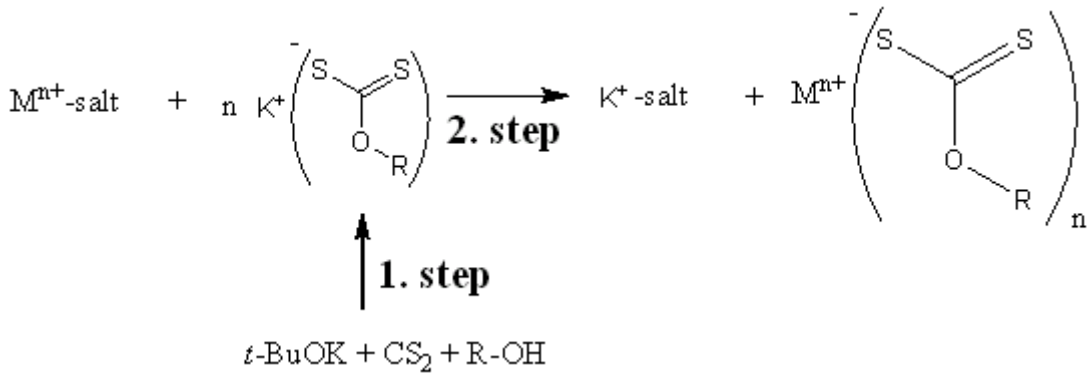

Figure 45: 2-step synthetic approach towards metal xanthates.

Furthermore metal xanthates are air stable and non hazardous, which allows handling of the precursors under ambient condition without any health related precautions.

The main decomposition pathway of metal xanthates is related to the Chugaev reaction,[159] yielding an olefin, COS and the metal sulfide. The exemplary decomposition reaction of Cu xanthate is depicted in Figure 46.

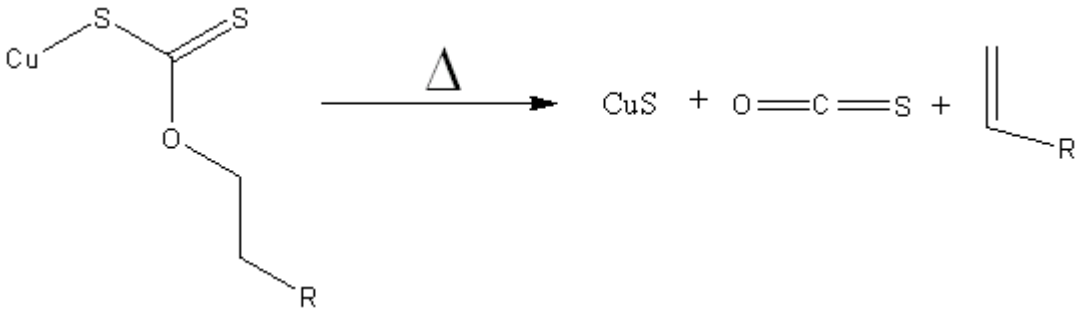

Figure 46: Decomposition pathway of Cu xanthate following a Chugaev related reaction.

It was shown, that the decomposition temperature of metal xanthates can be lowered drastically when coordinating solvents (e.g. alkylamine solvents) or Lewis bases[157] are used. If the alkyl moiety of the metal xanthate is small enough, the formed olefin is volatile under the decomposition conditions and highly pure metal sulfides can be obtained.

3.2 Syntheses of metal xanthates

3.2.1 Experimental

3.2.1.1 Materials

A list of the used chemicals and solvents, including their purity grade can be found in Table 9. All chemicals and solvents were purchased from Sigma Aldrich and used without any further purification.

Table 9: Chemicals and solvents and their corresponding purity grade.

Chemical/Solvent	**Purity grade**
acetone	puriss.
tetrahydrofuran (THF)	anhydrous ≥ 99.9 %
methanol (MeOH)	puriss.
diethyl ether (Et_2O)	puriss., stabilized
chloroform ($CHCl_3$)	puriss.
n-pentane	98 %
potassium ethyl xanthate	96 %
potassium amyl xanthate	96 %
carbon disulfide (CS_2)	≥ 99.9 %
1-decanol	99 %
2,4-dimethyl-3-pentanol	99 %
3,3-dimethyl-2-butanol	98 %
2,2-dimethyl-3-pentanol	97 %
4,4-dimethyl-2-pentanol	98 %
1-tert-Butoxy-2-propanol	99 %
1-phenyl-1-propanol	≥ 97 %
potassium-*tert*-butoxide (*t*-BuOK)	purum, ≥ 97 %
copper (II) chloride dihydrate ($CuCl_2{}^*2H_2O$)	99.99+ % metal basis
zinc (II) chloride ($ZnCl_2$)	puriss. p.a.
indium (III) chloride ($InCl_3$)	98 %
tin (IV) chloride pentahydrate ($SnCl_4{}^*5H_2O$)	lumps, 98 %

3.2.1.2 Methods

NMR spectra were recorded on a Bruker Ultrashield 300. ^{1}H- and ^{13}C-NMR spectra were obtained in $(CD_3)_2CO$ and $CDCl_3$ solutions at 300 MHz for ^{1}H- and 75 MHz for ^{13}C-NMR spectra. Chemical shifts are reported in δ units, parts per million (ppm) relative to the multiplet of $(CD_3)_2CO$ at 2.050 ppm or relative to the singlet of $CDCl_3$ at 7.240 ppm for ^{1}H-NMR spectra. For ^{13}C-NMR spectra the chemical shifts are referenced relative to the multiplet of $(CD_3)_2CO$ at 29.920 ppm or relative to the triplet of $CDCl_3$ at 77.230 ppm. Elemental analyses were carried out on a Universal CHNS Elemental Analyzer Vario El III. Thermal gravimetric measurements were performed on a Netzsch Jupiter STA 449C with a Netzsch Aëolos QMS 403C quadrupole mass spectrometer for gas analysis. All measurements were carried out in helium atmosphere and at a heating rate of 10 °C/min. The decomposition temperature was determined at a mass loss of 5 %. The X-ray powder diffraction profiles were measured with a Siemens D-5005 powder diffractometer (θ/θ geometry, Cu Kα radiation, graphite monochromator, scintillation counter, step width 0.02 °, constant counting times of 20 s/step). Transmittance and reflectance spectra of the thin films were measured with a Lambda900 spectrometer (Perkin Elmer) including an external integrating sphere diffuse reflectance accessory (PELA-1000). Energy dispersive X-ray (EDX) spectra were recorded in scanning transmission electron microscopy (STEM) mode using a Philips CM20/STEM operated at 200 kV with a LaB_6 cathode equipped with a Noran HPGe-detector.

3.2.1.3 Overview and characterization of synthesized metal xanthates

Figure 47 gives an overview of the chemical structures of the synthesized metal xanthates. Depending on the valence state of the metal atom, the metal xanthates bear one, two, three or four xanthate units. In the case of tin (IV) xanthate two different xanthates were prepared. Tin (IV) tetraxanthate exhibits the typical xanthate structure, whereas tin(IV) thio dixanthate consists of two tin atoms, which are bridged via two sulfur atoms, bearing two xanthate units each. Figure 48 shows the different alkyl moieties of the xanthate units, which were investigated to enhance the solubility of the metal xanthates, and Table 10 gives an overview of the synthesized metal xanthates for Cu, Zn, In and Sn. Potassium ethyl and amyl xanthate had not to be prepared, as they are commercially available.

In this context Cu xanthate plays an important role, as it bears only one xanthate group, which leads to the fact that it shows the lowest solubility of all metal xanthates. As a result, Cu xanthate was always prepared first to investigate the influence of the alkyl moiety on the solubility. The corresponding Cu Hex and Hep xanthates showed the best solubility in organic solvents, as a result, the preparation of Zn-, In- and Sn xanthates was only targeted with these alkyl moieties. The synthesis of tin(IV) tetra Hep xanthate was attempted as well but did not yield a pure product. A detailed investigation of the synthesis of different metal Hep xanthates was recently made by Schenk.[160] The detailed characterization of the xanthates and their conversion into various metal sulfides, like CIS and CZTS, can be found in his work.

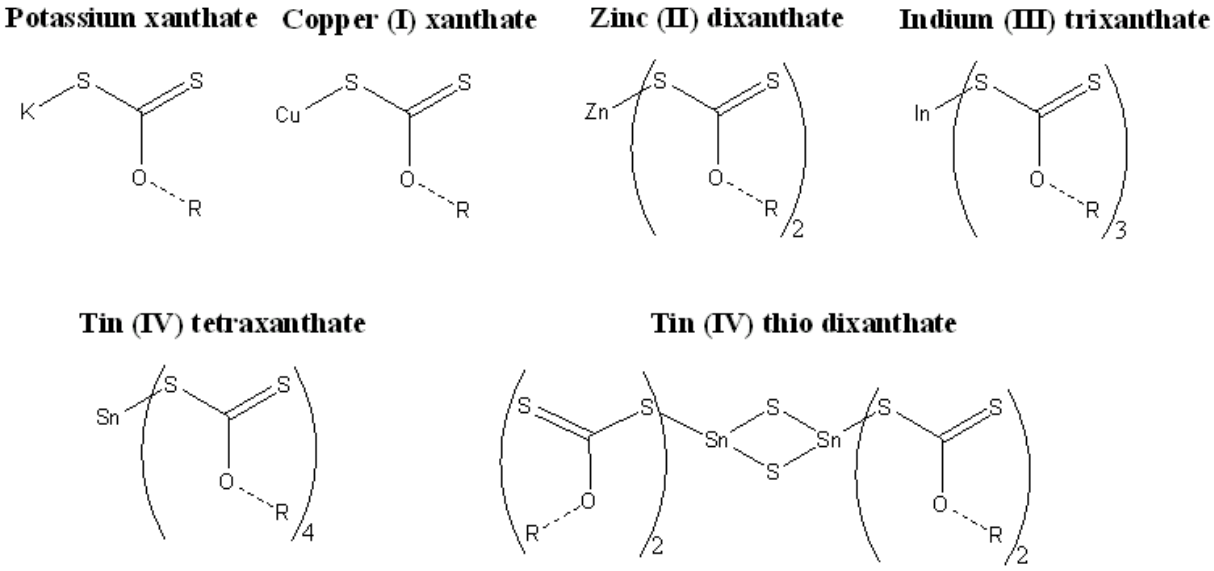

Figure 47: General chemical structure of the synthesized metal xanthates. “R” represents the alkyl moiety of the xanthates.

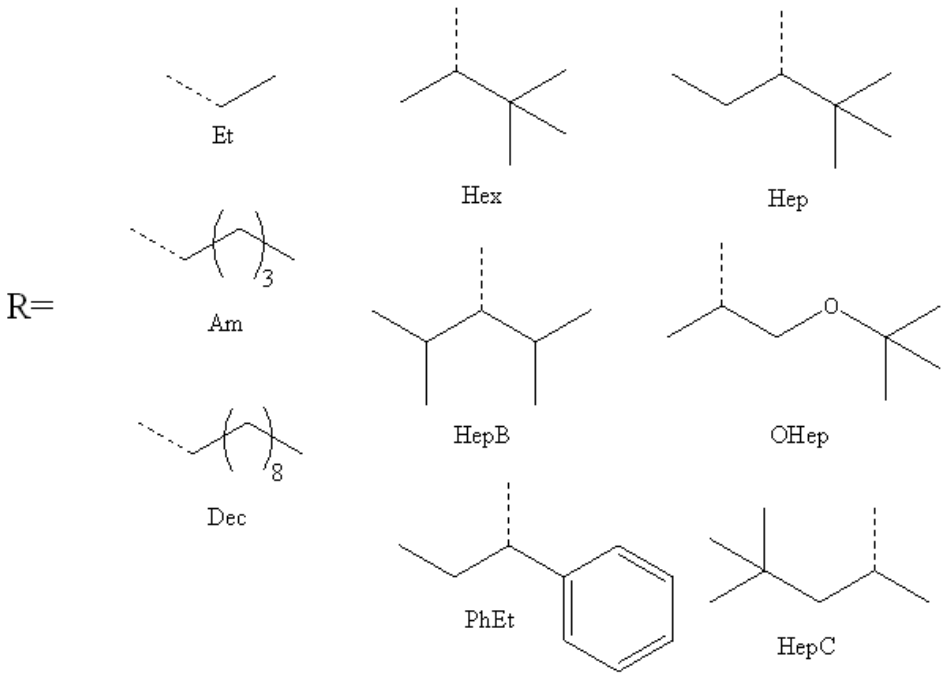

Figure 48: Different alkyl moieties, which were used for the preparation of metal xanthates, including their abbreviation.

Table 10: Synthesized metal xanthates and their corresponding abbreviation. Fields, which show "-" indicate that these metal xanthates were not prepared. "*" indicates, that these xanthates were prepared, however, it was not possible to characterize them with NMR due to their insolubility.

Moiety (R)	K xanthate	Cu xanthate	Zn dixanthate	In trixanthate	Sn tetraxanthate	Sn thio dixantahte
Et	-	Cu Et*	Zn Et	In Et	Sn Et	SnS Et
Am	-	Cu Am	-	-	-	-
Dec	K Dec	Cu Dec*	-	-	-	-
Hex	K Hex	Cu Hex	Zn Hex	In Hex	-	SnS Hex
Hep	K Hep	Cu Hep	Zn Hep	In Hep	-	-
HepB	K HepB	Cu HepB	-	-	-	-
OHep	K OHep	Cu OHep	-	-	-	-
PhEt	K PhEt	Cu PhEt*	-	-	-	-
HepC	K HepC	Cu HepC*	-	-	-	-

K Dec

^{1}H-NMR: ($(CD_3)_2CO$): δ_H/ ppm: 4.34 - 4.29 (t, 2H), 1.66 (q, 2H), 1.44 - 1.18 (m, 14H), 0.87 (t, 3H).

K Hex

^{1}H-NMR: ($(CD_3)_2CO$): δ_H/ ppm: 5.43 - 5.36 (dd, 1H), 1.11 – 1.09 (d, 3H), 0.91 (s, 9H). ^{13}C-NMR: ($(CD_3)_2CO$): δ_C/ ppm: 14.77, 26.46, 35.32, 84.36, 233.65. Anal. Calcd. for $C_7H_{13}OS_2K$: C, 38.85%; S, 29.63%; H, 6.05%. Found: C, 38.75%; S, 29.74%; H, 6.10%

K Hep

^{1}H-NMR: ($(CD_3)_2CO$): δ_H/ ppm: 5.64 - 5.59 (dd, 1H), 1.68 – 1.46 (m, 2H), 0.93 – 0.89 (m, 12H). ^{13}C-NMR: ($(CD_3)_2CO$): δ_C/ ppm: 11.63, 24.11, 26.77, 36.19, 88.68, 235.40. Anal. Calcd. for $C_7H_{13}OS_2K$: C, 41.70%; S, 27.83%; H, 6.56%. Found: C, 41.70%; S, 26.38%; H, 6.59%

K HepB

^{1}H-NMR: ($(CD_3)_2CO$): δ_H/ ppm: 5.56 (t, 1H), 2.00 – 1.85 (m, 2H), 0.91 (d, 12H).

K OHep

^{1}H-NMR: ($(CD_3)_2CO$): δ_H/ ppm: 5.68 - 5.56 (m, 1H), 3.60 – 3.52 (m, 1H) 3.42 – 3.32 (m, 1H), 1.24 (d, 3H) 1.19 (s, 9H). ^{13}C-NMR: ($(CD_3)_2CO$): δ_C/ ppm: 17.37, 27.80, 65.17, 73.47, 76.29, 232.18.

K PhEt

^{1}H-NMR: ($(CD_3)_2CO$): δ_H/ ppm: 7.42 - 7.16 (m, 5H), 6.54 (t, 1H) 2.02 – 1.76 (m, 2H), 0.87 (t, 3H). ^{13}C-NMR: ($(CD_3)_2CO$): δ_C/ ppm: 10.32, 83.42, 127.32, 127.62, 128.53, 143.65, 232.78.

K HepC

^{1}H-NMR: ($(CD_3)_2CO$): δ_H/ ppm: 5.86 - 5.73 (m, 1H), 1.82 – 1.70 (m, 1H), 1.35 – 1.25 (m, 1H), 1.16 (d, 3H), 0.93 (s, 1H). ^{13}C-NMR: ($(CD_3)_2CO$): δ_C/ ppm: 22.23, 30.81, 50.59, 75.50, 232.58.

Cu Am

^{1}H-NMR: ($CDCl_3$): δ_H/ ppm: 4.51 (t, 2H), 1.91 – 1.78 (m, 2H), 1.46 – 1.30 (m, 4H), 0.92 (t, 3H).

Cu Hex

^{1}H-NMR: ($CDCl_3$): δ_H/ ppm: 5.16 - 5.09 (q, 1H), 1.29 – 1.27 (d, 3H), 0.95 (s, 9H). ^{13}C-NMR: ($CDCl_3$): δ_C/ ppm: 14.16, 25.89, 35.42, 93.66, 228.70. Anal. Calcd. for $C_7H_{13}OS_2Cu$: C, 34.91%; S, 26.43%; H, 5.44%. Found: C, 34.31%; S, 27.09%; H, 5.37%.

Cu Hep

^{1}H-NMR: ($CDCl_3$): δ_H/ ppm: 5.27 - 5.17 (t, 1H), 1.75 – 1.66 (m, 2H), 0.94 – 0.89 (m, 12H). ^{13}C-NMR: ($CDCl_3$): δ_C/ ppm: 11.27, 23.51, 26.21, 36.23, 98.93, 230.37. Anal. Calcd. for $C_8H_{15}OS_2Cu$: C, 37.70%; S, 25.15%; H, 5.93%. Found: C, 37.71%; S, 25.62%; H, 5.89%.

Cu HepB

^{1}H-NMR: ($CDCl_3$): δ_H/ ppm: 5.18 (t, 1H), 2.13 – 2.01 (m, 2H), 0.94 (d, 12H).

Cu OHep

^{1}H-NMR: ($CDCl_3$): δ_H/ ppm: 5.48 - 5.34 (m, 1H), 3.66 – 3.40 (m, 2H), 1.41 (d, 3H), 1.19 (s, 9H). ^{13}C-NMR: ($CDCl_3$): δ_C/ ppm: 16.38, 27.52, 63.89, 73.59, 84.75, 228.53.

Zn Et

^{1}H-NMR: ($CDCl_3$): δ_H/ ppm: 4.57 (q, 2H), 1.47 (t, 3H).

Zn Hex

^{1}H-NMR: ($CDCl_3$): δ_H/ ppm: 4.94 – 4.92 (q, 1H), 1.33 – 1.31 (d, 3H), 0.98 (s, 9H). ^{13}C-NMR: ($CDCl_3$): δ_C/ ppm: 14.55, 25.85, 35.30, 95.00, 229.78. Anal. Calcd. for $C_{14}H_{26}O_2S_4Zn$: C, 40.04%; S, 30.54%; H, 6.24%. Found: C, 39.88%; S, 31.03%; H, 6.23%.

Zn Hep

^{1}H-NMR: ($CDCl_3$): δ_H/ ppm: 4.92 (t, 1H), 1.57 – 1.54 (m, 2H), 1.10 - 0.90 (m, 12H). ^{13}C-NMR: ($CDCl_3$): δ_C/ ppm: 11.15, 23.39, 26.13, 36.10, 101.21, 231.22. Anal. Calcd. for $C_{16}H_{30}O_2S_4Zn$: C, 42.89%; S, 28.63%; H, 6.75%. Found: C, 42.45%; S, 28.57%; H, 6.79%.

In Et

^{1}H-NMR: ($CDCl_3$): δ_H/ ppm: 4.51 (q, 2H), 1.50 (t, 3H).

In Hex

^{1}H-NMR: ($CDCl_3$): δ_H/ ppm: 4.75 (q, 1H), 1.35 (d, 3H), 1.00 (s, 9H). ^{13}C-NMR: ($CDCl_3$): δ_C/ ppm: 14.21, 25.58, 35.27, 96.95, 229.27. Anal. Calcd. for $C_{21}H_{39}O_3S_6In$: C, 39.00%; S, 30.25%; H, 6.08%. Found: C, 39.87%; S, 29.75%; H, 6.01%

In Hep

^{1}H-NMR: ($CDCl_3$): δ_H/ ppm: 4.74 (t, 1H), 1.82 – 1.68 (m, 2H), 1.06 – 0.94 (m, 12H). ^{13}C-NMR: ($CDCl_3$): δ_C/ ppm: 10.94, 23.33, 25.90, 36.01, 103.08, 230.80. Anal. Calcd. for $C_{24}H_{45}O_3S_6In$: C, 41.85%; S, 27.93%; H, 6.58%. Found: C, 41.88%; S, 28.39%; H, 6.60%.

Sn Et

^{1}H-NMR: ($CDCl_3$): δ_H/ ppm: 4.56 (q, 2H), 1.50 (t, 3H). ^{13}C-NMR: ($CDCl_3$): δ_C/ ppm: 13.97, 74.28, 220.70. ^{119}Sn-NMR: ($CDCl_3$): δ_{Sn}/ ppm: -738.06.

SnS Et

^{1}H-NMR: (CD_2Cl_2): δ_H/ ppm: 4.49 (q, 2H), 1.50 (t, 3H). ^{13}C-NMR: (CD_2Cl_2): δ_C/ ppm: 13.53, 77.12, 227.53. ^{119}Sn-NMR: ($CDCl_3$): δ_{Sn}/ ppm: -710.12. Anal. Calcd. for $C_6H_{10}O_2S_5Sn$: C, 18.33%; S, 40.78%; H, 2.56%. Found: C, 18.5%; S, 40.9%; H, 2.2%.

SnS Hex

^{1}H-NMR: ($CDCl_3$): δ_H/ ppm: 4.63 (q, 1H), 1.36 (d, 3H), 0.99 (s, 9H). ^{13}C-NMR: ($CDCl_3$): δ_C/ ppm: 14.27, 25.56, 35.45, 98.21, 227.42. ^{119}Sn-NMR: ($CDCl_3$): δ_{Sn}/ ppm: -708.10. Anal. Calcd. for $C_{14}H_{26}O_2S_5Sn$: C, 33.27%; S, 31.72%; H, 5.19%. Found: C, 32.6%; S, 30.7%; H, 4.6%.

3.2.1.4 General procedure for potassium xanthates

For the preparation of potassium xanthates a literature method was adapted.[161] The reaction itself was carried out under vacuum, however, the purification steps were done under ambient conditions. A solution of potassium-*tert*-butoxide (*t*-BuOK) (1 equiv.) in tetrahydrofuran (THF) (approx. 1.7 mL THF/mmol alcohol) was cooled down to 0 °C and the corresponding alcohol (1.1 equiv) was added dropwise. The solution was allowed to stir for 15 minutes before carbon disulfide (CS_2) (1.11 equiv) was added dropwise. The reaction mixture was stirred for at least 4 hours. The reaction solution was decanted into diethyl ether (Et_2O) and the precipitate was filtered and dried under vacuum. The crude product was dissolved in hot acetone, filtrated and the obtained solution poured into Et_2O to obtain the potassium xanthate as a white precipitate, which was filtered and dried under vacuum.

3.2.1.5 General procedure for copper (I) xanthates

A solution of the corresponding potassium xanthate (2.03 equiv.) in H_2O (1.5 mL/mmol potassium xanthate) was added dropwise to a solution of copper (II) chloride dihydrate ($CuCl_2{}^{*}2H_2O$) (1 equiv.) in H_2O (1.5 mL/mmol $CuCl_2{}^{*}2H_2O$). The reaction mixture was allowed to stir for at least 5 hours before the water phase was decanted. The remaining residue was dissolved in chloroform ($CHCl_3$), filtrated, and the obtained solution poured into methanol (MeOH) to obtain the crude product as a green orange precipitate, which was consequently dried under vacuum. To support precipitation the mixture can be reduced under vacuum to

remove excess $CHCl_3$. To obtain the pure Cu xanthate the crude product was washed intensively with n-pentan and dried again under vacuum.

3.2.1.6 General procedure for zinc (II) dixanthates

A solution of the corresponding potassium xanthate (2.05 equiv.) in H_2O (2 mL/mmol potassium xanthate) was added dropwise to a solution of zinc (II) chloride ($ZnCl_2$) (1 equiv.) in H_2O (15 mL/mmol $ZnCl_2$). The reaction mixture was allowed to stir for at least 1.25 hours before it was filtrated. The precipitate was washed with H_2O and dried under vacuum. The crude product was dissolved in $CHCl_3$ and poured into MeOH to obtain the corresponding Zn xanthate as a white precipitate, which was consequently filtered, washed with cold MeOH and dried under vacuum. To help precipitation H_2O can be added to the $CHCl_3$/MeOH mixture.

3.2.1.7 General procedure for indium (III) trixanthates

A solution of the corresponding potassium xanthate (3.05 equiv.) in H_2O (2 mL/mmol potassium xanthate) was added dropwise to a solution of indium (III) chloride ($InCl_3$) (1 equiv.) in H_2O (20 mL/mmol $InCl_3$). The reaction mixture was allowed to stir for at least 2.5 hours before it was filtrated. The precipitate was washed with H_2O and dried under vacuum. The crude product was dissolved in $CHCl_3$ and poured into MeOH to obtain the corresponding In xanthate as a white precipitate, which was consequently filtered, washed with MeOH and dried under vacuum.

3.2.1.8 Procedure for tin (IV) tetraethyl xanthates

For the preparation of tin (IV) tetraethyl xanthate a literature method was adapted.[162] The reaction itself was carried out under vacuum using cannula techniques. Potassium ethyl xanthate (4.53 equiv.) was added to a solution of $SnCl_4$ (1 equiv.) in benzene (40 mL/mmol $SnCl_4$). The reaction mixture was stirred for 1 hour at room temperature, filtrated and the obtained solution reduced under high vacuum to obtain the tin (IV) tetraethyl xanthate as orange oil.

3.2.1.9 General procedure for tin (IV) thio dixanthate

A solution of the corresponding potassium xanthate (1.5 equiv.) in H_2O (1.5 mL/mmol potassium xanthate) was added dropwise to a solution of tin (IV) chloride pentahydrate

($SnCl_4{}^*5H_2O$) (1 equiv.) in H_2O (5.5 mL/mmol $SnCl_4{}^*5H_2O$). The reaction mixture was allowed to stir for at least 5 hours before it was filtrated. The reaction mixture was extracted with $CHCl_3$ and the organic phase was reduced under vacuum and poured into MeOH to obtain the corresponding Sn (IV) thio dixanthate as a yellow precipitate, which was filtrated and dried under vacuum.

3.2.2 Results and Discussion

Metal alkyl xanthates bearing methyl,[157] ethyl[152,157,163,164] or isopropyl[164,165] groups, especially the corresponding Cu alkyl xanthates, show very low solubility in apolar solvents. As a result, these compounds are not suitable to obtain sufficiently concentrated precursor solutions, containing the photoactive polymer and the metal xanthates, for the in situ preparation of CIS/polymer or CZTS/polymer nanocomposite layers. Therefore, the main focus of the presented synthesis strategy was the improvement of the solubility of the metal xanthates precursors in organic solvents. This was accomplished by varying the alkyl side chain of the xanthate moiety. By using secondary alcohols for the synthesis of the potassium alkyl xanthate, instead of primary alcohols, the solubility of the corresponding transition metal xanthate can be increased significantly. Unfortunately, it is not possible to use ternary alcohols as the corresponding metal xanthates are not stable and decompose during the synthesis. This was also observed by Whitmore et al.[166] Using the secondary alcohol 3,3-dimethyl-2-butanol lead to a good solubility of the transition metal xanthates in the desired solvent $CHCl_3$. For the synthesis of the corresponding potassium xanthate (K xanthate), which was subsequently used to obtain the Cu, Zn and In xanthate and the Sn thio xanthate, a previously established procedure[161] was modified.

Despite the fact that $CuCl_2$ is used as reagent and 2 equiv. of K xanthate are added to the reaction, the corresponding Cu xanthate bears only one xanthate moiety. This is caused by an immediate reduction of the formed Cu^{+2} xanthate to Cu^{+1} xanthate during the reaction and the formation of metal free xanthate dimers ($(S_2COR)_2$).[167]

Although the syntheses for various metal xanthates are described in the literature, only very few reports on Sn(IV) xanthates[162,168] can be found. Following published procedures, using the K Hex xanthate, instead of K Et xanthate as stated in the literature, does not give the corresponding Sn(IV) Hex xanthate in pure form. Recrystallization of the crude product does not yield a pure product either. However, we found, that it is possible to synthesize pure

Sn(IV) thio Et dixanthate[168,169] by reacting $SnCl_4{}^*5H_2O$ with K Et xanthate in EtOH. Based on these results we adapted the synthesis of $SnCl_4{}^*5H_2O$ with K Hex xanthate to yield the corresponding Sn(IV) thio Hex dixanthate. Price et al.[170] showed, that the related metal Et carbamate compound, $[(C_2H_5NCS_2)_2SnS]_2$, is an intermediate product appearing during the thermal decomposition of $Sn(C_2H_5NCS_2)_4$. This result is consistent with our observation, as Sn Et tetraxanthate can be transformed into Sn thio Et dixanthate by refluxing in hexane. Therefore, it can be assumed that Sn thio Hex dixanthate is also an intermediate product occurring during the thermal decomposition of Sn Hex tetraxanthate and should form the corresponding SnS_2 in the end. This assumption is confirmed by TG-analysis of Sn thio Hex dixanthate, showing a relative mass loss, which is in accordance to the formation of SnS_2.

In conclusion the successful synthesis of metal xanthates, which are soluble in apolar solvents (metal Hex and Hep xanthates), is presented herein. In particular a special focus was placed on Cu, In, Zn and Sn xanthates, which can be converted to the corresponding metal sulfides, CIS and CZTS. Their good solubility in apolar solvents enables the direct preparation of precursor solutions, containing the photoactive polymer and the metal xanthate precursors, hence, allows a simple in situ preparation of nanocomposite thin films. Before the fabrication of CIS and CZTS nanocomposite thin films, the formation of the pure metal sulfides using xanthates and an apolar solvent ($CHCl_3$) was investigated.

3.3 Metal sulfides prepared from metal xanthates

This chapter focuses on the formation of CIS and CZTS starting from metal xanthates as precursors. A special emphasis is placed on the investigation of the material properties (e.g. crystal structure, crystallinity, optical properties) as a function of different metal ratios within the precursor solution as well as different thermal treatments during the formation of the metal sulfide.

3.3.1 $CuInS_2$

In the case of CIS, two different precursor combinations were studied. An overview of the two precursor systems is given in Table 11.

Table 11: Precursor system used for the preparation of CIS thin films.

	System 1	System2
Cu xanthate	Am	Hex
In xanthate	Et	Hex
Solvent	pyridine/$CHCl_3$ (1/4)	$CHCl_3$

To investigate the formation of CIS from Cu and In xanthates, thick precursor films were thermally treated under vacuum. The Cu/In metal ratio within the precursor solution was adjusted to 1.7 and the overall metal xanthate concentration was set at 0.2 mmol/L (precursor system 1) and 0.15 mol/L (precursor system 2).

Due to the limited solubility of Cu Am xanthate a solvent mixture of pyridine and $CHCl_3$ (1 part pyridine to 4 parts $CHCl_3$) was used as solvent for the precursor system 1. In the case of precursor system 2 straight $CHCl_3$ was used, as Cu Hex xanthate shows an excellent solubility in apolar solvents. The obtained CIS material was analyzed with XRD.

At this stage it is important to highlight, that the formation temperature of CIS should be below 200 °C to be able to prepare an efficient nanocomposite thin film for photovoltaic applications. This value is approximately the highest temperature most photoactive polymers can withstand without severe damage. Therefore, investigations on the formation of the metal sulfides focused on temperatures below 200 °C.

Figure 49 and Figure 50 show the X-ray diffraction patterns obtained from CIS powders prepared using precursor system 1 and 2, respectively.

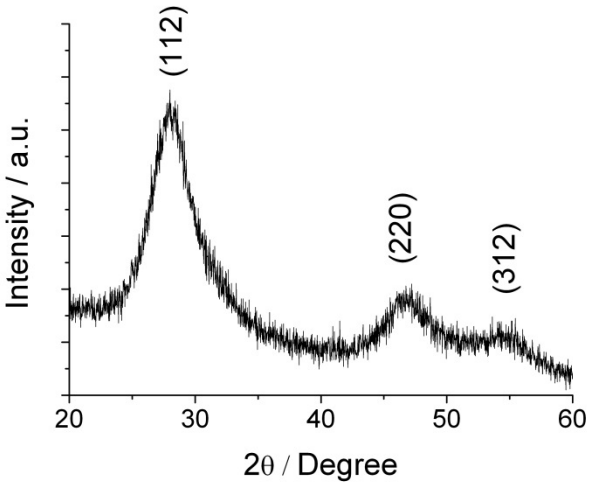

Figure 49: X-ray diffraction patterns of CIS sample prepared at 180 °C under vacuum from precursor system 1 - Cu Am xanthate and In Et xanthates.

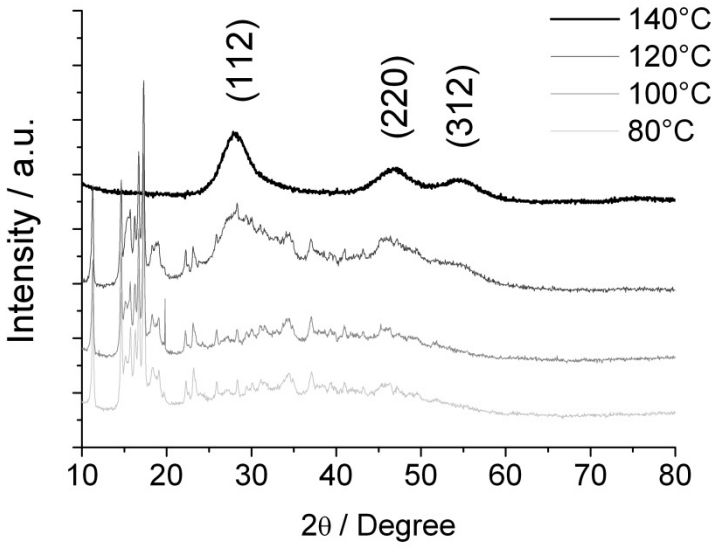

Figure 50: X-ray diffraction patterns of CIS samples prepared at different temperatures under vacuum from precursor system 2 - Cu and In Hex xanthates. Diffraction patterns are shifted vertically for better visibility.

In the case of precursor system 2, the three major X-ray diffraction peaks (112), (220), (312) characteristic for the chalcopyrite structure of CIS are already observed at 120 °C, however, a lot of extra diffraction signals, deriving from the metal xanthate precursors, are still visible. At 140 °C only diffraction peaks corresponding to CIS can be seen, indicating that the xanthate precursors decomposed completely during the thermal treatment.

In the case of precursor system 1 the obtained CIS powders (treated at 180 °C) show similar the XRD pattern as for precursor system 2 at 140 °C.

Based on these results, it can be concluded, that both precursor systems are suitable for the in situ formation of nanocomposite thin films, as the precursors for CIS decompose far below 200 °C, ensuring that the polymer is not damaged.

A more detailed investigation on CIS using metal Hep xanthates as precursor materials can be found in the master thesis of DI Alexander Schenk.[160]

3.3.2 Cu_2ZnSnS_4

In the case of CZTS prepared from metal xanthates only one precursor system was investigated in detail, consisting of Cu and Zn Hex xanthate and Sn thio Hex xanthate and $CHCl_3$ as solvent.

To investigate the influence of the synthesizing temperature and different metal ratios on the formation of CZTS, precursor solutions with three different Cu/(Zn+Sn) metal ratios were prepared and the obtained precursor thin films annealed at three different temperatures. The metal xanthate solutions were prepared using Cu/(Zn+Sn) metal ratios of 1, 0.8 and 0.6, with a fixed Zn/Sn metal ratio of 1. The solutions were spin coated or drop-coated onto glass substrates, which were then baked at 180, 250 and 350 °C to obtain CZTS thin films.

3.3.2.1 Experimental

ITO coated glass substrates were cleaned in an ultrasonic water bath followed by an ultrasonic isopropanol bath, each for 20 min. The CZTS precursor solution consisted of Cu Hex xanthate, Zn Hex dixanthate and Sn thio Hex dixanthate dissolved in $CHCl_3$. Three different solutions with Cu/(Zn+Sn) metal ratios of 1, 0.8, 0.6 with overall metal concentrations of 0.164, 0.157 and 0.148 mol/L, respectively, were prepared. The solution was spin coated at a speed of 1000 rpm on the substrates, which were then baked for 15 min at different temperatures in the range of 180 – 350 °C (heating rate 21 °C/min) under vacuum to form the CZTS-layer. After the heat treatment the samples were cooled down to room temperature under vacuum within 10 min.

For XRD analysis and TEM-EDX measurements the CZTS precursor solutions were drop-coated onto glass substrates at ambient conditions, followed by the same heat treatment of the substrates as described above. Finally the µm thick CZTS layer was scraped off the glass substrate to obtain the CZTS powder.

3.3.2.2 Results and discussion

Thermogravimetric analysis

To study the decomposition behavior of the metal xanthate precursors and the final precursor solution thermogravimetric (TG) analyses were conducted. The metal xanthate precursors were analyzed as synthesized, in contrast to the precursor solution analysis, where the metal xanthate precursors were dissolved in $CHCl_3$ followed by evaporation of the solvent under vacuum.

All three metal xanthate precursors show sharp decomposition onsets and a one-step decompositions. Interestingly, the decomposition onset temperatures (T_d) vary significantly (Figure 51). The precursor solution shows a much lower T_d (117 °C) than the Cu xanthate and Zn xanthate. In addition, when samples containing only Cu and Zn xanthate (Cu/Zn ratio of 1.2) or samples containing Cu xanthate and Sn thio xanthate (Cu/Sn ratio of 1.2) are analyzed, similar observations were made. The decomposition occurs in one step and T_d is approximately the decomposition temperature of Zn xanthate or Sn thio xanthate, respectively. Therefore, an explanation for the reduction of T_d might be, that the decomposition of the xanthate, which decomposes first or intermediate decomposition products thereof, catalyze the decomposition of the remaining xanthates.

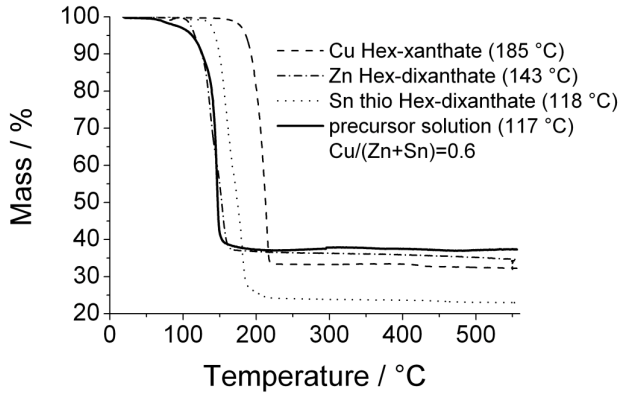

Figure 51: TG analysis of Cu Hex xanthate, Zn Hex dixanthate, Sn thio Hex dixanthate and a precursor solution with a Cu/(Zn+Sn) ratio of 0.6. Decomposition onset temperatures (5 % mass loss) are given in parenthesis.

The measured relative mass losses of the different metal xanthates at 500 °C correspond very well to the theoretic relative mass losses, assuming the decomposition to Cu_2S, ZnS and SnS_2. This good correlation indicates a clean decomposition process of the metal xanthates

to the corresponding metal sulfides. In the case of the precursor solution, the theoretic relative mass loss was calculated on the basis of the starting amount of Cu xanthate within the precursor solution for the compound $Cu_{2.3}ZnSnS_{4.3}$. This formula was derived from TEM-EDX results of the CZTS material annealed at 350 °C using a precursor solution with a Cu/(Zn+Sn) ratio of 0.6.

Table 12: Relative mass losses at 500 °C from the metal xanthates and a CZTS precursor solution (Cu/(Zn+Sn) = 0.6) versus the theoretic relative mass losses. The reference metal sulfides are given in parentheses. *The theoretic relative mass loss is calculated on the basis of the starting amount of Cu xanthate within the precursor solution for the formula $Cu_{2.3}ZnSnS_{4.3}$, which was derived from TEM-EDX results of the CZTS material annealed at 350 °C, using a precursor solution with a Cu/(Zn+Sn) ratio of 0.6.

Sample	**relative mass loss at 500 °C / %**	**relative mass loss (theoretic)**
Cu Hex xanthate	67.5	66.9 (Cu_2S)
Zn Hex dixanthate	77.0	76.8 (ZnS)
Sn thio Hex dixanthate	64.7	63.8 (SnS_2)
precursor solution	62.8	61,4 *

X-ray diffraction

Figure 52 shows the x-ray diffraction patterns for samples synthesized at 350 °C using three different Cu/(Zn+Sn) metal ratios (1, 0.8, 0.6) within the precursor solution. For all samples the major characteristic X-ray diffraction peaks (112), (200), (220), (312) and the minor superstructure reflections (110), (202), (211), (114), (105), (224) of the kesterite CZTS were observed, due to the high crystallinity of these powders. The positions of the reflections are in good agreement with the literature values of crystalline CZTS (kesterite), according to the Powder Diffraction File (PDF) 26-0575 of the International Centre for Diffraction Data.
It has to be noted, that it is necessary to reduce the Cu/(Zn+Sn) metal ratio to 0.6 to obtain single phase CZTS. When higher amounts of Cu xanthate are used an unidentified secondary phase (marked with x in Figure 52) appears.

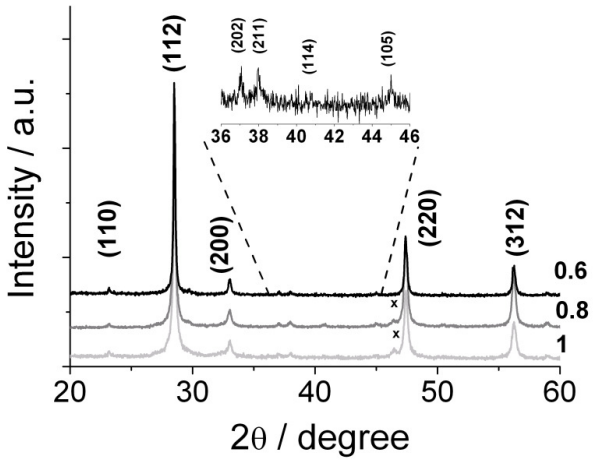

Figure 52: X-ray diffraction patterns of CZTS powders prepared with different Cu/(Zn+Sn) metal ratios annealed at 350 °C. Diffraction patterns are shifted vertically for better visibility.

To investigate the influence of the synthesizing temperature on the obtained CZTS precursor layers, , films with the optimized Cu/(Zn+Sn) metal ratio of 0.6 were heat treated at different temperatures. As expected from TG measurements the precursors form CZTS already at 180 °C, causing the appearance of the (112), (200), (220), (312) diffraction peaks. However, it has to be mentioned, that due to similar crystal structures of ZnS and Cu_2SnS_3,[137] it is not possible to exclude their presence on the basis of XRD results.

The crystallinity of the CZTS materials rises significantly with increasing synthesizing temperature as all reflexes get sharper. This can also be seen from the domain size estimated using Scherrer formula (Table 13).

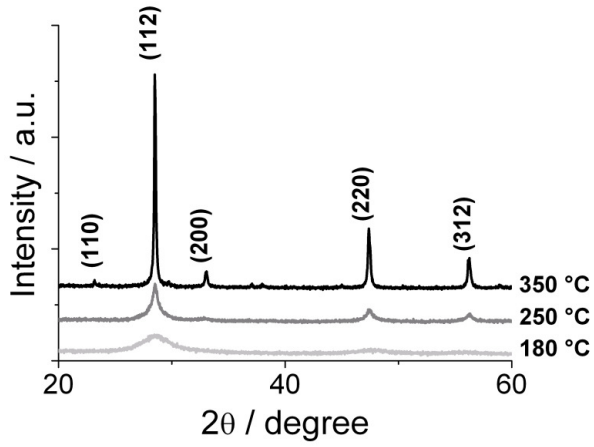

Figure 53: X-ray diffraction patterns of CZTS powders prepared with a Cu/(Zn+Sn) metal ratio of 0.6 annealed at 180, 250 and 350 °C. Diffraction patterns are shifted vertically for better visibility.

Temperature / °C	Cu/(Zn+Sn) = 1	Cu/(Zn+Sn) = 0.8	Cu/(Zn+Sn) = 0.6
180	4.9	6.1	3.4
250	7.3	18.9	15.2
350	33.4	32.8	43.0

Table 13: Crystallographic domain sizes of CZTS powders synthesized at different temperatures and different Cu/(Zn+Sn) ratios within the precursor solution. Primary crystallite sizes were calculated from XRD data using the Scherrer formula.

Chemical composition

The elemental composition of the obtained CZTS powders was determined using TEM-EDX analysis. Figure 54 shows the atomic percentage of the elements for CZTS samples synthesized at 350 °C using a precursor solution with varying Cu/(Zn+Sn) ratios and of CZTS samples annealed at different temperatures with a fixed Cu/(Zn+Sn) ratio of 0.6. The atom percentages were calculated using the Cu K, Zn K, Sn L, and S K peaks using the Cliff-Lorimer approximation.[101] The elemental ratios of Cu/(Zn+Sn), Zn/Sn and S/(Cu+Zn+Sn) are summarized in Table 14 and Table 15.

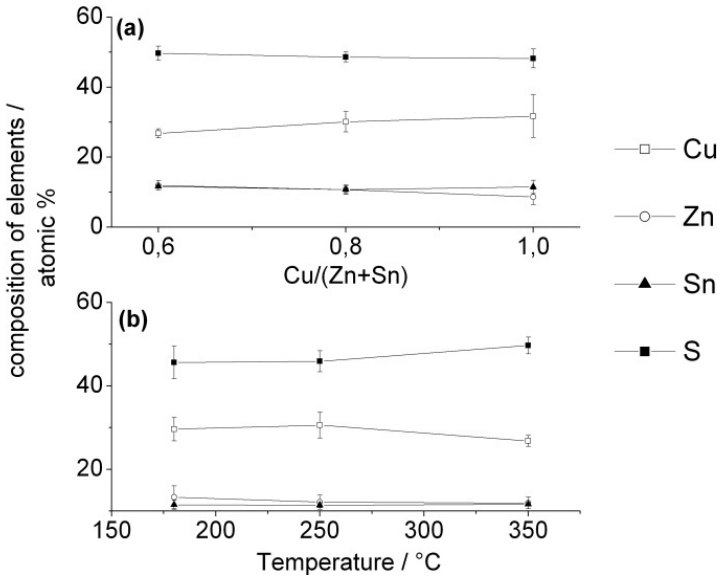

Figure 54: Chemical composition of CZTS films synthesized at 350 °C using precursor solutions with varying Cu/(Zn+Sn) ratios (a) and CZTS films with a Cu/(Zn+Sn) ratio of 0.6 annealed at different temperatures (b).

Table 14: Elemental ratios of the CZTS powders annealed at 350 °C synthesized from precursor solutions with different Cu/(Zn+Sn) ratios. Calculated from TEM-EDX measurements.

Precursor solution	CZTS material		
Cu/(Zn+Sn)	Cu/(Zn+Sn)	Zn/Sn	S/(Cu+Zn+Sn)
1	1.4±0.2	0.8±0.1	1.0±0.1
0.8	1.3±0.1	1.0±0.1	1.0±0.1
0.6	1.1±0.1	1.0±0.1	1.0±0.1

Table 15: Elemental ratios of the CZTS powders synthesized at different temperatures from precursor solutions with a fixed Cu/(Zn+Sn) ratio of 0.6. Calculated from TEM-EDX measurements.

Temperature / °C	Cu/(Zn+Sn)	Zn/Sn	S/(Cu+Zn+Sn)
180°C	1.2±0.2	1.2±0.3	0.8±0.1
250 °C	1.3±0.2	1.1±0.2	0.9±0.1
350°C	1.1±0.1	1.0±0.1	1.0±0.1

All CZTS powders possess nearly stoichiometric amounts of sulfur, with a S/(Cu+Zn+Sn) ratio varying between 1.0 and 0.9, independent from the synthesizing temperature and the Cu/(Zn+Sn) ratio within the precursor solution. Precursor solution with a stoichiometric amount of Cu, Zn and Sn are highly copper rich with a Cu/(Zn+Sn) ratio of 1.4. Additionally, these powders exhibited isolated particles, which contain mainly Cu and S with a Cu/S ratio of approximately 1, indicating the presence of a secondary copper sulfide phase. These particles might be the reason for the observation of the unidentified secondary phase in the XRD spectra, which appeared when precursor solutions with a Cu/(Zn+Sn) ratio above 0.6 were used. With decreasing amount of Cu xanthate within the precursor solution the Cu(/Zn+Sn) ratio within the final CZTS material drops as well. CZTS powders with a nearly stoichiometric composition are obtained when a precursor solution with a Cu/(Zn+Sn) ratio of 0.6 is used.

These deviations from the stoichiometric composition might be caused by a preferred generation of volatile Zn- and Sn-species, compared to Cu, during the thermal induced CZTS formation.

The synthesizing temperature shows only a minor influence on the chemical composition of the obtained CZTS materials (Table 15). It seems that the Zn/Sn ratio decreases slightly and the S/(Cu+Zn+Sn) ratio increases, however these changes should not be over interpreted due to the uncertainty of the TEM-EDX analysis.

Optical properties

To assess the optical properties of the prepared CZTS thin films, transmittance and reflectance measurements were conducted to obtain information about the absorption coefficient and the band gap. The absorption coefficient (α) was calculated according following equation:[102,103]

$$\alpha = \frac{1}{d}\ln\left(\frac{1-R}{T}\right) \qquad (8)$$

where d is the thickness of the film, R the reflectance and T the transmittance of the film.

From Figure 55 it can be seen, that all films show a high optical absorption coefficient lager than 10^4 cm^{-1}, which is in good agreement with other literature reports.[109,112] In addition, the absorption coefficient of the prepared films increases significantly with decreasing Cu/(Zn+Sn) ratio within the CZTS thin films. CZTS films with a stoichiometric composition show an optical absorption of up to $2.5*10^5$ cm^{-1}. It can also be observed, that films synthesized at 180 °C show a slightly lower absorption than film synthesized at higher temperatures, which can be explained by the lower crystallinity of the films and the possibility of remaining impurities at such low temperatures.

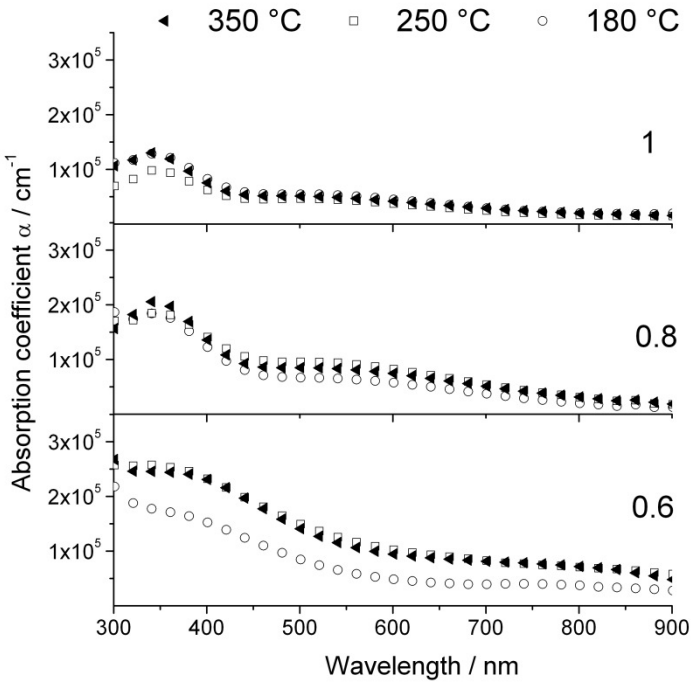

Figure 55: Optical absorption coefficient of CZTS films synthesized at different temperatures and with different Cu/(Zn+Sn) metal ratios within the precursor solution.

The optical band gap (E_g) values were obtained from the equation:

$$\alpha = \frac{A(h\upsilon - E_g)^n}{h\upsilon} \qquad (9)$$

where A is a constant, (hν) the photon energy and n an exponent, which is equal to 2 or ½ for indirect or direct transition, respectively. In the present work n was found to be ½ indicating a direct band gap, which is consistent with the literature.[112] Therefore, the band gap values were estimated from the $(\alpha h\nu)^2$ versus (hν) plots by extrapolating the linear part of the function as shown in Figure 56.

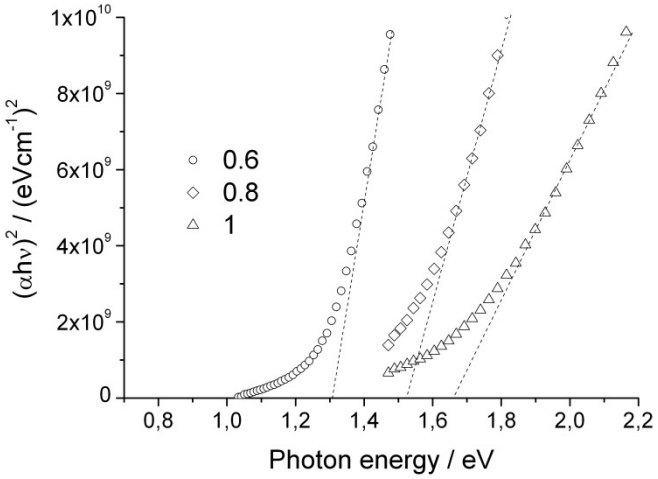

Figure 56. $(\alpha h\nu)^2$ vs. photon energy ($h\nu$) of CZTS films synthesized at 350 °C with different Cu/(Zn+Sn) ratios within the precursor solution.

For films synthesized at 350 °C the obtained band gaps vary significantly, depending on the Cu/(Zn+Sn) metal ratios within the CZTS film. CZTS thin films using a precursor solution with a Cu/(Zn+Sn) ratio of 0.6 exhibit a nearly stoichiometric composition and a band gap of 1.31 eV, which is consistent with literature reports.[126,171] Interestingly, the band gap decreases when the Cu/(Zn+Sn) ratio within the CZTS thin films is lowered from 1.4 to 1.1.

3.3.2.3 Conclusion

For the first time a novel solution based preparation method for CZTS thin films using exclusively metal alkyl xanthates as precursors is presented. Highly concentrated and homogenous precursor solutions using $CHCl_3$ can be prepared and easily applied on suitable substrates by spin coating, due to the low polarity of the solvent. To obtain single phase CZTS thin films with a stoichiometric composition using the presented annealing process, Cu poor precursor solutions have to be used. TG analysis reveals, that the precursors within the precursor film show a one-step decomposition with a decomposition onset at 117 °C, which is much lower than for the isolated metal xanthates. CZTS films with a stoichiometric composition exhibit a very high absorption coefficient (> $2*10^5$ cm^{-1}) and a band gap of 1.31 eV. Summing up, this new method shows the applicability of metal xanthates for the preparation of single phase CZTS thin films with suitable properties for photovoltaic applications.

3.4 Hybrid solar cells

Due to the promising results obtained during the preparation and characterization of CIS and CZTS thin films using metal xanthates as precursors, the fabrication of hybrid solar cells was targeted.

A typical procedure for the fabrication and characterization of nanocomposite solar cells was as follows:

ITO coated glass substrates were cleaned in an ultrasonic water bath followed by an ultrasonic isopropanol bath, each for 20 min. The photoactive polymer was dissolved in $CHCl_3$ by heating the solution up to approx. 70 °C for 5 minutes. Consequently, the metal xanthates were added to the cold solution, which was then stirred until a clear and homogeneous solution formed. In the case of the preparation of the CIS precursor solution using the precursor system 1 (3.3.1), pyridine was added to the $CHCl_3$ after the addition of the metal xanthates to help the solubilization of the Cu Am xanthate. The solution was then spin coated or doctor bladed on ITO covered glass substrates, which were then baked under vacuum to form the nanocomposite (metal sulfide/polymer) layer. After the heat treatment the samples were cooled down to room temperature under vacuum within 10 min. Afterwards, the aluminum (Al) top electrode was deposited at a pressure of 10^{-6} mbar with a thickness of 200 nm to complete device fabrication. I-V curves were measured under N_2-atmosphere using a Keithley-2400 sourcemeter, samples were illuminated by a halogen lamp (P_{in} = 100 $mWcm^{-2}$, illumination power was determined using a calibrated KippZonen CMP-11 pyranometer). EQE spectra were recorded using an AMKO MuLTImode 4 monochromator equipped with a xenon lamp and a Keithley-2400 sourcemeter.

3.4.1 $CuInS_2$/Polymer

For the fabrication of CIS nanocomposite solar cells the precursor system 1 as well as 2 was employed (see Table 11).

The precursor system 1 uses a pyridine/CHCl3 (vol/vol: 1/4) mixture to solubilize the Cu Am xanthate and In Et trixanthate. Due to the high content of $CHCl_3$ various photoactive polymers can be used for the optimization of these solar cells. Table 16 gives an overview of the best solar cell devices obtained with certain CIS/polymer combinations. All devices were prepared with precursor solutions using a Cu/In ratio of 1.7 with an overall metal xanthate

concentration of 0.15 mol/L. The polymer concentration was set at 6 g/mL. The exact spin coating parameters as well as the thermal treatment settings are given in Table 16.

Table 16: Preparation details (polymer, spin program and thermal treatment) and characteristic solar cell parameters for the most efficient solar cell devices using the precursor system 1. The heating rate up to 200 °C was set at 28 °C/min.

Polymer	Spin program	thermal treatment	I_{SC} / mA/cm^2	V_{OC} / V	Efficiency / %
P3HT	500rpm/3sec; 2000rpm/20sec	15min/200°C	0,084	0,221	0,005
P3EBT	500rpm/3sec; 2000rpm/20sec	15min/200°C	0,522	0,533	0,078
MEH-PPV	800rpm/3sec; 2000rpm/20sec	15min/200°C	1,66	0,65	**0,35**
PF-gly	500rpm/3sec; 2000rpm/20sec	15min/200°C	2,41	0,202	0,14
F8BT	800rpm/3sec; 2000rpm/20sec	15min/200°C	0,72	0,52	0,1

Using the precursor system 1, the combination of poly[2-methoxy-5-(2-ethylhexyloxy)-1,4 phenylenevinylene]/CIS (MEH-PPV/CIS) gives the best results concerning the obtained solar cell efficiency. Figure 57 (left) shows the I-V characteristic of the MEH-PPV/CIS solar cell device and Figure 57 (right) gives the corresponding IPCE and UV/vis spectrum. In addition, UV/vis spectra of a pure CIS layer as well as of a MEH-PPV thin film on the same kind of substrate as used for the solar cell are shown. From the IPCE spectrum it can be seen that the solar cell starts to produce a current at around 870 nm, which is approximately the same region where the pure CIS thin film starts to absorb light. This wavelength corresponds to 1.43 eV, hence, this value is in good agreement with the theoretical band gap of CIS at around 1.5 eV[77] and with own results shown in chapter 2.2. As the MEH-PPV polymer starts to absorb light below 700 nm (see UV/vis of pure MEH-PPV thin film) the rise in the IPCE spectra > 700 nm can be solely attributed to charges produced within the CIS phase of the nanocomposite thin film. This shows that the CIS phase contributes significantly to the generation of the photocurrent within the device.

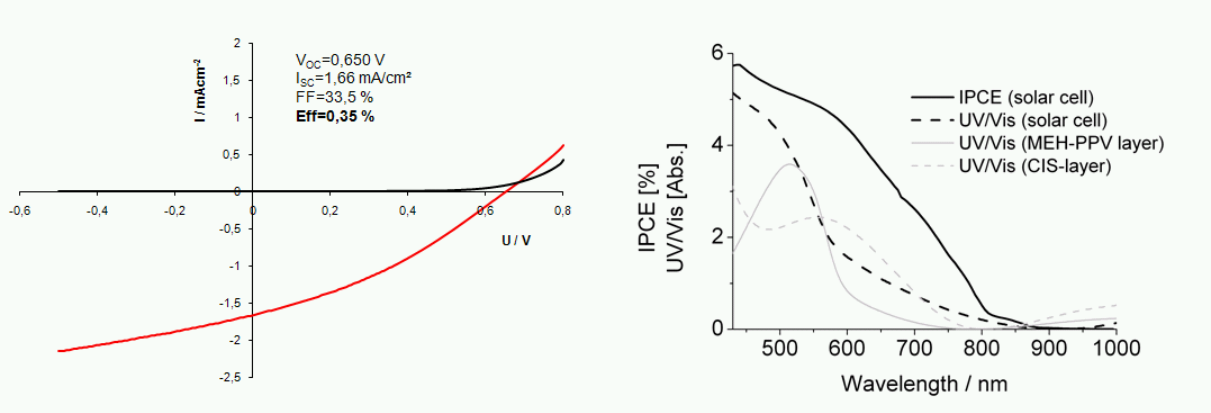

Figure 57: I-V characteristic of a MEH-PPV/CIS nanocomposite solar cell prepared with the precursor system 1 is given at the left. The corresponding IPCE and UV/vis spectrum of the solar cell including the UV/vis spectra of a pure MEH-PPV thin film as well as a CIS layer is shown on the right.

Due to the solvent mixture of pyridine and $CHCl_3$, which has to be used for the precursor system 1, the stability of the precursor solution becomes a critical factor. After the addition of pyridine to the $CHCl_3$ solution, which contains the polymer and the metal xanthate precursors, the xanthate precursors dissolved completely. However, pyridine presents a non solvent for typical photoactive polymers as MEH-PPV or P3HT. This leads to the problem, that after a certain time, depending on the polymer, the precursor solution becomes unsuitable for the fabrication of nanocomposite thin layers. The polymer starts to precipitate or the solution starts to form a gel. This results in a bad reproducibility for the preparation of solar cell devices. Fortunately, the synthesis of metal Hex xanthates solved this issue, as these metal xanthates, especially the Cu Hex xanthates, are soluble in straight $CHCl_3$. As a result, no addition of pyridine is necessary, which leads to the precursor system 2 (Table 11). With this system it is possible to obtain homogeneous precursor films by doctor blading. With the solvent mixture of the precursor system 1 the different evaporation rates of $CHCl_3$ and pyridine caused the formation of inhomogeneous thin film. However, when pure $CHCl_3$ can be used as solvent this problem vanishes completely.

In the case of precursor system 2, the precursor layer was applied by doctor blading, therefore, less concentrated precursor solution with an overall metal concentration of approximately 0.08 mol/L were used.

The following section shows an example of a typical optimization approach for CIS/polymer nanocomposite solar cells using F8T2 as photoactive polymer. The chemical structure of the polymer and the energy alignment within the nanocomposite layer is given in Figure 58.

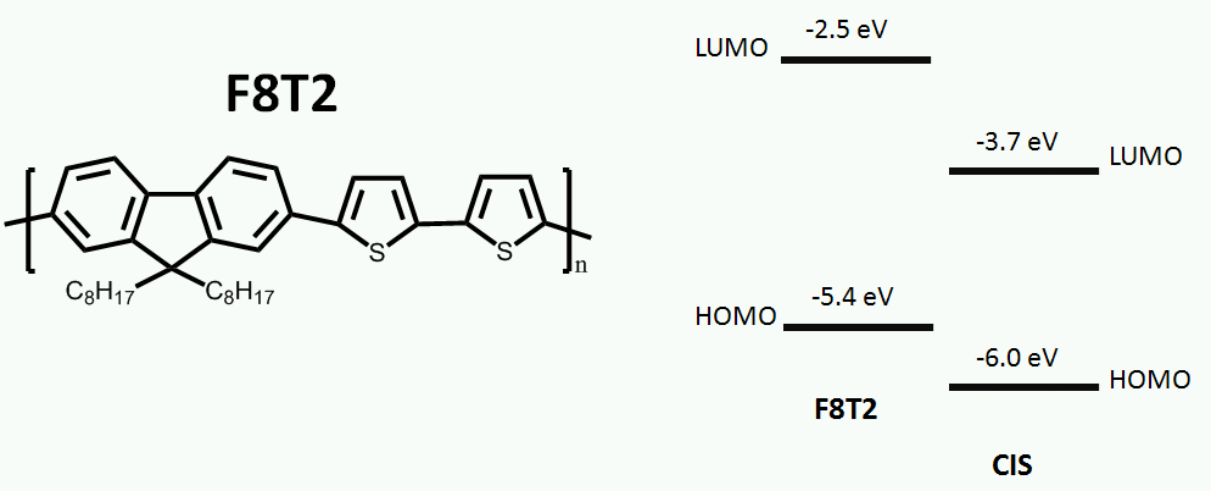

Figure 58: Chemical structure of F8T2 (left) and band alignment within a CIS/F8T2 nanocomposite layer (right).

From the energy alignment it can be seen, that an efficient heterojunction between CIS and F8T2 should be formed, allowing exciton dissociation due to the sufficient large offsets between the HOMO und LUMO levels of the polymer and the CIS phase. The maximum open circuit voltage, which can be obtained, using this material combination, is 1.7 eV (calculated from the difference between the HOMO level of F8T2 and the LUMO level of CIS).

In general, there are two major parameters, which can be optimized regarding the composition of the active layer of a CIS/F8T2 solar cell device. Firstly, the CIS/polymer ratio within the nanocomposite layer and, secondly, the Cu/In ratio within the CIS phase, which is directly linked to the Cu/In ratio within the precursor solution. However, in the case of CIS, it is also possible to influence its performance in solar cells by doping with Ag, Mg, or Zn.[80] Therefore, the doping with Zn was investigated as well by adding Zn Hex dixanthate to the precursor solution. At this stage it has to be noted, that the thermal treatment (200 °C for 15 min; 28 °C/min heating rate) to convert the precursor layer into the final nanocomposite layer is the same for all devices presented in this section. The thickness of the wet precursor layer was varied between 70 and 150 µm by adjusting the height of the knife of the doctor

blade. Typically, the best result were obtained between 90 and 120 µm, yielding nanocomposite layers with a thickness of around 100 nm after the thermal treatment.

Figure 59 shows the influence of the CIS/polymer weight ratio within the nanocomposite layer and its influence on the performance of the solar cells. In these cases the Cu/In ratio within the precursor solution was kept at 1.7 and no doping with Zn was carried out. With increasing CIS/polymer ratio up to 4 the efficiency of the device increases significantly, which is mainly linked to a rise in the short circuit current (I_{SC}). In contrast, CIS/polymer ratios above 4 lead to a decrease in the I_{SC} and the efficiency (η). These observations can be linked directly to the nanomorphological properties of the active layer. Too high polymer contents or too high CIS contents lead to a volumetric mismatch between the two phases, which causes the formation of isolated islands of the low-content phase. A CIS/polymer weight ratio of 4 within the nanocomposite layer leads to an optimized CIS/polymer volume ratio within the nanocomposite layer, hence, to the formation of an efficient nanomorphology, which allows good exciton separation and charge transport at the same time. Interestingly, the fill factor (FF) and the open circuit voltage (V_{OC}) remain more or less constant between a CIS/polymer ratio of 3 and 5.

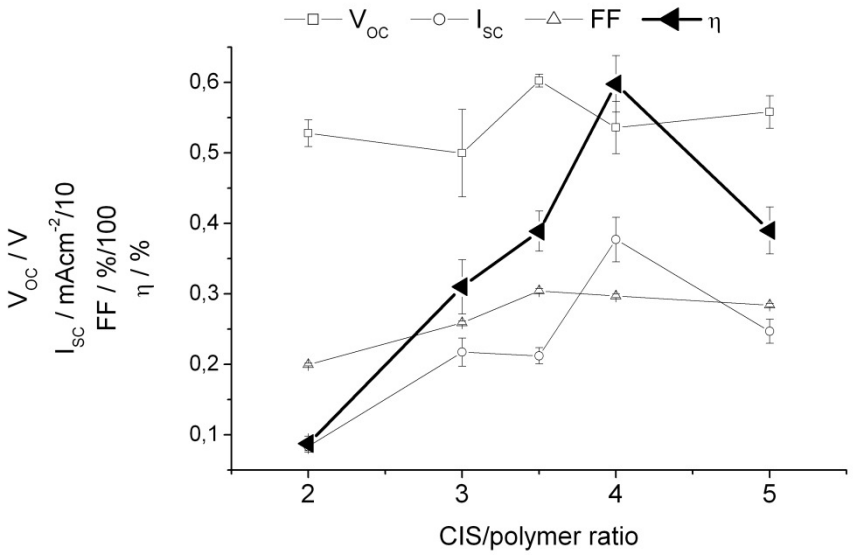

Figure 59: Variation of the CIS/polymer weight ratio within the nanocomposite layer of the solar cell and its influence on characteristic solar cell parameters. Every data point reflects an average of the five most efficient devices.

Apart from the nanomorphology of the active layer, the material properties of the CIS phase can have a significant influence on the obtained efficiency of the solar cells. In this regard, especially the Cu/In ratio within the CIS phase plays a crucial role. This ratio is strongly linked to the Cu/In ratio within the precursor solution and can, therefore, be adjusted easily. Figure 60 gives an overview of the results obtained during the optimization of the Cu/in ratio within the precursor solution. The ratio was varied from 1.3 to 1.9, which is sufficiently high to ensure the formation of n-type conducting CIS.[44] All solar cells within this optimization were fabricated with a CIS/polymer weight ratio of 4 and no doping of the CIS phase with Zn was carried out.

It appears as if the Cu/In ratio is directly connected with the obtained V_{OC} of the devices, whereas other parameters (I_{SC} and FF) show no direct dependence. The highest V_{OC}, hence, the best efficiency, is obtained with a Cu/In ratio of 1.7. Interestingly, a ratio of 1.6 shows a distinct minimum caused by a drop in the V_{OC}.

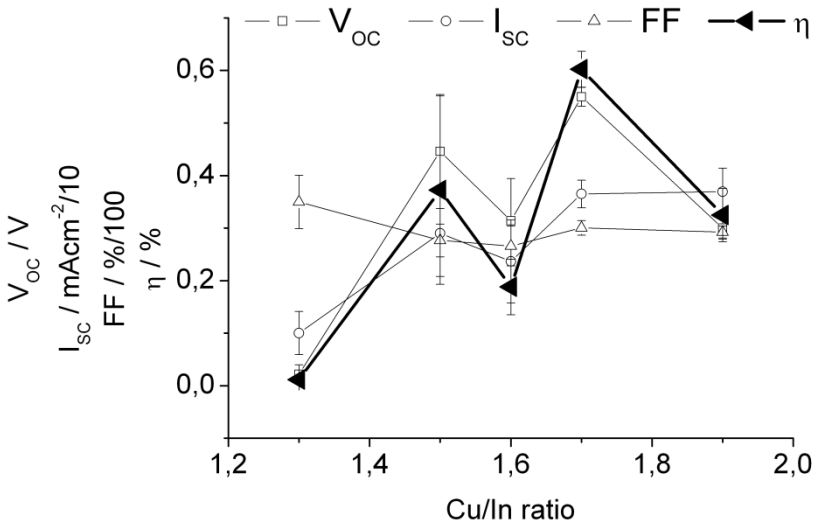

Figure 60: Variation of the Cu/In ratio within the precursor solution and its influence on the characteristic parameters of the obtained solar cells. Every data point reflects an average of the five most efficient devices.

As mentioned above, CIS can be doped by the addition of Zn. This chemical modification leads to an alteration of the optical, structural and electrical properties.[172] Moreover, it was shown that an incorporation of Zn can enhance the V_{OC} of CIS based solar cells.[173] To study the effect of Zn doping of CIS on nanocomposite solar cells, Zn Hex dixanthate was added to the CIS precursor solution (Cu/In molar ratio of 1.7, CIS/polymer weight ratio of 4).

Figure 61 shows the influence of the Zn doping on the solar cell characteristics. The amount of Zn is expressed in the Cu/Zn molar ratio within the precursor solution, which was varied from 0.05 to 1. Up to a ratio of 0.1 an increase in efficiency can be observed, caused by an enhancement of the I_{SC} as well as the V_{OC}. Additions of Zn, exceeding a Cu/Zn molar ratio of 0.1, lead to a significant decrease in efficiency.

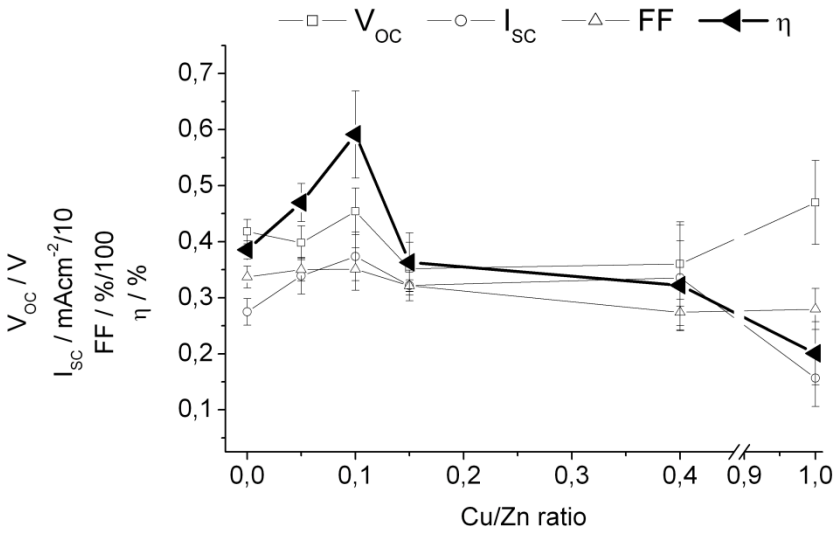

Figure 61: Variation of the Cu/Zn ratio within the precursor solution and its influence on the characteristic parameters of the obtained solar cells. Every data point reflects an average of the five most efficient devices.

In summary, it was clearly shown that the presented CIS/polymer nanocomposite thin films prepared from metal xanthates show an extremely high potential for photovoltaic applications. Especially the metal Hex xanthates, which show a good solubility in $CHCl_3$, are highly interesting, as they allow the usage of a various photoactive polymers for the optimization of solar cells.

3.4.2 Cu_2ZnSnS_4/Polymer

Within this section, the preparation of CZTS/polymer nanocomposite layers is investigated, focusing on the application of these films in photovoltaic devices.

The precursor solutions consisted of Cu and Zn Hex xanthate and Sn thio Hex xanthate dissolved in $CHCl_3$. The photoactive polymer, poly(2-methoxy-5-(3'-7'-dimethyloctyloxy)-1,4-

phenylenevinylene) (MDMO-PPV), was dissolved in $CHCl_3$ and Cu Hex xanthate, Zn Hex dixanthate and Sn thio Hex dixanthate added under stirring. Within the precursor solution the overall metal concentration was kept at 0.08 mol/L, the Cu:Zn:Sn ratio at 2:1:1 and the CZTS/polymer weight ratio at 4. The clear solution was applied by doctor blading to form the precursor thin film, which was consequently heat treated at 200 °C for 15 min (heating rate 28 °C/min) under vacuum.

TEM investigation on the CZTS/MDMO-PPV nanocomposite thin layers (Figure 62 left) show that a homogeneous film, with CZTS agglomerates (20 – 40 nm) embedded within the polymer phase, is formed. In addition, the associated selected area electron diffraction intensity profile (Figure 62, right) confirms the formation of CZTS nanoparticles. The positions of the peaks match perfectly with the Powder Diffraction File (PDF) 26-0575 of the International Centre for Diffraction Data for kesterite CZTS.

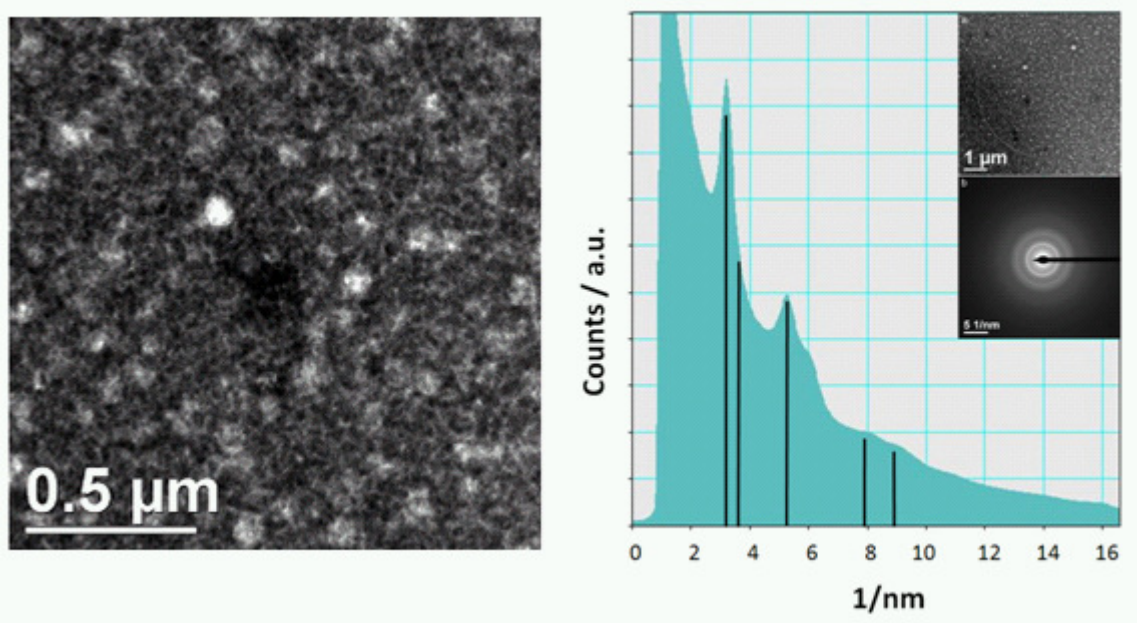

Figure 62: TEM image of a CZTS/MDMO-PPV nanocomposite thin film (left) and corresponding selected area electron diffraction intensity profile (right). Upper inlet shows the investigated area and lower inlet gives the electron diffraction image. Black lines give the position of the peaks according to the Powder Diffraction File (PDF) 26-0575 of the International Centre for Diffraction Data for CZTS.

From the morphological point of view, these nanocomposite CZTS/MDMO-PPV thin films can be regarded as highly suitable for the application in hybrid solar cells, as the inorganic

semiconductor is formed and the phase separation with the polymer occurs in the nanometer range.

Unfortunately, solar cell devices using an ITO/CZTS:MDMO-PPV/Al assembly did not show any noteworthy photovoltaic activity. Even variations of the Cu/Zn or Cu/(Zn+Sn) molar ratio within the precursor solution lead to no improvement of this situation.

As nanomorphological reasons can be excluded, it is very likely, that the mismatch in the conductivity behavior between the CZTS phase and the photoactive polymer is responsible for the bad performance of the cells. CZTS as well as MDMO-PPV show p-type conductivity, therefore, the nanocomposite layer lacks off electron mobility, resulting in an inefficient charge transport.

4 Mesoporous metal sulfide acceptor layers

The most efficient polymer/inorganic hybrid solar cells are based on a bulk heterojunction architecture, where the active layer consists of a blend of organic polymer and inorganic nanoparticles. These blends are normally prepared either by applying a solution of inorganic nanoparticles and organic polymers [72,174] or by direct synthesis of the inorganic nanoparticles within a polymer matrix [47,74,175]. However, in both approaches one of the main bottlenecks for the improvement of the hybrid solar cells is the control of the nanomorphology. On the one hand, this situation is caused by the limited diffusion length of excitons within the organic polymer and, on the other hand, by necessity of a bicontinuous organic/inorganic network to enable an efficient charge transport to the electrodes. A more detailed description of these phenomena can be found in 1.2.1.

A way to gain tight control of the nanomorphology is be to split the preparation of the active layer into two parts (Figure 63). Firstly, a robust inorganic semiconducting layer with a defined nanomorphology is prepared on top of an electrode. Secondly, this layer is infiltrated with an organic polymer before the counter electrode is deposited on top. In this case, the control of the nanomorphology is transferred to the fabrication of the inorganic semiconducting layer.

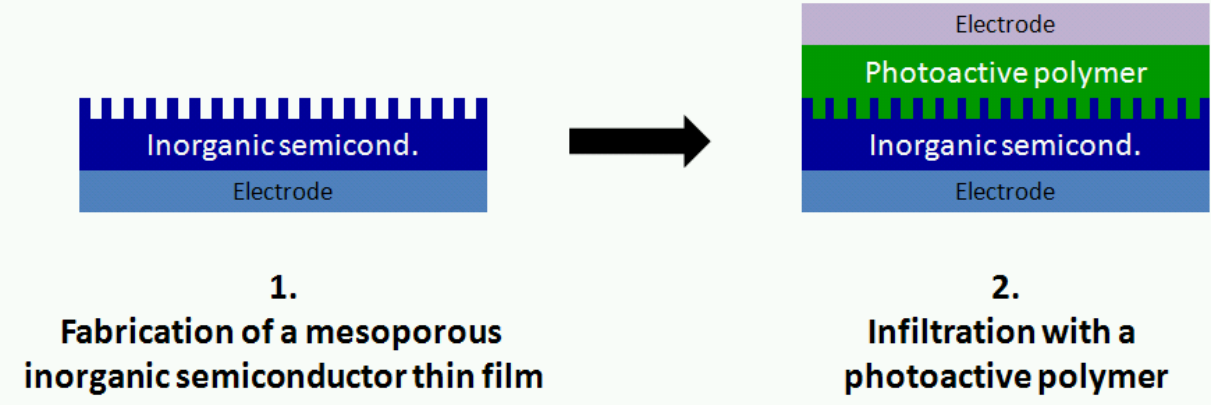

Figure 63: Sequential fabrication of a polymer/inorganic composite layer with a controlled morphology.

The main aim of the last research part of this thesis is the development of a preparation method for mesoporous metal sulfide thin films, which can serve as electron acceptor phase in hybrid solar cells. These films can then be infiltrated with organic polymers to provide the

necessary polymer/inorganic interface for exciton dissociation. As the diffusion length of an exciton within the polymer phase is limited to approximately 10 nm, the pores of the metal sulfide thin film should not be bigger than 20 nm at most to ensure highly efficient exciton dissociation. In addition, it is crucial, that the pores are connected with each other to provide a bicontinuous polymer/inorganic network and percolating pathways to the electrodes for an efficient charge transport. A schematic illustration of the targeted mesoporous 3 D architecture of such a metal sulfide thin film can be seen in Figure 64.

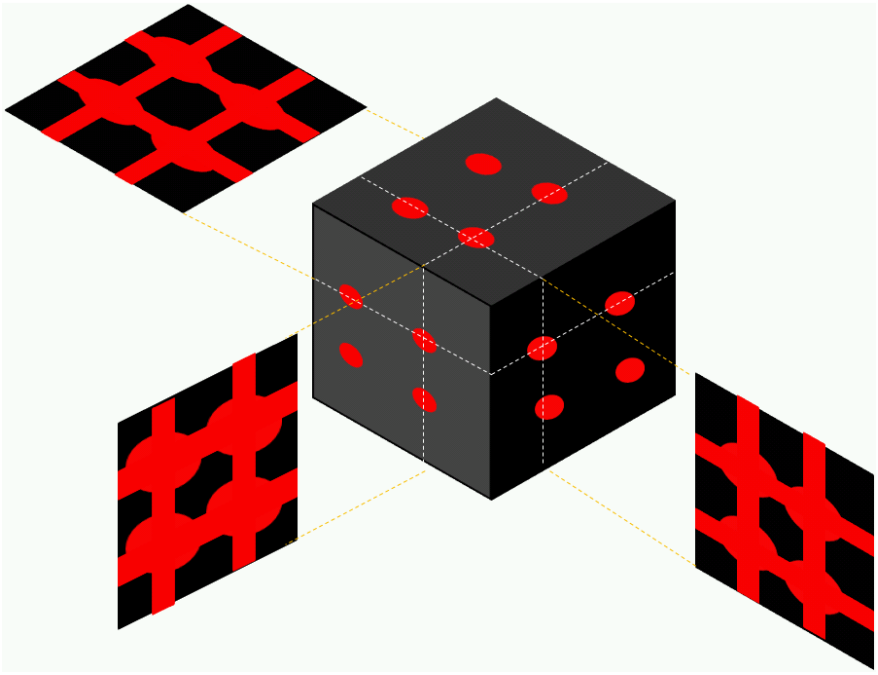

Figure 64: Illustration of the 3 D architecture of a mesoporous metal sulfide thin film.

4.1 Introduction

Since the first reports concerning the preparation of three-dimensional ordered silica networks by supramolecular templating and coassembly,[176,177] mesoporous materials have attracted a lot of scientific attention. Due to their unique properties (highly ordered structure, extremely high surface area (< 2000 m^2g^{-1})), the possibility to tailor their morphological parameters (pore size, pore size distribution, pore geometry, …) and to functionalize the mesoporous materials, they found various applications in fields like biomedicine, catalysis, environmental protection, optics, sensors.[178-182] Beside siliceous materials, mesoporous transition metal oxides, pure metals as well as metal sulfides were

prepared by sol-gel processes, where surfactants are used as structure defining agent.[183-185] However, in the case of non-siliceous materials the involved chemistry is much more difficult to control[186] (redox reaction, hydrolysis, etc.) and especially in the case of metal sulfides, the necessity of favorable interactions between the surfactant and the resulting material, makes their preparation very difficult.[183] In addition, the removal of the surfactant without destroying the mesoporous structure turns out to be difficult, as the single nanoparticles are normally very weakly bound to each other.[187]

These disadvantages can be eliminated by using a nanocasting approach, where mesoporous silica serves as an exotemplate. This robust and universal synthetic method allows the preparation of novel mesoporous materials (e.g. metal sulfides), which cannot be prepared directly by sol-gel processes.[188] After infiltration of the nanospace, provided by the pores of the hard silica template, with the desired material or precursor, further treatments can be carried out without the danger of destroying the mesoporous structure. Therefore, even high surface inorganic compounds, which require high temperatures for their synthesis can be obtained.[189] In addition, the interconnected three-dimensional pore structure of the mesoporous silica allows the formation of a continuous solid phase of the infiltrated nanomaterial. As a result a stable nanostructured material, which possesses the complete topology of the template, can be obtained after the selective removal of the silica template.[190]

In this contribution we focus on the preparation of mesoporous zinc sulfide (ZnS) thin films, which could be applied in electronic devices, like hybrid solar cells. As hard template we use mesoporous silica films prepared by evaporation induced self assembly (EISA),[191] which are consequently infiltrated with ZnS by a successive ionic layer adsorption and reaction (SILAR) process.[30,192,193] In the last step the silica exotemplate is selectively etched away to expose the stable mesoporous ZnS thin film. Various steps of the preparation process as well as the final ZnS thin film are characterized using UV/vis, environmental ellipsometry porosimetry (EEP), scanning electron microscopy (SEM) including energy dispersive x-ray spectroscopy (EDXS) and transmission electron microscopy (TEM) including bright field imaging and selected area electron diffraction (SAED). In addition, small angle x-ray scattering (SAXS) and x-ray reflectomerty (XRR) measurements were performed using synchrotron radiation.

4.2 Experimental

Chemicals

Tetraethoxysilane (TEOS, 99.999 %, trace metal basis), triblock copolymer Pluronic® F-127 (F127, PEO106-PPO70-PEO106, MW ≈ 13,800), zinc (II) chloride ($ZnCl_2$, puriss. p. a.), sodium sulfide (Na_2S, 98%), hydrochloric acid (HCl, 37%, ACS reagent), and ethanol (EtOH, absolute) were purchased from Sigma Aldrich and used without further purification. Millipore water was used for the preparation of all precursor solutions.

Glass substrates were purchased from Marienfield and indium tin oxide- (ITO)-coated glass substrates with a surface resistivity of 15-25 Ω/cm^2 were purchased from Delta Technologies Ltd.

Preparation of mesoporous SiO_2 thin films

Mesoporous silica films (MSF) were prepared on glass with a ZrO_2 buffer layer (glass/ZrO_2) and on ITO-covered glass (glass/ITO) substrates by a sol-gel method based on the oxide precursor tetraethoxysilane (TEOS) using Pluronic® F-127 as templating agent. Prior to deposition, the substrates were washed with Dextran or other suitable surfactant-based cleaning agents, followed by rinsing with water and ethanol. Precursor films were prepared by dip-coating with a withdrawing speed of 4 mms^{-1} under 40-50% relative humidity (RH) at room temperature. The precursor solution was prepared using the following molar ratios: 1 TEOS: 0.0055 F127: 40 EtOH: 10 H_2O: 0.009 HCl. Deposited films were stored immediately in a chamber with 50 % RH for 30 minutes followed by a stabilizing thermal treatment of 30 minutes at 60 °C and 30 minutes at 130 °C. The final calcination was carried out at 350 °C for 2 hours. After this treatment robust and well adhesive SiO_2 films with a defined mesoporous structure are obtained.

Infiltration of the mesoporous SiO_2 films

To infiltrate the mesoporous SiO_2 films with ZnS (MSF:ZnS) a successive ionic layer adsorption and reaction (SILAR) process was used. Each infiltration cycle consisted of four steps (Figure 4): (I) The SiO_2 film is placed for 1 minute in a 0.1 M aq. solution of $ZnCl_2$. Zn^{+2} cations are adsorbed on the surface of the substrate, forming an electrical double layer with the Cl^- anions. The adsorption of Zn^{2+} ions on the surface occurs as long as the isoelectric

point (i.p.) of the substrate (i.p. of $SiO_2 \approx 1.7\text{-}3,5$)[194] is below the pH of the $ZnCl_2$ solution (pH ≈ 6.0). In step (II) the substrate is rinsed with distilled water to remove unadsorbed Zn^{2+} and Cl^- ions from the diffusion layer. In step (III) the substrate is immersed into a 0,07 M aq. Na_2S solution for 1 minute leading to the replacement of the Cl^- ions with S^{2-} ions. Hence, the reaction between the Zn^{2+} and S^{2-} ions occurs, leading to the formation of an insoluble ZnS layer. In the last step (IV), the substrate is washed again with H_2O to remove non-reacted Na_2S molecules.

Characterization

UV-Vis optical characterization of the films was performed with a spectrophotometer Hewlett-Packard 8453. EEP measurements were performed on a UV–visible (240–1000 nm) Variable Angle Spectroscopic Ellipsometer (VASE) from SOPRA (GES5A), and the data analysis was conducted with the WVase 32 software. A dynamic in situ monitoring of the film parameters (index of refraction and thickness) was realized by variation of the relative vapor pressures between 0% and 100% inside the analysis chamber.[195] Field emission-scanning electron microscopy (FE-SEM) images were taken with a ZEISS LEO 982 GEMINI field emission electron microscope in the secondary-electron mode, using an in-lens detector to improve resolution. Energy Dispersive X-ray (EDX) spectra were recorded with a scanning electron microscope using a Philips SEM 515 equipped with a Falcon detector. Transmission electron microscopy (TEM) bright field images were acquired on a Tecnai 20 microscope (FEI Company, 200kV, LaB_6 cathode) and selected area electron diffraction (SAED) patterns were acquired on a Tecnai 12 microscope (FEI Company, 120kV, LaB_6 cathode).

The film density was obtained from the analysis of critical angle and x-ray reflectomerty (XRR) measurements were performed at the D10A-XRD2 line of Laboratorio Nacional de Luz Sincrotron (LNLS), Campinas, SP, Brazil (α=1.5498 Å). In order to obtain accurate density values, measurements were done at low humidity to avoid atmospheric water condensation within the pores that leads to an underestimation of mesoporosity. The film mesostructure was analyzed using SAXS at the D11A-SAXS2 line of LNLS (α=1.608 Å) at normal and 3° incidence.

4.3 Results and discussion

MSF were prepared by an evaporation induced self assembly (EISA)[191] process using F127 as templating agent. The preparation method involved dip-coating of substrates (glass/ITO or glass/ZrO_2) into the precursor solution under controlled atmosphere. After the corresponding thermal stabilization treatment, robust, completely transparent and well-defined mesoporous films were obtained.

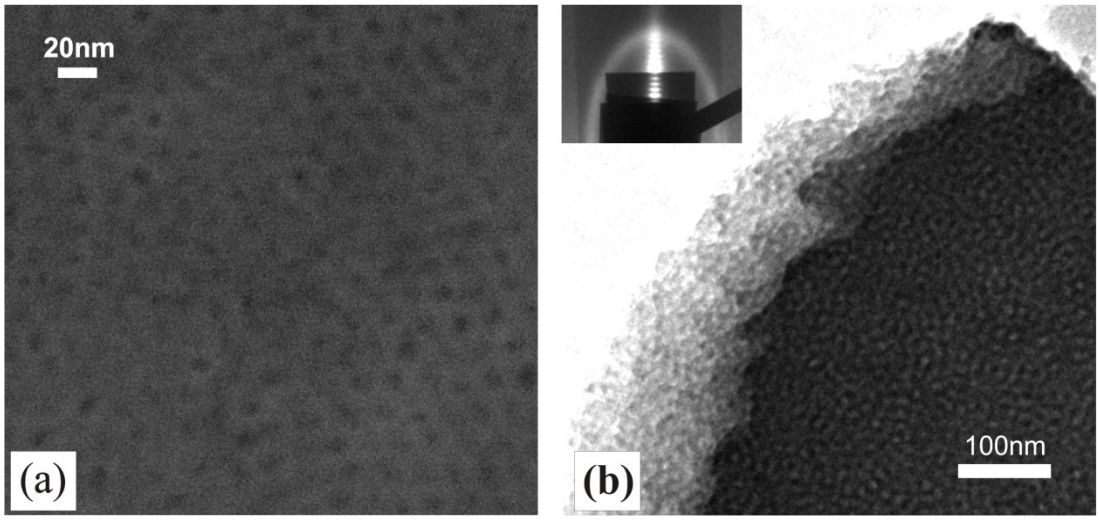

Figure 65: SEM (a) and TEM (b) images of a MSF patterned with F127. Inset in (b) shows a SAXS image at 3° incidence.

Figure 65a shows the SEM image of a MSF prepared on an ITO-covered glass substrate. The porous structure can easily be seen with pore sizes of approximately 6 nm (measured from the SEM image). Figure 1b shows a typical TEM image of the MSF, where it is possible to observe a homogenous mesostructure with a $Im\bar{3}m$/wormlike structure. The inset in Figure 65b corresponds to a 2D SAXS image of a MSF thin film over glass/ZrO_2, where the pattern is a continuous ellipsoidal diffraction, confirming the wormlike structure observed in the TEM image.

The structure (thickness and porosity) and optical characteristics (index of refraction) of the MSF on glass/ITO were obtained using an ellipsometry technique. For this characterization a Cauchy model for the index of refraction for each layer (ITO and MSF) was used. This model expresses the functional dependence of the real and imaginary parts of the index of refraction with wavelength,$n(\lambda) = n_r(\lambda) + in_i(\lambda)$, as follows:

$$n_r(\lambda) = A + \frac{B}{\lambda^2} + \frac{C}{\lambda^4}, \qquad n_i(\lambda) = \frac{D}{\lambda} + \frac{E}{\lambda^3} + \frac{F}{\lambda^5}$$

Where *A, B, C, D, E* and *F* are parameters whose value will be settled according to the modeled material. In case of transparent materials, $n_i(\lambda) = 0$.

Employing UV–VIS spectroscopic ellipsometry measurements in the range of 250 nm to 850 nm and according to the Cauchy model, the obtained parameters at 0% RH for the two layers, ITO and MSF, which compose the structure under study are specified in Table 17.

Table 17: Thickness and optical parameters of the Cauchy model for the MSF and the ITO layers for $250nm < \lambda < 850nm$.

	d [nm]	*A*	*B[μm²]*	*C[μm⁴]*	*D[μm]*	*F[μm³]*	*G[μm⁵]*	*n (0.63μm)*
MSF	202.9	1.25	$1.83e^{-3}$	——	——	——	——	1.26 + 0i
ITO	159.5	1.76	0.103	$-3.62e^{-3}$	$-9.67e^{-2}$	$2.15e^{-2}$	$-8.89e^{-5}$	$1.993-4.31e^{-2}$ i

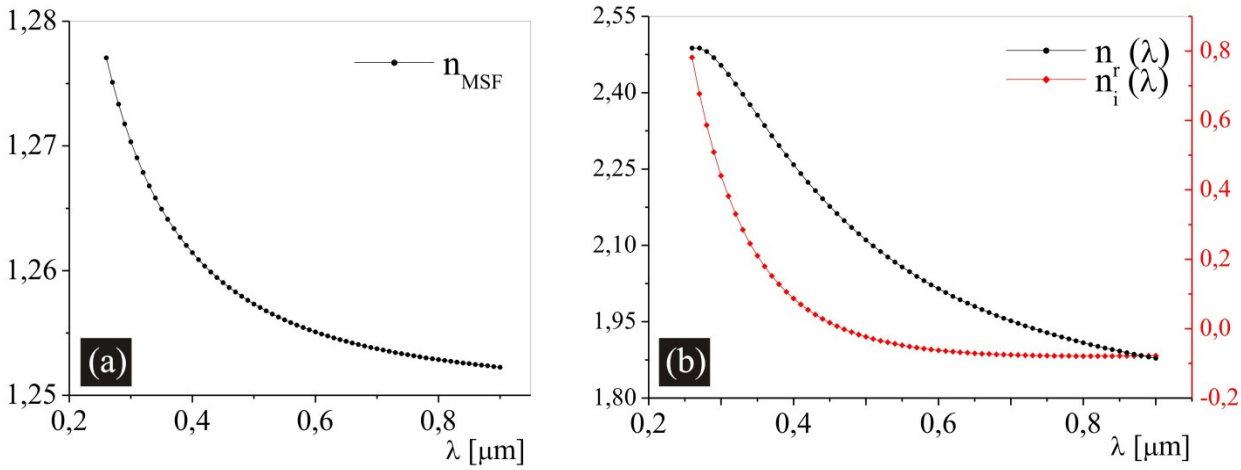

Figure 66: Refractive index curves (a) MSF, (b) ITO layer, corresponding to the parameters shown in Table 17.

The MSF Cauchy parameters show that the MSF has no absorption ($n_i(\lambda) = 0$) and that with just two parameters the index of refraction is well defined. This is not the case of the ITO layer where six Cauchy parameters are necessary to get an appropriate index of refraction

model. The last column of Table 17 shows typical refractive index values for both MSF and ITO layers at 630nm. Plots of these two curves can be observed in Figure 66.

To assess other morphological parameters, such as pore volume and pore and neck size distribution of the MSF, EEP was used. Figure 67a shows the adsorption-desorption isotherms upon variation of the relative vapor pressures between 0% and 100% inside the analysis chamber for the MSF prepared on an ITO-covered glass substrate. The adsorption and desorption isotherms are characteristic for mesostructured materials, showing a steep increase/decrease in adsorption/desorption due to capillary condensation. Figure 65a shows the overall porosity of the film which is approximately 47%. Due to the water pore filling, the MSF refractive index changes upon the variation of the relative vapor pressures, exhibiting values in the range between 1.26 and 1.43. The pore and neck size distribution calculated from the adsorption-desorption isotherms and based on the Kelvin equation[196,197] is shown in Figure 67b. The film exhibits a pore size of around 4.5 nm and neck size of approximately 1.3 nm, which is in accordance with literature data.[198] The pore size obtained by EEP is in accordance with the results obtained from the SEM image analysis (Figure 65).

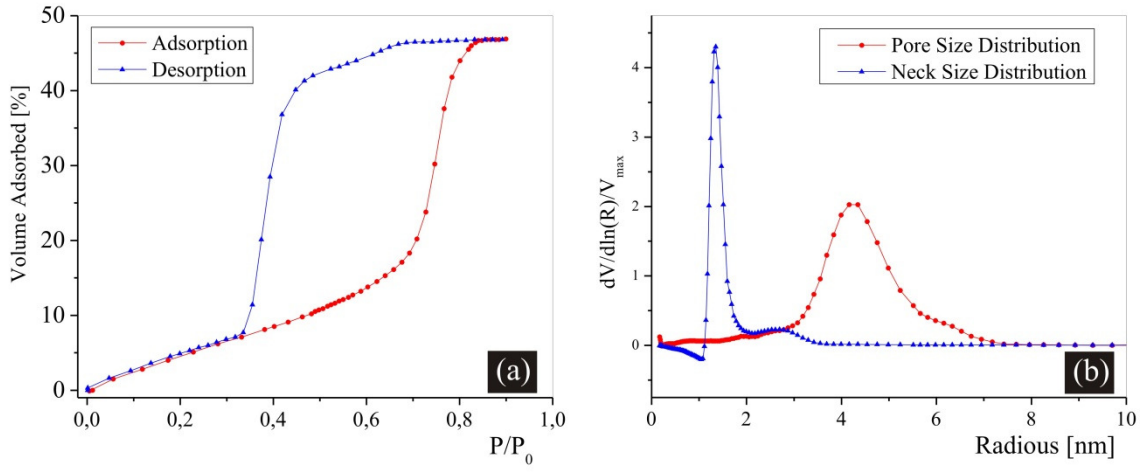

Figure 67: Adsorption-desorption isotherms (a) and pore and neck size distribution of a mesoporous SiO_2 thin film prepared on ITO-covered glass substrate with F127 as surfactant. (b) measured with EEP.

The ZnS infiltration of the silica exotemplate was performed using the successive ionic layer adsorption and reaction (SILAR) process, where alternating solutions of a metal salt ($ZnCl_2$) and a sulfurizing agent (Na_2S) are used.[193,199] The mechanism of the SILAR process for the growth of ZnS thin films is depicted in Figure 68.

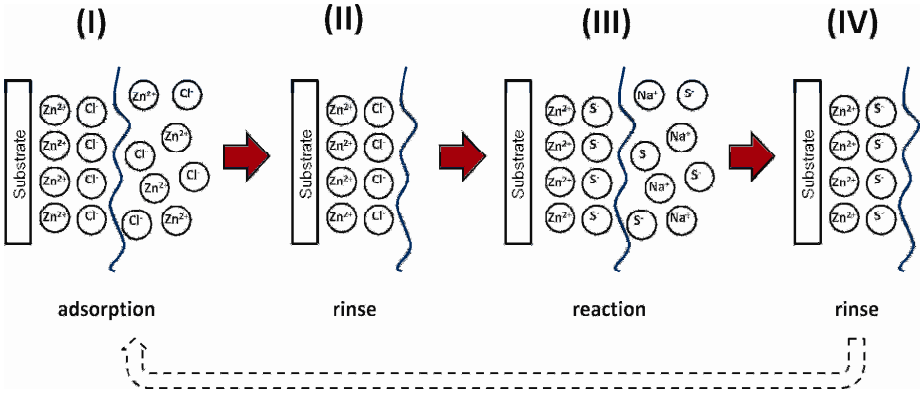

Figure 68: Schematic illustration of the single steps during the infiltration of the MSF substrate using SILAR.

This approach allows a successive and controlled infiltration with ZnS of the exotemplate without the formation of ZnS on the external surface, which would inhibit further infiltrations. In this way, a sufficiently high filling degree of the porosity with ZnS can be reached to obtain a stable mesoporous ZnS thin film after removal of the silica scaffold. To track the proceeding infiltration with ZnS with every SILAR cycle, UV/VIS spectra (Figure 69a) of a MSF prepared on glass/ITO were recorded. The baseline was measured from the same substrate before the infiltration. It can be seen, that the absorption below 340 nm increases significantly, due to the formation of ZnS.

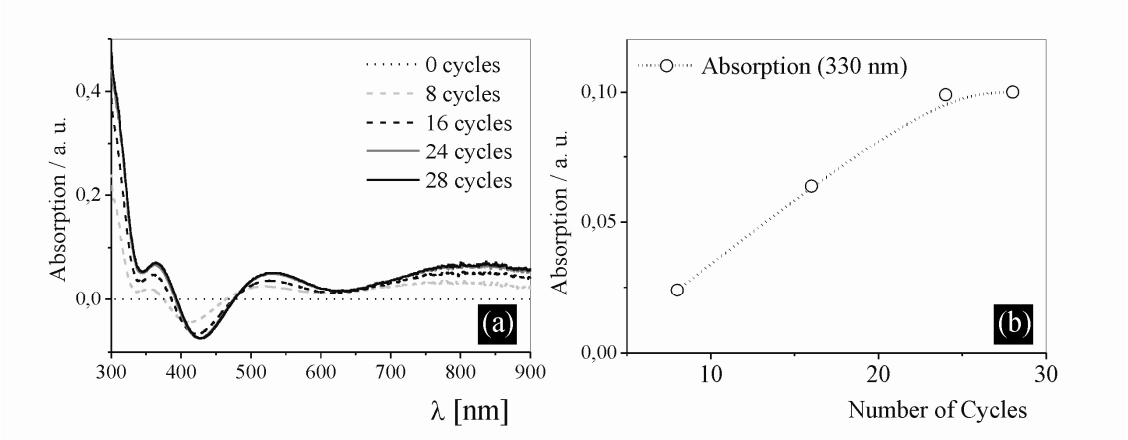

Figure 69: Evolution of the absorption behaviour of a MSF on glass/ITO during infiltration with ZnS (a) and increase of absorption at 330 nm vs. number of infiltration cycles (b).

The appearance of interference fringes can be explained by the change in the refractive index of the MSF thin film due to the infiltration with ZnS. Interestingly, after 24 infiltration cycles, the absorption increase reaches a plateau (Figure 69b), indicating that it is not possible to infiltrate more ZnS.

To obtain a better insight into the infiltration process, SEM images of the film before infiltration (Figure 70a) and after 28 cycles of infiltration (Figure 70b) were recorded.

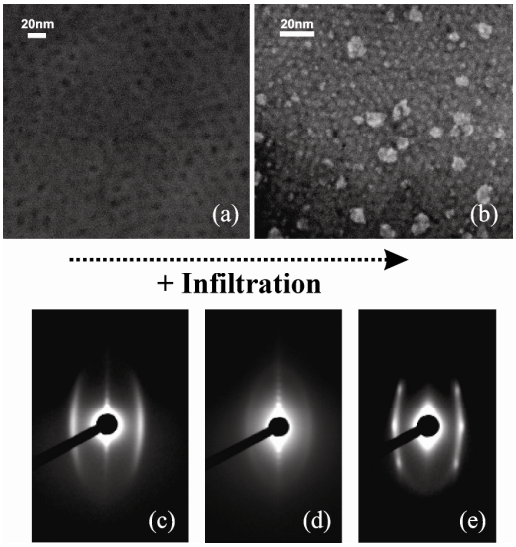

Figure 70: SEM images of a MSF prepared on glass/ITO (a) before infiltration and (b) after 28 cycles of infiltration. SAXS images of a MSF on glass/ZrO_2 for: 0 cycles (c), 14 cycles (d) and 28 cycles (e).

SEM images show that almost all pores (black spots) presented in Figure 70a are filled with ZnS (white spots)[1] in Figure 70b, indicating that the SILAR process leads to a complete infiltration of the mesoporous structure. Figure 70c-e validate these results by showing the evolution of SAXS patterns with ZnS infiltration cycles. Figure 70c exhibits a continuous ellipsoidal diffraction SAXS pattern corresponding to a $lm\bar{3}m$/wormlike structure (as also seen in inset of Figure 1b for an empty - not infiltrated - MSF thin film on glass/ZrO_2. Figure 70d shows how the previous wormlike structure disassembles after 14 ZnS infiltration cycles evidencing a homogeneous but not complete distribution of ZnS infiltration. Noticeably, Figure 70e exhibits a typical $lm\bar{3}m$/ordered SAXS pattern after 28 cycles. This result shows that when almost all the pores are filled with ZnS, the cubic structure is reobtained. This outcome is in very good accordance with Figure 70b where it can be observe that almost all pores are filled with ZnS.

The formation of single clusters, which can be seen in the SEM image after infiltration (Figure 70b), might be caused by the realization of too many infiltration cycles. This is in accordance with the observed plateau of the absorption increase at 330 nm after 24 cycles in Figure 69b.This phenomenon can be explained by taking the difference in surface area at the beginning of the infiltration (empty pores) and the end of the filtration (filled pores) into account, as it is shown in Figure 71.

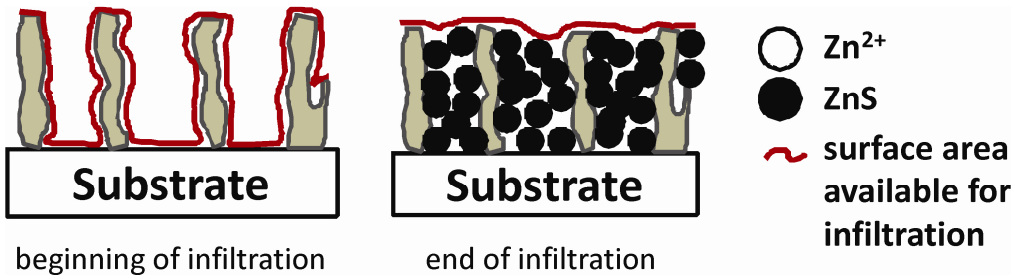

Figure 71: Available surface area at the beginning and the end of the infiltration process.

In the first cycles the pores are nearly empty, therefore, a high surface area (superficial and pore area) is available for the absorption of Zn^{2+}cations. However, after 24 cycles all the

[1]Change in colour is caused by the fact that heavy elements (e.g. Zn) produce more secondary electrons than light elements (e.g. Si). Therefore, regions with heavy elements appear brighter than regions with light elements.

pores are filled in and the surface area for absorption is only limited to the surficial area, which is substantially smaller than the pore area.

For a exact quantification of the ZnS loadings in the SiO_2 template, XRR measurements were performed following previously published procedures.[200] Figure 72a gives XRR diagrams obtained for MSFs prepared on glass/ITO, for different ZnS infiltration cycles. Each XRR measurement shows a signal decay associated to the critical angle (θ_c) which depends directly on the electronic density of each film.[201] As expected, it is possible to observe that θ_c increases with the number of ZnS infiltration cycles, which means that the ZnS inside the thin film is drastically altering the electronic density of the MSF. With this θ_c variation it is possible to calculate the pore filling factor at each infiltration step as it is shown in Figure 72b.

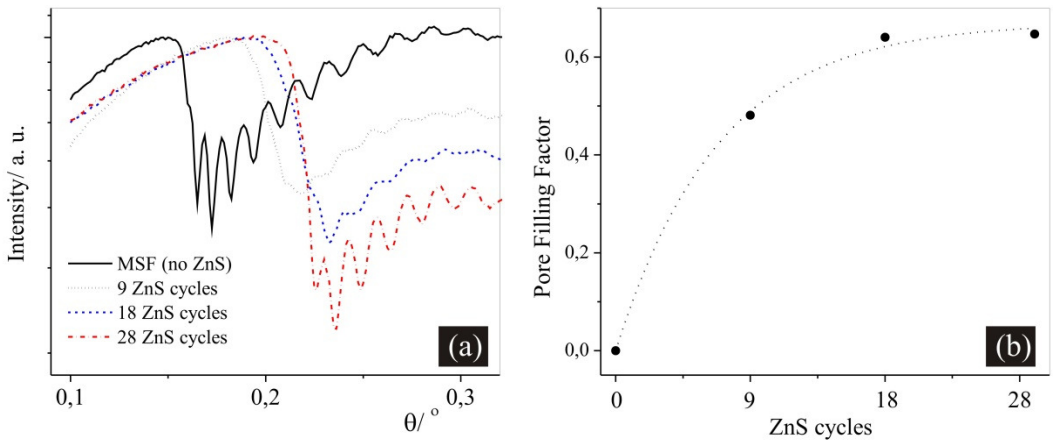

Figure 72: Reflectivity data for the MSF prepared on ITO-covered glass substrate for different ZnS cycles (a), Pore filling factor with ZnS cycles (b).

It is possible to observe in this evolution curve, that a plateau is reached for approximately 20 ZnS infiltration cycles, which is in accordance to the results obtained from the UV/VIS spectra. From this number of cycles onwards, 60-65% of the pore relative volume is filled in. This limit might be due to partial blocking of the necks and pores of the MSF as the number of infiltrations increases. It was observed in additional XRR experiments that the studied films still exhibit a little remaining accessible porosity. For these measurements the films were exposed to high RH (90-95 %) and a small increase in the critical angle was observed, which means that water vapour was adsorbed in the remaining pores.

To expose the mesoporous ZnS structure a 0.5 % ethanolic HF solution was used to dissolve the exotemplate (silica matrix). Due to the similar chemical behaviour of the glass substrates and the silica matrix it is necessary to provide a buffer layer between the glass substrate and the MSF:ZnS to prevent the detachment of the mesoporous ZnS layer during the etching process. Neither the ITO and ZrO_2 layers that covered the glass substrates nor the ZnS are attacked by the etching reagent. In this way the detachment or destruction of the mesoporous ZnS is inhibited successfully.

Figure 73 shows four SEM images for different exposure times (0, 5, 10 and 50 min) of the MSF:ZnS to the HF solution. Figure 73a corresponds to the MSF:ZnS thin film after 28 cycles. After 5 minutes of exposure of the film to the HF solution, a partial dissolution of the SiO_2 matrix can be seen (Figure 73b). This dissolution progresses in Figure 73c and Figure 73d (10 and 50 min of etching). The structure of ZnS (white spots in the Figure 73a) remains unchanged to a large extent and no detaching of the ZnS thin film from the ITO covered glass substrate can be observed.

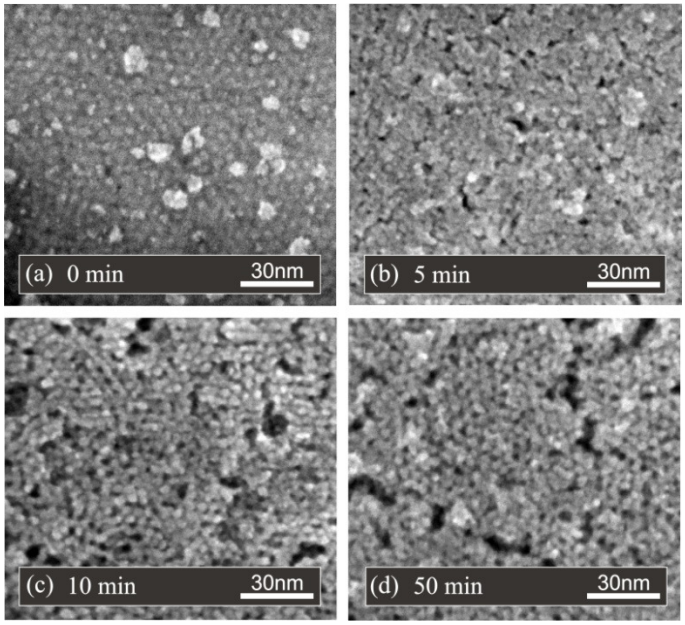

Figure 73: SEM images obtained from Glass/ITO/SF:ZnS samples exposed to HF for (a) 0, (b) 5, (c) 10 and (d) 50 minutes.

The ZnS thin films depicted in Figure 73, which were etched for 0 and 50 minutes, were analyzed with SEM-EDX to obtain information about the SiO_2 content within the MSF:ZnS and the final mesoporous ZnS thin film. The corresponding SEM-EDX spectra as well as the quantification of the elements are shown in Figure 74.

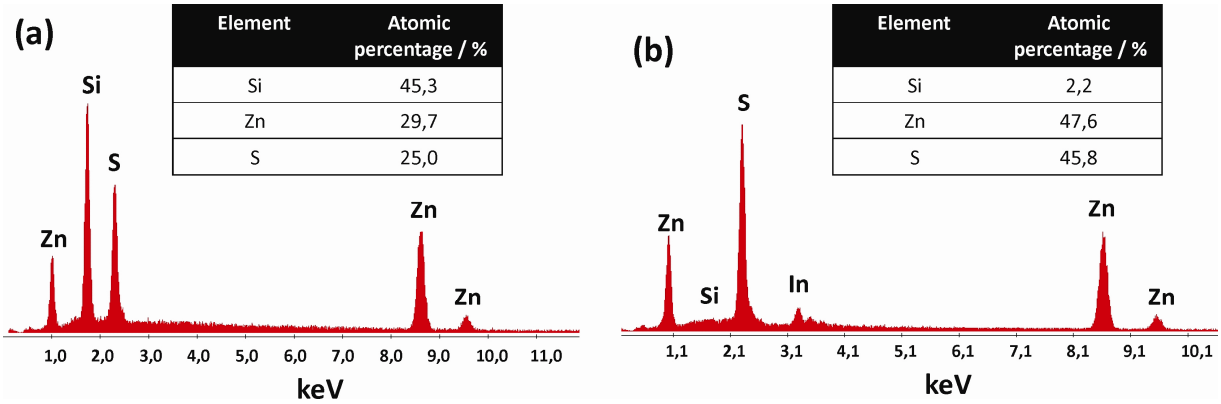

Figure 74: EDX spectra obtained from MSF:ZnS scraped of glass/ITO (28 infiltration cycles) exposed to ethanolic HF for 0 minutes (a) and 50 minutes (b).

The SEM-EDX spectra of a pristine MSF:ZnS film shows three strong signals for Si, Zn and S, corresponding to the SiO_2 matrix (Si) and the ZnS infiltrated MSF (Zn and S). After 50 min etching with 0,5 % ethanolic HF the Si peak in the SEM-EDX spectrum is hardly detectable in contrast to the Zn and S signal, which are still present. This indicates that the SiO_2 matrix is removed successfully by the etching step. In both cases, untreated and etched MSF:ZnS, the ratio between Zn and S is approximately 1:1, which corresponds to ZnS. The weak In peak in Figure 74b derives from the ITO layer of the glass/ITO substrate.

To quantify the porosity of the ZnS mesoporous film after the etching process, XRR measurements were done. Figure 75 shows the different responses of the critical angle for the three main steps in the whole process. Black solid line shows a small θ_c for the not infiltrated MSF while an important increment of the θ_c is observed for the 28 cycle ZnS infiltrated film. (blue dashed line). This change reflects the increment in the MSF:ZnS density as concluded in Figure 72. Noticeably, the red dotted line shows a lower θ_c, indicating that density has lowered down because of the absence of SiO_2 due to the removal of the exotemplate in the etching process. Considering the results obtained in the SEM-EDX and that in other XRR measurements no meaningful difference was obtained for the θ_c between 30 min and 120 min, the resultant porosity of the ZnS film reaches approximately 47%.

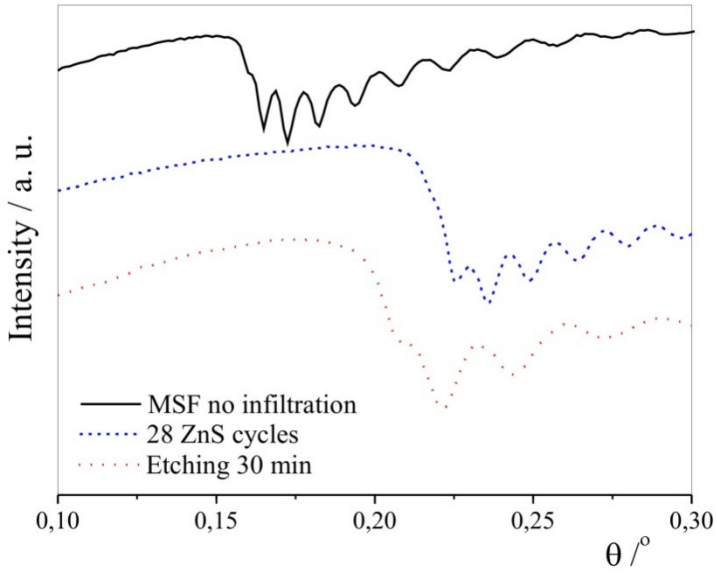

Figure 75: Reflectivity data for a not infiltrated MSF (black solid line), for the 28 ZnS infiltration cycle (blue dashed line) and for an etched ZnS film (red dotted line).

Figure 76a shows a TEM image recorded from a mesoporous ZnS thin film scratched of an glass/ITO substrate, obtained after etching in ethanolic HF solution for 50 minutes. The ZnS pores (black spots) show a long range order, which is consistent with recorded SEM images (Figure 73). To obtain structural information about the mesoporous ZnS, the thin film was studied by selected area electron diffraction (Figure 76b). These measurements were evaluated by using the method described by Mitchell.[202] The electron diffraction shows five well resolved main rings, corresponding to the diffraction of different planes of the randomly ordered nanocrystallites. The positions of the rings can be assigned to sphalerite type ZnS, which is in accordance with the Powder Diffraction File (PDF) 05-05665.

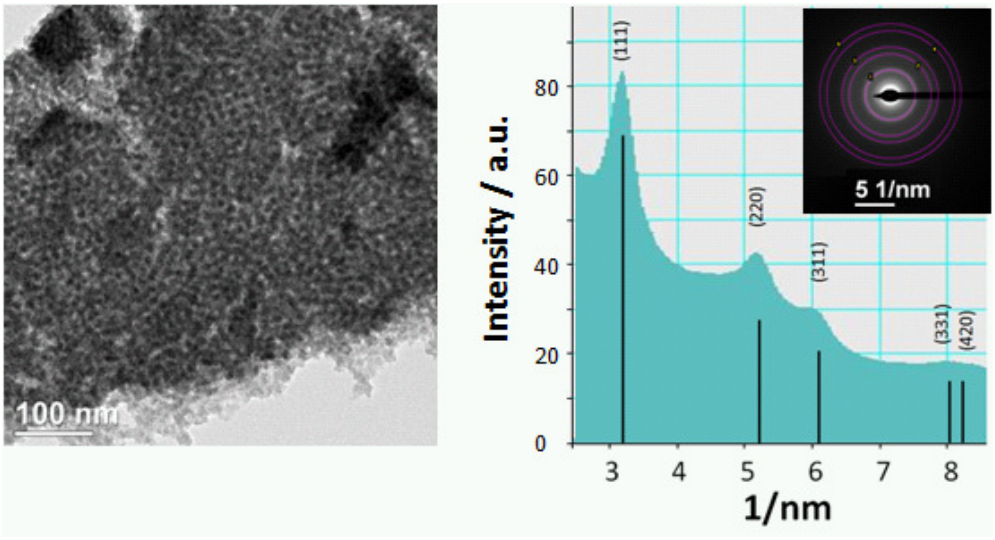

Figure 76: TEM image (a) and electron diffraction analysis and diffraction rings of a mesoporous ZnS thin film (b) scratched off a glass/ITO substrate after removal of the SiO_2 matrix. Black lines give the position of the peaks according to the Powder Diffraction File (PDF) 05-05665 of the International Centre for Diffraction Data for sphalerite type ZnS.

4.4 Conclusion

In this chapter the successful preparation of mesoporous ZnS thin layers by a nanocasting approach is presented. The SiO_2 exotemplate is prepared by evaporation induced self-assembly (EISA) process using Pluronic® F-127 as templating agent. The infiltration of the mesoporous SiO_2 matrix with ZnS is conducted via a successive ionic layer adsorption and reaction (SILAR) approach. In the last step the exotemplate is removed by exposing the film to an ethanolic HF solution yielding a stable and nearly SiO_2 free mesoporous ZnS thin film on a glass/ITO substrate.

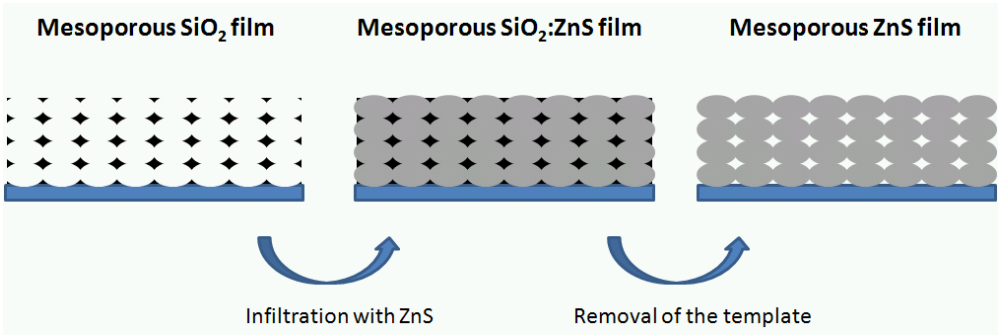

Figure 77: Selected synthesis approach for stable and mesoporous zinc sulfide thin films.

5 Summary

Within this work the formation of non-structured and nanostructured metal sulfide thin films as well as metal sulfide/polymer nanocomposite films is investigated. Furthermore, a special emphasis is placed on their performance in photovoltaic applications such as thin film solar cells and nanocomposite solar cells.

The first two sections (chapter 2 and 3) focus on $CuInS_2$ (CIS) and Cu_2ZnSnS_4 (CZTS) thin films and CIS/polymer as well as CZTS/polymer nanocomposite layers. Chapter 4 deals with the preparation of mesoporous ZnS thin films with a highly defined morphology in the nanometer scale.

The preparation methods presented in chapter 2 and 3 are based on solution based precursor systems (Figure 78). In the first step a precursor solution, containing the metal sulfide precursors in a completely dissolved state, is applied on a suitable substrate. The obtained thin film is thermally treated to convert the precursors into the final metal sulfides. For the preparation of nanocomposite thin films, a polymer is dissolved together with the metal sulfide precursors.

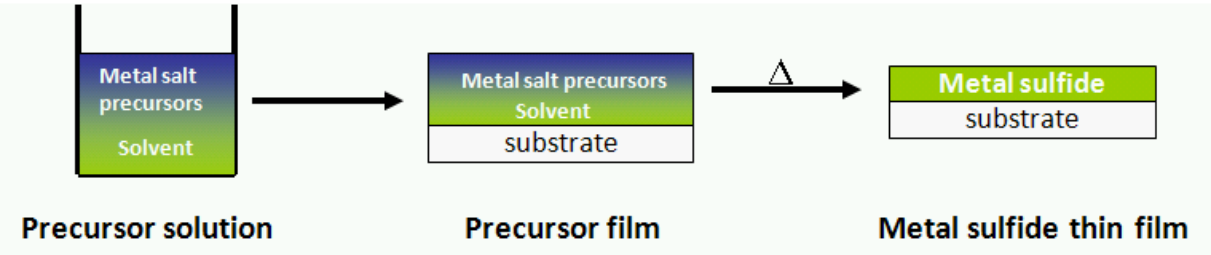

Figure 78: General preparation method for metal sulfide thin films based on a solution based precursor method.

At this stage it has to be noted, that the type of precursors used in chapter 2 and 3 vary significantly from each other, resulting in a completely different chemical behavior and application range of the methods.

Within chapter 2 the metal sulfide precursors consist of metal salts (e.g. CuAc, $InCl_3$, $ZnAc_2$, $SnCl_4{}^*5H_2O$) and an external sulfur source such as thiourea (TU) or thioacetamide (TAA). In this case, the formation of the metal sulfide is initiated by the generation of sulfur containing species deriving from the decomposition of TU or TAA. Due to the high polarity of the metal

salts only polar solvents, such as pyridine, can be used for the preparation of clear precursor solutions.

It was found, that pyridine leads to a significant reduction of the thermal decomposition onset of the external sulfur source compared to similar precursor systems, which are based on water as solvent. In other words, the formation of the metal sulfides takes place at much lower temperatures than the normal decomposition temperature of pure TU or TAA. Especially in the case of CIS, the morphological as well as chemical processes, occurring during the thermal treatment within the precursor layer, were studied intensively using a combination of various analytical techniques (simultaneous TG/MS measurements and simultaneous 2D grazing incident small angle X-ray scattering (GISAXS) and 1D gracing incident wide angle X-ray scattering (GIWAXS) measurements, x-ray diffraction measurements). Figure 79 gives an overview of the most important findings:

At 90 °C metal salt/TU/pyridine complexes within the precursor film, which are embedded in a TU matrix, start to decompose followed by the formation of CIS nanoparticles at 130 °C. Afterwards the TU matrix decomposes at 180 °C, which causes the formation of a dense metal sulfide thin film.

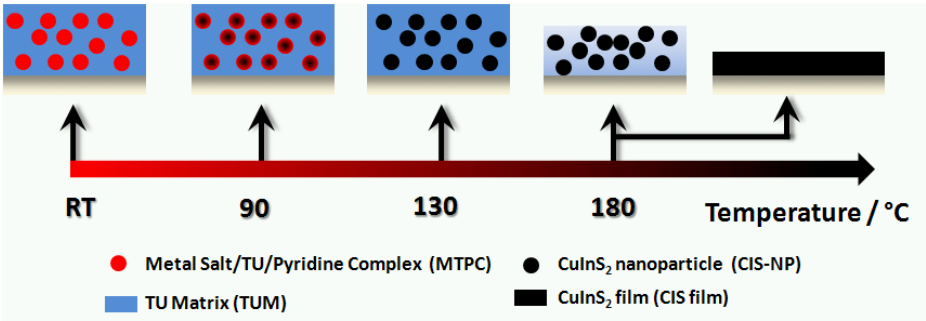

Figure 79: Distinct structural and chemical processes occurring during the formation of CIS thin films using metal salts and TU as precursors.

However, in the case of CIS, where TU is used as external sulfur source, the formation of melamine, caused by the trimerisation of TU, was observed during the thermal treatment of the precursor films. Regarding the application of this precursor system for an in-situ formation of nanocomposite thin films, this situation is problematic. To avoid a thermally induced damage and/or breakdown of the polymer, precursor thin films can only be heated up to approximately 200 °C. Therefore, melamine, which has a decomposition temperature

of 270 °C, remains within the nanocomposite layer, which leads in turn to a lower performance of these films in photovoltaic devices.

Triggered by these results, the external sulfur source for the preparation of CZTS thin films was changed from TU to TAA. As this compound is chemically similar to TU, the trimerisation reaction can still take place, however, the formed 2,4,6-trimethyltriazine exhibits a very low boiling point (176 °C at 1 atm) and is removed easily from the active layer during the thermal treatment. In addition, CZTS forms already at 105 °C, which is even lower than in the case of CIS. For higher synthesizing temperatures (> 250 °C) single phase CZTS with kesterite structure is obtained, exhibiting a very high crystallinity (primary crystallite sizes up to 150 nm). Despite the fact that a stoichiometric precursor solution is used, the final CZTS powders exhibit a Cu-poor and Zn-rich nature.

The optical and electrical properties of the prepared CIS and CZTS thin films were in agreement with literature. The films possessed a high absorption coefficients and band gaps between 1.3 - 1.6 eV, which makes them ideal for the application in photovoltaic devices.

To investigate the performance of the melamine-free CZTS thin films, thin film solar cells with a simple ITO/CZTS/CdS/Al assembly were fabricated and characterized. Despite the fact, that the active layer was only 120 nm thick and that these cells were not optimized in any kind, efficiencies up to 0.5% were reached, showing the potential of this synthetic route based on metal salts and TAA for CZTS layers.

Concerning the fabrication of nanocomposite thin films using the described precursor system within chapter 2 two main problems can be identified. Firstly, the obtained CIS and CZTS material shows p-type conductivity, which inhibits the formation of an efficient heterojunction with p-type photoactive polymers. In contrast to CZTS, CIS can be converted to n-type conductivity by changing its chemical composition, however, a second major problem exists. The presented precursor system is restricted to polar solvents to be able to dissolve the metals salts and the external sulfur source. This situation makes it impossible to prepare clear precursor solutions with the majority of photoactive polymers. This limitation presents a considerable bottleneck for the potential application of this system for the in situ preparation of nanocomposite solar cells.

To improve this situation, a new precursor system, based on sulfur containing metal-organic complexes, named metal xanthates, was developed. Chapter 3 describes the synthetic progress towards metal xanthates, which are highly soluble in organic solvent as well as their

application for CIS and CZTS thin films. In addition, these precursors were used for the preparations of CIS/polymer and CZTS/polymer nanocomposite solar cells.

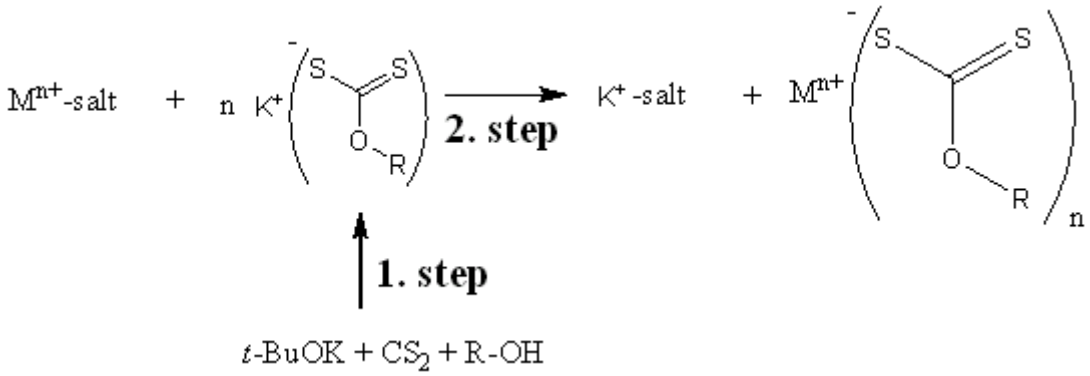

Figure 80: General preparation steps towards transition metal xanthates.

The synthesis of transition metal xanthates is carried out in two steps (Figure 80). Firstly, a potassium xanthate is prepared using a potassium base, carbon disulfide and a chosen alcohol. Afterwards this xanthate is reacted with a transition metal salt to form the final transition metal xanthate. The solubility of the xanthate can be altered by varying the alkyl moiety, which depends in turn on the alcohol used in the first step.

In this part the most crucial point was the solubility enhancement of Cu xanthate, which is used for the preparation of CIS as well as CZTS. In contrast to Zn, In and Sn xanthates, Cu xanthate bears only one xanthate moiety. Whereas Cu xanthates with linear alkyl chains show low solubility in organic solvents, this situation can be improved significantly by changing to branched alkyl chain. The chemical structure of Cu Hex and Cu Hep xanthate, two highly soluble Cu xanthates with branched alkyl chains, is given in Figure 81.

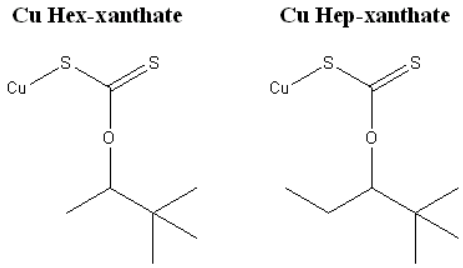

Figure 81: Chemical structure of Cu Hex and Hep xanthates.

In the case of the Sn xanthates, the corresponding Sn (IV) tetraxanthate, which bears four xanthate moieties, could not be prepared with branched alkyl chains in pure form, therefore, the synthetic strategy was changed towards a chemically related Sn (IV) thio dixanthate. This Sn xanthate consists of two Sn atoms, which are bridged via two sulfur atoms, bearing two xanthate moieties each (see Figure 82).

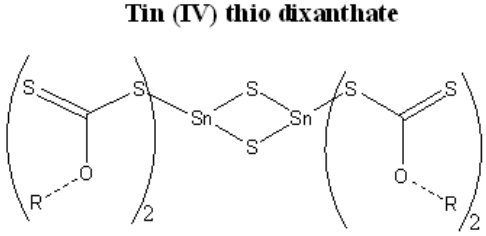

Figure 82: Chemical structure of Sn (IV) thio dixanthate.

Consequently, CIS and CZTS thin films were prepared and studied using precursor solutions containing the described Cu, In and Zn Hex xanthates and Sn thio Hex dixanthate, dissolved in $CHCl_3$.

In the case of CZTS the involved decomposition processes as well as the influence of different Cu/(Zn+Sn) metal ratios within the precursor solution and different synthesizing temperatures (180 – 350 °C) was investigated. Thermogravimetric analysis revealed, that the precursors within the precursor film show a one-step decomposition with a decomposition onset at 117 °C, which is much lower than for the isolated metal xanthates.

In addition, it is necessary to use Cu poor precursor solutions to obtain single phase CZTS thin films with a stoichiometric composition. In general, the films exhibit a very high optical absorption coefficient (> $2*10^5$ cm^{-1}) and a band gap between 1.3 and 1.5 eV, which is ideal for photovoltaic applications.

Based on the successful application of this new precursor system for CIS and CZTS thin films, nanocomposite CIS/polymer and CZTS/polymer solar cells were fabricated using metal xanthates as precursor materials. Depending on the alkyl moiety of the metal xanthates, solvent mixtures of $CHCl_3$ and pyridine (linear alkyl moieties) or pure $CHCl_3$ (Hex and Hep xanthates) can be used for the preparation of the precursor solution. In both cases it is possible to dissolve various kinds of photoactive polymers within the precursor solution. Consequently a broad range of polymers (e.g. P3HT, MEH-PPV, F8BT, F8T2, MDMO-PPV) can

be used for the in situ fabrication of nanocomposite thin films and for the optimization of nanocomposite solar cells.

As expected from previous results from chapter 2, CZTS/polymer nanocomposite solar cells did not show any noteworthy photovoltaic response, due to the conductivity mismatch of the CZTS and polymer phase.

However, in the case of CIS/polymer nanocomposite solar cells, very promising results were obtained. The Cu/In ratio within the precursor solution was kept above 1 to ensure the formation of CIS with n-type conductivity. In this way an efficient heterojunction can be created with a p-type conductive photoactive polymer.

Within this chapter a typical optimization procedure for CIS/F8T2 solar cells is illustrated. After optimizing the Cu/In molar ratio and the CIS/polymer weight ratio, the influence of doping CIS with Zn atoms was investigated as well. Record efficiencies, exceeding 0.6 %, were already achieved after very short time, proofing the high potential of this metal xanthate based precursor method for nanocomposite solar cells. Although the in situ formation approach for the preparation of nanocomposite thin films leads to remarkably good efficiencies for CIS/polymer nanocomposite solar cells, a tighter control of the morphology of the active layer would be desirable. The inorganic semiconducting phase forms within the polymer matrix during the thermal treatment of the precursor layer, hence, the morphology can only be influenced indirectly by changing preparation parameters. A possible way to improve this situation is to divide the preparation of the nanocomposite layer into two parts. Firstly, a mesoporous metal sulfide thin film, with a precisely controlled morphology is prepared. Secondly, this film is infiltrated with the photoactive polymer to form a heterojunction and the final nanocomposite thin layer.

The preparation of such a mesoporous metal sulfide thin film with a precisely defined morphology is investigated in chapter 4. The presented results were obtained during a 7-months research stay in Buenos Aires (ARG) at the Comisión Nacional de Energía Atómica (CNEA) in the research group of Prof. Dr. Galo Soler-Illia.

The used synthetic strategy was based on a nanocasting approach (Figure 83). In the first step a SiO_2 exotemplate was prepared by an evaporation induced self assembly (EISA) process using Pluronic® F-127 as templating agent. Then this mesoporous SiO_2 matrix was infiltrated with ZnS via a successive ionic layer adsorption and reaction (SILAR) method. In the last step the exotemplate was removed by exposing the film to an ethanolic HF solution

yielding a stable and nearly SiO_2 free mesoporous ZnS thin film on an ITO covered glass substrate.

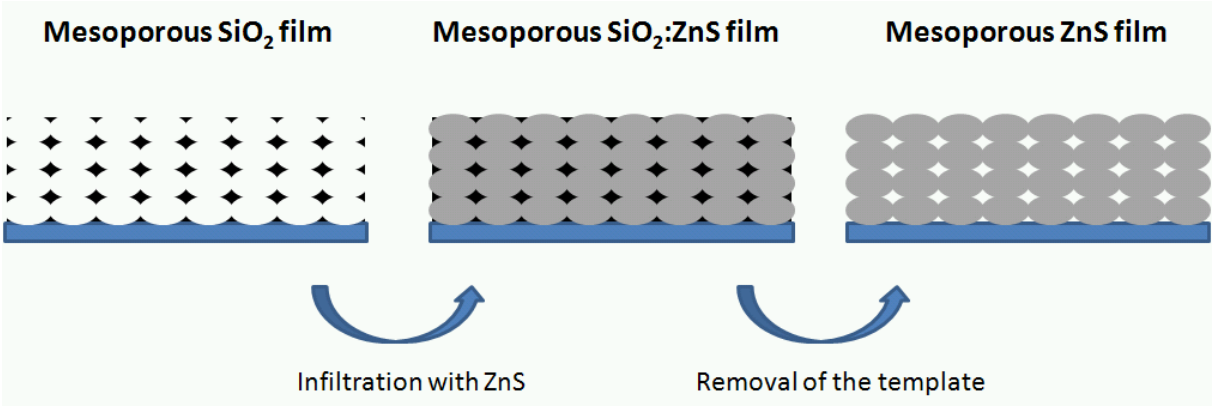

Figure 83: Selected synthesis approach for stable and mesoporous zinc sulfide thin films.

6 References

(1) Wadia, C. Alivisatos, A. P.; Kammen, D. M. *Environmental Science & Technology* **2009**, *43*, 2072-7.

(2) Arvizu, D. Balaya, P. Cabeza, L. Hollands, T. Jäger Waldau, A. Kondo, M. Konseibo, C. Meleshko, V. Stein, W. Tamaura, Y. Xu, H.; Zilles, R. *Direct Solar Energy. In IPCC Special Report on Renewable Energy Sources and Climate Change Mitigation* **2011**.

(3) Repins, I. Contreras, M. A. Egaas, B. DeHart, C. Scharf, J. Perkins, C. L. To, B.; Noufi, R. *Progress in Photovoltaics: Research and Applications* **2008**, *16*, 235-239.

(4) Green, M. A. Emery, K. Hishikawa, Y.; Warta, W. *Progress in Photovoltaics* **2011**, *19*, 84-92.

(5) Zhao, J. Wang, A. Green, M. A.; Ferrazza, F. *Applied Physics Letters* **1998**, *73*, 1991.

(6) Harris, S. *Chemical Physics* **1982**, *67*, 229-237.

(7) Bronger, W. *Angew. Chem. Intern. Ed* **1981**, *20*, 52.

(8) Upadhyaya, H. M.; Chandra, S. *Journal of Materials Science* **1994**, *29*, 2734-2740.

(9) Enculescu, I. Sima, M. Ghiordanescu, V.; Secu, M. *Chalcogenide Letters* **2005**, *2*, 9–15.

(10) Thambidurai, M. Muthukumarasamy, N. Velauthapillai, D. Murugan, N. Agilan, S. Vasantha, S.; Balasundaraprabhu, R. *International Journal of Materials Research* **2011**, *102*, 584-586.

(11) Seoudi, R. Shabaka, A. Eisa, W. H. Anies, B.; Farage, N. M. *Physica B* **2010**, *405*, 919-924.

(12) Zhai, T. Fang, X. Li, L. Bando, Y.; Golberg, D. *Nanoscale* **2010**, *2*, 168-87.

(13) Merdes, S. Mainz, R. Klaer, J. Meeder, A. Rodriguez-Alvarez, H. Schock, H. W. Lux-Steiner, M. C.; Klenk, R. *Solar Energy Materials and Solar Cells* **2010**, *95*, 864-869.

(14) Meyer, N. Meeder, A.; Schmid, D. *Thin Solid Films* **2007**, *515*, 5979-5984.

(15) Lane, D. Rogers, K. D. Painter, J. D. Wood, D. A.; Ozsan, M. E. *Thin Solid Films* **2000**, *361-362*, 1-8.

(16) Watanabe, T. Matsui, M.; Mori, K. *Solar Energy Materials and Solar Cells* **1994**, *35*, 239-245.

(17) Unold, T. Sieber, I.; Ellmer, K. *Applied Physics Letters* **2006**, *88*, 213502.

(18) Momose, N. Htay, M. T. Yudasaka, T. Igarashi, S. Seki, T. Iwano, S. Hashimoto, Y.; Ito, K. *Japanese Journal of Applied Physics* **2011**, *50*, 01BG09.

(19) Kazmerski, L. L. Ayyagari, M. S.; Sanborn, G. A. *Journal of Applied Physics* **1975**, *46*, 4865-4869.

(20) Nakamura, S.; Seto, S. *Physica Status Solidi (C)* **2009**, *6*, 1137-1140.

(21) Baykul, M. C.; Orhan, N. *Thin Solid Films* **2010**, *518*, 1925-1928.

(22) Berry, A. Boone, J.; Vandoren, T. *Materials Letters* **1990**, *10*, 261-263.

(23) Kijatkina, O. Krunks, M. Mahrov, B.; Dloczik, L. *Thin Solid Films* **2003**, *431-432*, 105-109.

(24) Marathe, Y. V.; Shrivastava, V. *Advances in Applied Science Research* **2011**, *2*, 295-301.

(25) Todorov, T. Carda, J. Escribano, P. Grimm, A. Klaer, J.; Klenk, R. *Solar Energy Materials and Solar Cells* **2008**, *92*, 1274-1278.

(26) Herrero, J.; Ortega, J. *Solar Energy Materials* **1990**, *20*, 53-65.

(27) Moriya, K. Watabe, J. Tanaka, K.; Uchiki, H. *Physica Status Solidi (C)* **2006**, *3*, 2848-2852.

(28) Pan, G.-T. Lai, M.-H. Juang, R.-C. Chung, T.-W.; Yang, T. C.-K. *Solar Energy Materials and Solar Cells* **2010**, *94*, 1790-1796.

(29) Fischereder, A. Rath, T. Haas, W. Amenitsch, H. Albering, J. Meischler, D. Larissegger, S. Edler, M. Saf, R. Hofer, F.; Trimmel, G. *Chemistry of Materials* **2010**, 3399-3406.

(30) Ristov, M. Sinadinovski, G. Grozdanov, I.; Mitreski, M. *Thin Solid Films* **1989**, *173*, 53-58.

(31) Carmalt, C. J. Morrison, D. E.; Parkin, I. P. *Journal of Materials Chemistry* **1998**, *8*, 2209-2211.

(32) Yu, C. Yu, J. C. Wen, H.; Zhang, C. *Materials Letters* **2009**, *63*, 1984-1986.

(33) Jiang, Y. Wu, Y. Mo, X. Yu, W. Xie, Y.; Qian, Y. *Inorganic Chemistry* **2000**, *39*, 2964-5.

(34) Trindade, T.; O´Brien, P. *Advanced Materials* **1996**, *8*, 161-163.

(35) Trindade, T. O´Brien, P.; Zhang, X.-mei *Chemistry of Materials* **1997**, *9*, 523-530.

(36) Tao, H. Jin, Z. Wang, W. Yang, J.; Hong, Z. *Materials Letters* **2011**, *65*, 1340-1343.

(37) Courtel, F. M. Paynter, R. W. Marsan, B.; Morin, M. *Chemistry of Materials* **2009**, *21*, 3752-3762.

(38) Zhong, H. Zhou, Y. Ye, M. He, Y. Ye, J. He, C. Yang, C.; Li, Y. *Chemistry of Materials* **2008**, *20*, 6434-6443.

(39) Guo, Q. Hillhouse, H. W.; Agrawal, R. *Journal of the American Chemical Society* **2009**, *131*, 11672-3.

(40) Guo, Q. Ford, G. M. Hillhouse, H. W.; Agrawal, R. *Nano Letters* **2009**, *9*, 3060-5.

(41) Liu, W. Mitzi, D. B. Yuan, M. Kellock, A. J. Chey, S. J.; Gunawan, O. *Chemistry of Materials* **2010**, *22*, 1010-1014.

(42) Look, D.; Manthuruthil, J. *Journal of Physics and Chemistry of Solids* **1976**, *37*, 173-180.

(43) Tell, B.; Thiel, F. A. *Journal of Applied Physics* **1979**, *50*, 5045.

(44) Lewerenz, H. *Solar Energy Materials and Solar Cells* **2004**, *83*, 395-407.

(45) Goossens, A.; Hofhuis, J. *Nanotechnology* **2008**, *19*, 424018.

(46) O´Regan, B.; Schwartz, D. T. *Chemistry of Materials* **1998**, *10*, 1501-1509.

(47) Maier, E. Fischereder, A. Haas, W. Mauthner, G. Albering, J. Rath, T. Hofer, F. List, E. J. W.; Trimmel, G. *Thin Solid Films* **2011**, *519*, 4201-4206.

(48) Weickert, J. Dunbar, R. B. Hesse, H. C. Wiedemann, W.; Schmidt-Mende, L. *Advanced Materials* **2011**, *23*, 1810-1828.

(49) Han, L. Koide, N. Chiba, Y. Islam, A. Komiya, R. Fuke, N. Fukui, A.; Yamanaka, R. *Applied Physics Letters* **2005**, *86*, 213501.

(50) Cai, N. Moon, S.-J. Cevey-Ha, L. Moehl, T. Humphry-Baker, R. Wang, P. Zakeeruddin, S. M.; Grätzel, M. *Nano Letters* **2011**, *11*, 1452-6.

(51) Shaheen, S. E. Brabec, C. J. Sariciftci, N. S. Padinger, F. Fromherz, T.; Hummelen, J. C. *Applied Physics Letters* **2001**, *78*, 841-843.

(52) Sariciftci, N. S. Smilowitz, L. Heeger, A. J.; Wudl, F. *Science* **1992**, *258*, 1474-6.

(53) Ginger, D. S.; Greenham, N. C. *Synthetic Metals* **1999**, *101*, 425-428.

(54) Arici, E. Meissner, D. Schäffler, F.; Sariciftci, N. S. *International Journal of Photoenergy* **2003**, *5*, 199-208.

(55) Cook, S. Ohkita, H. Kim, Y. Benson-Smith, J. J. Bradley, D. D. C.; Durrant, J. R. *Chemical Physics Letters* **2007**, *445*, 276-280.

(56) Cheng, Y.-J. Yang, S.-H.; Hsu, C.-S. *Chemical Reviews* **2009**, *109*, 5868-5923.

(57) Liang, Z. Nardes, A. Wang, D. Berry, J. J.; Gregg, B. A. *Chemistry of Materials* **2009**, *21*, 4914-4919.

(58) Brabec, C. J. Winder, C. Sariciftci, N. S. Hummelen, J. C. Dhanabalan, A. Hal, P. A. van; Janssen, R. A. J. *Advanced Functional Materials* **2002**, *12*, 709-712.

(59) Günes, S. Neugebauer, H.; Sariciftci, N. S. *Chemical Reviews* **2007**, *107*, 1324-38.

(60) Parker, I. D. *Journal of Applied Physics* **1994**, *75*, 1656-1666.

(61) Hoppe, H.; Sariciftci, N. S. *Journal of Materials Research* **2004**, *19*, 1924-1945.

(62) Winder, C. Matt, G. Hummelen, J. C. Janssen, R. A. J. Sariciftci, N. S.; Brabec, C. J. *Thin Solid Films* **2002**, *403-404*, 373-379.

(63) Liu, J. Shi, Y.; Yang, Y. *Advanced Functional Materials* **2001**, *11*, 420-424.

(64) Malliaras, G. G. Salem, J. R. Brock, P. J.; Scott, J. C. *Journal of Applied Physics* **1998**, *84*, 1583-1587.

(65) Zhu, W. Minami, N. Kazaoui, S.; Kim, Y. *Journal of Materials Chemistry* **2004**, *14*, 1924-1926.

(66) Talapin, D. V. Lee, J.-S. Kovalenko, M. V.; Shevchenko, E. V. *Chemical Reviews* **2010**, *110*, 389-458.

(67) Hoppe, H.; Sariciftci, N. S. *Journal of Materials Research* **2004**, *19*, 1924-1945.

(68) Rostalski, J.; Meissner, D. *Solar Energy Materials and Solar Cells* **2000**, *61*, 87-95.

(69) Arici, E. Sariciftci, N. S.; Meissner, D. *Advanced Functional Materials* **2003**, *13*, 165-171.

(70) McDonald, S. A. Konstantatos, G. Zhang, S. Cyr, P. W. Klem, E. J. D. Levina, L.; Sargent, E. H. *Nature Materials* **2005**, *4*, 138-42.

(71) Reiss, P. Couderc, E. Girolamo, J. De; Pron, A. *Nanoscale* **2011**, *3*, 446-89.

(72) Dayal, S. Kopidakis, N. Olson, D. C. Ginley, D. S.; Rumbles, G. *Nano Letters* **2010**, *10*, 239-42.

(73) Oosterhout, S. D. Wienk, M. M. Bavel, S. S. van; Thiedmann, R. Koster, L. J. A. Gilot, J. Loos, J. Schmidt, V.; Janssen, R. A. J. *Nature Materials* **2009**, *8*, 818-24.

(74) Leventis, H. C. King, S. P. Sudlow, A. Hill, M. S. Molloy, K. C.; Haque, S. A. *Nano Letters* **2010**, *10*, 1253-8.

(75) Kazmerski, L. L.; Sanborn, G. A. *Journal of Applied Physics* **1977**, *48*, 3178-3180.

(76) Kazmerski, L. L. White, F. R. Ayyagari, M. S. Juang, Y. J.; Patterson, R. P. *Journal of Vacuum Science and Technology* **1977**, *14*, 65-68.

(77) Yoshino, K. Ikari, T. Shirakata, S. Miyake, H.; Hiramatsu, K. *Applied Physics Letters* **2001**, *78*, 742-744.

(78) Siebentritt, S. *Thin Solid Films* **2002**, *403-404*, 1-8.

(79) Klenk, R. Klaer, J. Köble, C. Mainz, R. Merdes, S. Rodriguez-Alvarez, H. Scheer, R.; Schock, H. W. *Solar Energy Materials and Solar Cells* **2010**, *95*, 1441-1445.

(80) Werner, A. Bruns, J. Klaer, J. Siemer, K.; Bräunig, D. *Thin Solid Films* **2000**, *361-362*, 88-92.

(81) Konovalov, I. *Thin Solid Films* **2004**, *451-452*, 413-419.

(82) Motoyoshi, R. Oku, T. Suzuki, A. Kikuchi, K. Kikuchi, S. Jeyadevan, B.; Cuya, J. *Advances in Materials Science and Engineering* **2010**, 1-11.

(83) Kaiser, I. Ernst, K. Fischer, C.-H. Könenkamp, R. Rost, C. Sieber, I.; Lux-Steiner, M. C. *Solar Energy Materials and Solar Cells* **2001**, *67*, 89-96.

(84) Amenitsch, H. Rappolt, M. Kriechbaum, M. Mio, H. Laggner, P.; Bernstorff, S. *Journal of Synchrotron Radiation* **1998**, *5*, 506-8.

(85) Tiwari, A. Pandya, D, K.; Chopra, K, L. *Thin Solid Films* **1985**, *130*, 217-230.

(86) Krunks, M. Mikli, V. Bijakina, O.; Mellikov, E. *Applied Surface Science* **1999**, *142*, 356-361.

(87) Krunks, M. Mikli, V. Bijakina, O. Rebane, H. Mere, A. Varema, T.; Mellikov, E. *Thin Solid Films* **2000**, *361-362*, 61-64.

(88) Ortega-López, M.; Morales-Acevedo, A. *Thin Solid Films* **1998**, *330*, 96-101.

(89) Krunks, M. Bijakina, O. Varema, T. Mikli, V.; Mellikov, E. *Thin Solid Films* **1999**, *338*, 125-130.

(90) Crews, G. M. Ripperger, W. Kersebohm, D. B. Güthner, T.; Mertschenk, B. *Melamine and Guanamines. Ullmann´s Encyclopedia of Industrial Chemistry.* 2006.

(91) Maier, E. Rath, T. Haas, W. Werzer, O. Saf, R. Hofer, F. Meissner, D. Volobujeva, O. Bereznev, S. Mellikov, E. Amenitsch, H. Resel, R.; Trimmel, G. *Solar Energy Materials and Solar Cells* **2011**, *95*, 1354-1361.

(92) Krunks, M. Leskela, T.; Niinisto, L. *Japanese Journal of Applied Physics* **2000**, *39*, 181-186.

(93) Madarász, J. Krunks, M. Niinisto, L.; Pokol, G. *Journal of Thermal Analysis and Calorimetry* **2004**, *78*, 679-686.

(94) Fan, L. Song, H. Liu, L. Zhao, H. Pan, G. Jiang, J. Dong, B.; Bai, X. *Journal of Nanoscience and Nanotechnology* **2009**, *9*, 2014-2022.

(95) D.I. Svergun and L.A. Feigin *Structure analysis by small-angle x-ray and neutron scattering*; Taylor, G. W., Ed. Plenum Press: New York, 1987.

(96) Beaucage, G. *Journal of Applied Crystallography* **1995**, *28*, 717-728.

(97) Pedersen, J. S. *Advances in Colloid and Interface Science* **1997**, *70*, 171-210.

(98) Kinning, D. J.; Thomas, E. L. *Macromolecules* **1984**, *17*, 1712-1718.

(99) Tolan, M. *X-Ray Scattering from Soft-Matter Thin Films*; Springer Berlin Heidelberg: Berlin, Heidelberg, 1999; Vol. 148.

(100) Wang, S. Gao, Q.; Wang, J. *Journal of Physical Chemistry (B)* **2005**, *109*, 17281-9.

(101) Cliff, G.; Lorimer, G, W. *Journal of Microscopy* **1975**, *103*, 203-207.

(102) Wakkad, M. M. Shokr, E. K. Abd El Ghani, H. A.; Awad, M. A. *The European Physical Journal* **2008**, *43*, 23-30.

(103) Khemiri, N. Akkari, F., C. Kanzari, M.; Rezig, B. *Physica Status Solidi (A)* **2008**, *205*, 1952-1956.

(104) Guezmir, N. Ouerfelli, J.; Belgacem, S. *Materials Chemistry and Physics* **2006**, *96*, 116-123.

(105) Sharma, A. K.; Rajaram, P. *Materials Science and Engineering: B* **2010**, *172*, 37-42.

(106) Katagiri, H. Jimbo, K. Maw, W. S. Oishi, K. Yamazaki, M. Araki, H.; Takeuchi, A. *Thin Solid Films* **2009**, *517*, 2455-2460.

(107) Todorov, T. K. Reuter, K. B.; Mitzi, D. B. *Advanced Materials* **2010**, *22*, E156-E159.

(108) Scragg, J. J. Dale, P. J. Peter, L. M. Zoppi, G.; Forbes, I. *Physica Status Solidi (B)* **2008**, *245*, 1772-1778.

(109) Todorov, T. Kita, M. Carda, J.; Escribano, P. *Thin Solid Films* **2009**, *517*, 2541-2544.

(110) Zhou, Y.-L. Zhou, W.-H. Du, Y.-F. Li, M.; Wu, S.-X. *Materials Letters* **2011**, *65*, 1535-1537.

(111) Mitzi, D. B. Gunawan, O. Todorov, T. K. Wang, K.; Guha, S. *Solar Energy Materials and Solar Cells* **2011**, 1-16.

(112) Kishore, K. Y. B. Suresh, B. G. Uday, B. P.; Sundara, R. V. *Solar Energy Materials and Solar Cells* **2009**, *93*, 1230-1237.

(113) Araki, H. Mikaduki, A. Kubo, Y. Sato, T. Jimbo, K. Maw, W. Katagiri, H. Yamazaki, M. Oishi, K.; Takeuchi, A. *Thin Solid Films* **2008**, *517*, 1457-1460.

(114) Katagiri, H. Sasaguchi, N. Hando, S. Hoshino, S. Ohashi, J.; Yokota, T. *Solar Energy Materials and Solar Cells* **1997**, *49*, 407-414.

(115) Tanaka, T. Kawasaki, D. Nishio, M. Guo, Q.; Ogawa, H. *Physica Status Solidi (C)* **2006**, *3*, 2844-2847.

(116) Weber, A. Krauth, H. Perlt, S. Schubert, B. Kötschau, I. Schorr, S.; Schock, H. W. *Thin Solid Films* **2009**, *517*, 2524-2526.

(117) Oishi, K. Saito, G. Ebina, K. Nagahashi, M. Jimbo, K. Maw, W. Katagiri, H. Yamazaki, M. Araki, H.; Takeuchi, A. *Thin Solid Films* **2008**, *517*, 1449-1452.

(118) Schubert, B. A. Marsen, B. Cinque, S. Unold, T. Klenk, R. Schorr, S.; Schock, H. W. *Progress in Photovoltaics* **2011**, *19*, 93–96.

(119) Yoo, H.; Kim, J. *Thin Solid Films* **2010**, *518*, 6567-6572.

(120) Jimbo, K. Kimura, R. Kamimura, T. Yamada, S. Maw, W. Araki, H. Oishi, K.; Katagiri, H. *Thin Solid Films* **2007**, *515*, 5997-5999.

(121) Tanaka, T. Nagatomo, T. Kawasaki, D. Nishio, M. Guo, Q. Wakahara, A. Yoshida, A.; Ogawa, H. *Journal of Physics and Chemistry of Solids* **2005**, *66*, 1978-1981.

(122) Kurihara, M. Berg, D. Fischer, J. Siebentritt, S.; Dale, P. J. *Physica Status Solidi (C)* **2009**, *6*, 1241-1244.

(123) Pawar, S. M. Pawar, B. S. Moholkar, A. V. Choi, D. S. Yun, J. H. Moon, J. H. Kolekar, S. S.; Kim, J. H. *Electrochimica Acta* **2010**, *55*, 4057-4061.

(124) Araki, H. Kubo, Y. Jimbo, K. Maw, W. S. Katagiri, H. Yamazaki, M. Oishi, K.; Takeuchi, A. *Physica Status Solidi (C)* **2009**, *6*, 1266-1268.

(125) Tanaka, K. Oonuki, M. Moritake, N.; Uchiki, H. *Solar Energy Materials and Solar Cells* **2009**, *93*, 583-587.

(126) Tanaka, K. Fukui, Y. Moritake, N.; Uchiki, H. *Solar Energy Materials and Solar Cells* **2010**, *95*, 838-842.

(127) Yeh, M. Y. Lee, C. C.; Wuu, D. S. *Journal of Sol-Gel Science and Technology* **2009**, *52*, 65-68.

(128) Prabhakar, T.; Jampana, N. *Solar Energy Materials and Solar Cells* **2011**, *95*, 1001-1004.

(129) Rajeshmon, V. G. Kartha, C. S. Vijayakumar, K. P. Sanjeeviraja, C. Abe, T.; Kashiwaba, Y. *Solar Energy* **2011**, *85*, 249-255.

(130) Yoo, H.; Kim, J. *Solar Energy Materials and Solar Cells* **2011**, *95*, 239-244.

(131) Madarász, J. Bombicz, P. Okuya, M.; Kaneko, S. *Solid State Ionics* **2001**, *141-142*, 439-446.

(132) Kumar, Y. B. K. Bhaskar, P. U. Babu, G. S.; Raja, V. S. *Physica Status Solidi (A)* **2010**, *207*, 149-156.

(133) Guo, Q. Ford, G. M. Yang, W.-C. Walker, B. C. Stach, E. A. Hillhouse, H. W.; Agrawal, R. *Journal of the American Chemical Society* **2010**, 7-9.

(134) Cairns, T. Larchar, A.; McKusick, B. *Journal of the American Chemical Society* **1952**, *74*, 5633–5636.

(135) Kumar, K. Babu, S. Bhaskar, U.; Raja, S. *Physica Status Solidi (A)* **2009**, *206*, 1525 - 1530.

(136) Schafer, W.; Nitsche, R. *Materials Research Bulletin* **1974**, *9*, 645-654.

(137) Weber, A. Mainz, R. Unold, T. Schorr, S.; Schock, H.-W. *Physica Status Solidi (C)* **2009**, *6*, 1245-1248.

(138) Schorr, S. Hoebler, H.-J.; Tovar, M. *European Journal of Mineralogy* **2007**, *19*, 65-73.

(139) Steinhagen, C. Panthani, M. G. Akhavan, V. Goodfellow, B. Koo, B.; Korgel, B. A. *Journal of the American Chemical Society* **2009**, *131*, 12554-5.

(140) Paier, J. Asahi, R. Nagoya, A.; Kresse, G. *Physical Review B* **2009**, *79*, 1-8.

(141) Kamoun, N. Bouzouita, H.; Rezig, B. *Thin Solid Films* **2007**, *515*, 5949-5952.

(142) AXS, B. TOPAS: General profile and structure analysis software for powder diffraction data. **2003**.

(143) Seol, J. Lee, S. Lee, J. Nam, H.; Kim, K. *Solar Energy Materials and Solar Cells* **2003**, *75*, 155-162.

(144) Czekelius, C. Hilgendorff, M. Spanhel, L. Bedja, I. Lerch, M. Müller, G. Bloeck, U. Su, D.-S.; Giersig, M. *Advanced Materials* **1999**, *11*, 643-646.

(145) Katagiri, H. Jimbo, K. Tahara, M. Araki, H.; Oishi, K. *MRS Proceedings* **2009**, *1165*.

(146) Moritake, N. Fukui, Y. Oonuki, M. Tanaka, K.; Uchiki, H. *Physica Status Solidi (C)* **2009**, *6*, 1233-1236.

(147) Li, L. Coates, N.; Moses, D. *Journal of the American Chemical Society* **2010**, *132*, 22-3.

(148) Anderson, W. W. *The Journal of Chemical Physics* **1966**, *44*, 3283-3288.

(149) Fernandes, P. A. Salomé, P. M. P.; Cunha, A. F. da *Journal of Alloys and Compounds* **2011**, *509*, 7600-7606.

(150) Huang, J.-H. Lee, C.-P. Ho, Z.-Y. Kekuda, D. Chu, C.-W.; Ho, K.-C. *Solar Energy Materials and Solar Cells* **2010**, *94*, 22-28.

(151) Verma, D. Ranga Rao, a; Dutta, V. *Solar Energy Materials and Solar Cells* **2009**, *93*, 1482-1487.

(152) Nair, P. S. Radhakrishnan, T. Revaprasadu, N. Kolawole, G.; O´Brien, P. *Journal of Materials Chemistry* **2002**, *12*, 2722-2725.

(153) Trindade, T. O'Brien, P. Zhang, X.-mei; Motevalli, M. *Journal of Materials Chemistry* **1997**, *7*, 1011-1016.

(154) Ludolph, B.; Malik, M. A. *Chemical Communications* **1998**, *3*, 1849-1850.

(155) Lazell, M.; O'Brien, P. *Chemical Communications* **1999**, 2041-2042.

(156) Green, M.; O'Brien, P. *Chemical Communications* **1999**, 2235-2241.

(157) Pradhan, N. Katz, B.; Efrima, S. *The Journal of Physical Chemistry (B)* **2003**, *107*, 13843-13854.

(158) Pradhan, N.; Efrima, S. *Journal of the American Chemical Society* **2003**, *125*, 2050-1.

(159) DePuy, C. H.; King, R. W. *Chemical Reviews* **1960**, *60*, 431-457.

(160) Schenk, A. Novel metal-xanthates for preparation of metal sulphides for photovoltaic applications **2011**, pages 90.

(161) González-Roura, A. Casas, J.; Llebaria, A. *Lipids* **2002**, *37*, 401-6.

(162) Raston, C. Tennant, P. White, A.; Winter, G. *Australian Journal of Chemistry* **1978**, *31*, 1493-1500.

(163) Barreca, D. Tondello, E. Lydon, D. Spalding, T. R.; Fabrizio, M. *Chemical Vapor Deposition* **2003**, *9*, 93-98.

(164) Barreca, D. Gasparotto, A. Maragno, C. Seraglia, R. Tondello, E. Venzo, A. Krishnan, V.; Bertagnolli, H. *Applied Organometallic Chemistry* **2005**, *19*, 59-67.

(165) Xu, K.; Ding, W. *Materials Letters* **2008**, *62*, 4437-4439.

(166) Whitmore, W. F.; Lieber, E. *Industrial and Engineering Chemistry* **1935**, 127-129.

(167) Yordanov, N. Gancheva, V. Mladenova, B.; Grampp, G. *Inorganic Chemistry Communications* **2003**, *6*, 54-57.

(168) Gable, R. W. Raston, C. L. Rowbottom, G. L. White, A. H.; Winter, G. *Dalton Transactions* **1981**, 1392-1397.

(169) Casey, A.; Vecchio, M. *Inorganica Chimica Acta* **1987**, *131*, 191-194.

(170) Barone, G. Chaplin, T. Hibbert, T. G. Kana, A. T. Mahon, M. F. Molloy, K. C. Worsley, I. D. Parkin, I. P.; Price, L. S. *Dalton Transactions* **2002**, 1085-1092.

(171) Dai, P. Shen, X. Lin, Z. Feng, Z. Xu, H.; Zhan, J. *Chemical Communications* **2010**, *46*, 5749-51.

(172) Ben Rabeh, M. Chaglabou, N. Kanzari, M.; Rezig, B. *Physics Procedia* **2009**, *2*, 745-750.

(173) Enzenhofer, T. Unold, T. Scheer, R.; Schock, H.-W. *Materials Research Society Symposium Proceedings* **2005**, *865*, 342 -346.

(174) Sun, B.; Greenham, N. C. *Physical Chemistry Chemical Physics* **2006**, *8*, 3557-60.

(175) Liao, H.-C. Chen, S.-Y.; Liu, D.-M. *Macromolecules* **2009**, *42*, 6558-6563.

(176) Yanagisawa, T. Shimizu, T. Kuroda, K.; Kato, C. *Bulletin of the Chemical Society of Japan* **1990**, *63*, 988-992.

(177) Kresge, C. T. Leonowicz, M. E. Roth, W. J. Vartuli, J. C.; Beck, J. S. *Nature* **1992**, *359*, 710-712.

(178) He, Q.; Shi, J. *Journal of Materials Chemistry* **2011**, *31*, 5845-5855.

(179) Hu, J.-S. Ren, L.-L. Guo, Y.-G. Liang, H.-P. Cao, A.-M. Wan, L.-J.; Bai, C.-L. *Angewandte Chemie (International ed. in English)* **2005**, *44*, 1269-73.

(180) Yu, J. C. Zhang, L. Zheng, Z.; Zhao, J. *Chemistry of Materials* **2003**, *15*, 2280-2286.

(181) Ding, Y. Chen, M.; Erlebacher, J. *Journal of the American Chemical Society* **2004**, *126*, 6876-7.

(182) Madhusudan Reddy, K. Satyanarayana, L. Manorama, S. V.; Misra, R. D. K. *Materials Research Bulletin* **2004**, *39*, 1491-1498.

(183) Braun, P. V. Osenar, P. Tohver, V. Kennedy, S. B.; Stupp, S. I. *Journal of the American Chemical Society* **1999**, *121*, 7302-7309.

(184) Li, J. Kessler, H. Soulard, M. Khouchaf, L.; Tuilier, M.-H. *Advanced Materials* **1998**, *10*, 946-949.

(185) Nistor, L. C. Mateescu, C. D. Birjega, R.; Nistor, S. V. *Applied Physics A* **2008**, *92*, 295-301.

(186) Rana, R. K. Zhang, L. Yu, J. C. Mastai, Y.; Gedanken, A. *Langmuir* **2003**, *19*, 5904-5911.

(187) Schüth, F. *Chemistry of Materials* **2001**, *13*, 3184-3195.

(188) Yang, H.; Zhao, D. *Journal of Materials Chemistry* **2005**.

(189) Valdés-Solís, T.; Fuertes, a B. *Materials Research Bulletin* **2006**, *41*, 2187-2197.

(190) Schüth, F. *Angewandte Chemie* **2003**, *115*, 3730-3750.

(191) Grosso, D. Cagnol, F. Soler-Illia, G. J. de A. A. Crepaldi, E. L. Amenitsch, H. Brunet-Bruneau, a; Bourgeois, a; Sanchez, C. *Advanced Functional Materials* **2004**, *14*, 309-322.

(192) Nicolau, Y. F. *Applications of Surface Science* **1985**, *22-23*, 1061-1074.

(193) Niesen, T. *Solid State Ionics* **2002**, *151*, 61-68.

(194) Kosmulski, M. *Chemical Properties of Material Surfaces*; 2001.

(195) Boissiere, C. Grosso, D. Lepoutre, S. Nicole, L. Bruneau, A. B.; Sanchez, C. *Langmuir□: the ACS journal of surfaces and colloids* **2005**, *21*, 12362-71.

(196) Galarneau, A. *Microporous and Mesoporous Materials* **1999**, *27*, 297-308.

(197) Sakatani, Y. Grosso, D. Nicole, L. Boissière, C. A. A. Soler-Illia, G. J. de; Sanchez, C. *Journal of Materials Chemistry* **2006**, *16*, 77.

(198) Brunsen, A. Calvo, A. Williams, F. J. Soler-Illia, G. J. a a; Azzaroni, O. *Langmuir□: the ACS journal of surfaces and colloids* **2011**, *27*, 4328-33.

(199) Nicolau, Y. F. *Journal of The Electrochemical Society* **1990**, *137*, 2915.

(200) Fuertes, M. C. Marchena, M. Marchi, M. C. Wolosiuk, A.; Soler-Illia, G. J. a a *Small* **2009**, *5*, 272-80.

(201) Lee, A. van der *Solid State Sciences* **2000**, *2*, 257-278.

(202) Mitchell, D. R. G. *Ultramicroscopy* **2008**, *108*, 367-74.

7 Appendix

7.1 List of Tables

7.2 List of Figures

7.3 List of Publications

7.3.1 Patents

2011

Solutions for the production of homogeneous large-area photoactive layers consisting of an electroactive polymer and semiconductor nanoparticles and use thereof in photovoltaics and optoelectronics - Trimmel, G.; Trattnig, R.; Schenk, A.; Rath, T.; Mauthner, G.; Haas, W.; Fischereder, A.; Edler, M. *PCT Int. Appl.* **2011**, WO 2011085425 A1 20110721

7.3.2 Papers

2011

Metal sulfide-polymer nanocomposite thin films prepared by a direct formation route for photovoltaic applications - Maier, E. Fischereder, A. Haas, W. Mauthner, G. Albering, J. Rath, T. Hofer, F. List, E. J. W.; Trimmel, G. *Thin Solid Films* **2011**, *519*, 4201-4206

A novel 2,7-linked carbazole based “double cable” polymer with pendant perylene diimide functional groups: preparation, spectroscopy and photovoltaic properties - Mohamad, D. K. Fischereder, A. Yi, H. Cadby, A. J. Lidzey, D. G.; Iraqi, A. *Journal of Materials Chemistry* **2011**, 21, 851-862

Electron Beam-Induced Current (EBIC) in solution-processed solar cells - Reuter, P. Rath, T. Fischereder, A. Trimmel, G.; Hadley, P. *Scanning* **2011**, 33, 1-6

Synthesis and characterization of alternating fluorene-thiophene copolymers bearing ethylene glycol side-chains - Ziegler, E. Pein, A. Fischereder, A.; Trimmel, G. *Monatshefte für Chemie - Chemical Monthly* **2011**, 142, 193-200

2010

Investigation of Cu_2ZnSnS_4 Formation from Metal Salts and Thioacetamide - Fischereder, A.; Rath, T.; Haas, W.; Amenitsch, H.; Albering, J.; Meischler, D.; Larissegger, S.; Edler, M.; Saf, R.; Hofer, F.; Trimmel, G. Chem. Mater. 2010, 22, 11, 3399

7.3.3 Oral Presentations

2011

Preparation of Copper Zinc Tin Sulfide Layers for Photovoltaic Applications via Solution Based Routes - Rath, T.; Fischereder, A.; Schenk, A.; Haas, W.; Amenitsch, H.; Meischler, D.; Edler, M.; Saf, R.; Hofer, F.; Trimmel, G.; EMRS Spring Meeting, Nizza, 2011

Investigations on the formation of metal sulphide-conjugated polymer nanocomposites for photovoltaic applications - Rath, T.; Maier, E.; Fischereder, A.; Haas, W.; Hofer, F.; Trimmel, G.; Hybrid Materials, Strasbourg, 2011

2010

New Nanocomposite Solar Cells prepared by an In-Situ Formation Process - Larissegger, S.; Maier, E.; Rath, T.; Fischereder, A.; Edler, M.; Haas, W.; Moscher, S.; Mauthner, G.; List, E.; Hofer, F.; Meissner, D.; Trimmel, G.; Materials Research Society Spring Meeting, San Francisco, 2010

Investigation of Cu_2ZnSnS_4 formation from metals salts and thioacetamide - Fischereder, A.; Haas, W.; Rath, T.; Amenitsch, H.; Albering, J.; Meischler, D.; Larissegger, S.; Edler, M.; Saf, R.; Hofer, F.; Trimmel, G.; MRS Spring Meeting, San Francisco, 2010

2009

Application of Nanocomposite Layers of Sulfidic Nanoparticles and Electroactive Polymers in Hybrid Photovoltaics - Rath, T.; Maier, E.; Larissegger, S.; Fischereder, A.; Edler, M.; Haas, W.; Fradler, C.; Moscher, S.; Santis Alvarez, A.; Saf, R.; Mauthner, G.; List, E.; Hofer, F.; Trimmel, G.; European Polymer Congress, Graz, 2009

Hybrid Photovoltaic Cells via a Novel Direct Route - Maier, E.; Edler, M.; Fischereder, A.; Fradler, C.; Haas, W.; Hofer, F.; Larissegger, S.; Mauthner, G.; Meischler, D.; Pein, A.; Rath, T.; Saf, R.; Santis Alvarez, A.; Trattnig, R.; Stelzer, F.; List, E.; Trimmel, G.; NAWI Graz Workshop, Graz, 2009

Application of Nanocomposite Layers consisting of Electroactive Polymers and Sulfidic Nanoparticles in Hybrid Photovoltaics - Rath, T.; Maier, E.; Fischereder, A.; Edler, M.; Haas, W.; Fradler, C.; Moscher, S.; Larissegger, S.; Santis Alvarez, A.; Meischler, D.; Saf, R.; Mauthner, G.; List, E.; Hofer, F.; Trimmel, G.; SLONANO, Ljubljana, 2009

7.3.4 Posters

2011

Novel Preparation Methods for Cu2ZnSnS4 Layers for Photovoltaic Applications - Fischereder, A.; Rath, T.; Schenk, A.; Haas, W.; Amenitsch, H.; Meischler, D.; Edler, M.; Saf, R.; Hofer, F.; Trimmel, G.; European Photovoltaic Solar Energy Conference and Exhibition, Hamburg, 2011

$CuInS_2$-Polymer nanocomposite solar cells prepared via metal xanthate precursors - Trimmel, G.; Fischereder, A.; Edler, M.; Moscher, S.; Trattnig, R.; Mauthner, G.; List, E.; Haas, W.; Hofer, F.; Rath, T.; EMRS Spring Meeting, Nizza,2011

Real Time Study of The Formation of ZnS Nanoparticles - Novak, J.; Rath, T.; Pein, A.; Fischereder, A.; Haas, W.; Amenitsch, H.; Hofer, F.; Trimmel, G.; EMRS Spring Meeting, Nizza, 2011

2010

Various Metal Sulfides as Acceptor Phase in Inorganic/Organic Hybrid Photovoltaics prepared by an in-Situ Formation Process - Edler, M.; Fischereder, A.; Maier, E.; Rath, T.; Haas, W.; Mauthner, G.; Albering, J.; Hofer, F.; List, E.; Trimmel, G.; ISOS 3 International Summit on OPV Stability, Roskilde, 2010

Investigation of the formation of $CuInS_2$ layers prepared at moderate temperatures - Meischler, D.; Rath, T.; Fischereder, A.; Bartl, K.; Amenitsch, H.; Trimmel, G.; Stelzer, F.; Saf, R.; MRS Spring Meeting, San Francisco, 2010

Organic-Inorganic Hybrid Solar Cells Based on Metal Sulfides and Electroactive Polymers - Trimmel, G.; Rath, T.; Fischereder, A.; Maier, E.; Albering, J.; Haas, W.; Hofer, F.; Mauthner, G.; List, E.; Meissner, D.; 25th European Solar Energy Conference and Exhibition, Valencia, 2010

Preparation of Copper Zinc Tin Sulfide Layers for Photovoltaic Applications - Rath, T.; Fischereder, A.; Haas, W.; Amenitsch, H.; Maier, E.; Albering, J.; Meischler, D.; Edler, M.; Saf, R.; Hofer, F.; Trimmel, G.; 25th European Solar Energy Conference and Exhibition, Valencia, 2010

2009

Direct Formation of Sulfidic Nanoparticles in Semiconducting Organic Matrices for Hybrid Photovoltaics - Trimmel, G.; Maier, E.; Rath, T.; Larissegger, S.; Fischereder, A.; Edler, M.; Haas, W.; Fradler, C.; Moscher, S.; Santis Alvarez, A.; Saf, R.; Mauthner, G.; List, E.; Hofer, F.; E-MRS, Strassbourg, 2009

Comparison of Metal Sulfides in Organic - Inorganic Nanocomposite Solar Cells by and In-Situ Formation Process - Fischereder, A.; Maier, E.; Dunst, S.; Rath, T.; Haas, W.; Albering, J.; Hofer, F.; Trimmel, G.; E-MRS, Strassbourg, 2009

Preparation and Characterization of Metal Sulfides/ Polymer Nanocomposite Solar Cells - Fischereder, A.; Maier, E.; Rath, T.; Haas, W.; Hofer, F.; List, E.; Trimmel, G.; European Polymer Congress, Graz, 2009

Electron microscopy as a tool for morphology control in nanocomposite solar cells - Haas, W.; Zankel, A.; Rath, T.; Maier, E.; Santis Alvarez, A.; Fischereder, A.; Trimmel, G.; Hofer, F.; Microscopy Conference, Graz, 2009

Organic-inorganic semiconductor blends for photovoltaic applications - Rath, T.; Maier, E.; Edler, M.; Fischereder, A.; Larissegger, S.; Pein, A.; Haas, W.; Mauthner, G.; Hofer, F.; List, E.; Trimmel, G.; Nano and Photonics, Mauterndorf, 2009

Comparison of Binary and Ternary Metal Sulfides as Acceptor Phase in Inorganic/Organic Hybrid Photovoltaics prepared by an In-situ Formation Process - Edler, M.; Fischereder, A.; Maier, E.; Rath, T.; Haas, W.; Hofer, F.; Trimmel, G.; MRS fall meeting, Boston, 2009

Organic-inorganic semiconductor blends for photovoltaic applications - Larissegger, S.; Rath, T.; Maier, E.; Edler, M.; Fischereder, A.; Pein, A.; Haas, W.; Hofer, F.; List, E.; Trimmel, G.; Mauthner, G.; 24th European Photovoltaic Solar Energy Conference, Hamburg, 2009